Fakultät für Mathematik, Informatik und Naturwissenschaften | RWTH AACHEN UNIVERSITY

# Topotactic phase transition in $La_{0.6}Sr_{0.4}CoO_{3-\delta}$ thin films: oxygen content, dynamics and reversibility

Von der Fakultät für Mathematik, Informatik und Naturwissenschaften der RWTH Aachen University zur Erlangung des akademischen Grades einer Doktorin der Naturwissenschaften genehmigte Dissertation

vorgelegt von

*Suqin He, Master of Science*

aus

*GuangDong, China*

Berichter: *Prof. Dr. Thomas Brückel*

*Prof. Dr. Rainer Waser*

Tag der mündlichen Prüfung*: Montag* *Datum: 28.04.2025*

# Abstract

Topotactic phase transitions induced by changes in oxygen vacancy concentration can significantly alter the physical properties of complex oxides, including electronic and magnetic properties. Such tunable properties are critical for developing novel electronic and spintronic devices, where control of magnetic and electronic functionalities is essential.

This thesis investigates an oxygen-vacancy-induced topotactic phase transition from perovskite (PV) to brownmillerite (BM) in epitaxial $La_{0.6}Sr_{0.4}CoO_{3-\delta}$ (LSCO) thin films. Depth-sensitive polarized neutron reflectometry (PNR) enable quantitative analysis of magnetization and oxygen content, revealing a continuous transition from $La_{0.6}Sr_{0.4}CoO_{2.97}$ to $La_{0.6}Sr_{0.4}CoO_{2.5}$. BM formation occurs at an oxygen content of 2.67, while the electronic metal-to-insulator transition (MIT) and magnetic ferromagnet-to-non-ferromagnet (FM-to-non-FM) transition occur above an oxygen content of 2.77, without a BM signature. These findings demonstrate that the MIT, FM-to-non-FM, and PV-to-BM transitions are interrelated but distinct processes.

To further understand the phase transition, the reversibility between PV and BM was studied over 20 cycles. XRD showed that, although the PV and BM structures were maintained, the intensities of both peaks decreased by half, suggesting lattice incoherence or decomposition. Magnetometry indicated no change in magnetic properties, while electronic transport measurements showed partially reversible behaviour. X-ray Photoelectron Spectroscopy (XPS) showed that the Co core-level spectra remained unchanged for both the as-grown and redox-treated PV phases. However, the BM-to-PV transition introduced new features in the A-site core-level spectrum, indicating surface chemical changes during this process.

The activation energy for the phase transition was found to be between 0.72 and 0.9 eV by *in-situ* XRD measurements, which is consistent with that of oxygen surface exchange in LSCO. Using platinum to accelerate the surface exchange process further enhanced the phase transition. These suggest that surface exchange is likely the rate-limiting step.

Finally, the study was extended to a free-standing LSCO + $SrTiO_3$ membrane. It exhibited similar structural and magnetic transitions from the PV to BM phase and from a ferromagnetic to non-ferromagnetic state, indicating that the membrane has similar functionalities as the thin film.

These findings highlight the potential of oxygen defect engineering to enable control of topotactic phase transitions, paving the way for perovskite-based devices with tailored functionalities.

# Zusammenfassung

Topotaktische Phasenübergänge, die durch Änderungen in der Sauerstoffleerstellenkonzentration induziert werden, können die physikalischen Eigenschaften komplexer Oxide, einschließlich elektronischer und magnetischer Eigenschaften, erheblich verändern. Solche abstimmbaren Eigenschaften sind entscheidend für die Entwicklung neuartiger elektronischer und spintronischer Systeme, bei denen die Kontrolle magnetischer und elektronischer Funktionalitäten essenziell ist.

Diese Arbeit untersucht einen durch Sauerstoffleerstellen induzierten topotaktischen Phasenübergang von der Perowskit- (PV) zur Brownmillerit- (BM) Phase in epitaktischen $La_{0.6}Sr_{0.4}CoO_{3-\delta}$- (LSCO) Dünnfilmen. Tiefenaufgelöste polarisierte Neutronenreflektometrie (PNR) ermöglichen eine quantitative Analyse von Magnetisierung und Sauerstoffgehalt, wobei ein kontinuierlicher Übergang von $La_{0.6}Sr_{0.4}CoO_{2.97}$ zu $La_{0.6}Sr_{0.4}CoO_{2.5}$ nachgewiesen wurde. Die BM-Bildung tritt bei einem Sauerstoffgehalt von 2,67 auf, während der elektronische Metall-Isolator-Übergang (MIT) und der ferromagnetisch-nicht-ferromagnetische Übergang (FM-zu-nicht-FM) oberhalb eines Sauerstoffgehalts von 2,77 erfolgen, ohne dass ein BM-Signal vorliegt. Diese Ergebnisse zeigen, dass MIT-, FM-zu-nicht-FM- und PV-zu-BM-Übergänge miteinander verbunden, jedoch unterschiedliche Prozesse sind.

Um den Phasenübergang weiter zu verstehen, wurde die Reversibilität zwischen PV und BM über 20 Zyklen untersucht. Röntgendiffraktion (XRD) zeigte, dass, obwohl die PV- und BM-Strukturen erhalten blieben, die Intensitäten beider Peaks um die Hälfte abnahmen, was auf Gitterinkohärenz oder Zersetzung hinweist. Magnetometrie deutete auf keine Änderung der magnetischen Eigenschaften hin, während elektronische Transportmessungen teilweise reversible Eigenschaften zeigten. Röntgenphotoelektronenspektroskopie (XPS) zeigte, dass die Co-Sprektren für die gewachsene PV und redox-behandelten PV-Phasen unverändert blieben. Jedoch wurden beim BM-zu-PV-Übergang neue Merkmale in den Elektronenspektren der inneren Schalen an den A-Stellen beobachtet, die auf chemische Oberflächenänderungen während dieses Prozesses hinweisen.

Die Aktivierungsenergie für den Phasenübergang wurde durch *in-situ* XRD-Messungen auf 0,72 bis 0,9 eV bestimmt, was mit derjenigen des Sauerstoff-Oberflächenaustauschs in LSCO übereinstimmt. Der Einsatz von Platin zur Beschleunigung des Oberflächenaustauschprozesses verstärkte den Phasenübergang weiter. Dies deutet darauf hin, dass der Oberflächenaustausch wahrscheinlich der ratenlimitierende Schritt ist.

Abschließend wurde die Studie auf eine freistehende LSCO + $SrTiO_3$-Membranen ausgeweitet. Diese zeigte ähnliche strukturelle und magnetische Übergänge von der PV- zur BM-Phase und von einem ferromagnetischen zu einem nicht-ferromagnetischen Zustand, was darauf hinweist, dass die Membran ähnliche Funktionalitäten wie der Dünnfilm besitzt.

Diese Ergebnisse unterstreichen das Potenzial der Defekt-Engineering-Strategie, topotaktische Phasenübergänge zu steuern, und ebnen den Weg für Perowskit-basierte Systeme mit maßgeschneiderten Funktionalitäten.

# Acknowledgements

"This thesis is the result of the support, help, and encouragement of many wonderful people."

First and foremost, I would like to thank Dr. Felix Gunkel and Dr. Oleg Petracic for bringing me into this PhD project. Entering the field of complex oxides has been a challenging and rewarding journey. I owe special thanks to Dr. Felix Gunkel for being a fantastic mentor—your guidance in solid-state ionics, thin film growth, and thin film characterization has been invaluable. Apart from offering valuable insights for the project, you have always supported my personal growth as a researcher by finding me new opportunities and exciting collaborations. Thank you for your care, insight and humour. Your insightful and often challenging questions have consistently motivated me throughout my PhD, pushing me to expand and refine my knowledge in the field of phase transitions. Tackling these questions has deepened my understanding of my PhD topic.

I also want to thank Dr. Oleg Petracic for always asking the right questions and giving me the freedom to explore. Working with you has been a great opportunity to learn about magnetism, neutron scattering, and other scattering techniques. Your guidance always pointed me in the right direction, pushing me to expand my knowledge in these areas. I feel truly fortunate to have had such supportive supervisors who enabled me to grow as a researcher, both in thin film studies and in the broader fields of magnetism and scattering.

Thank you, Dr. Felix Gunkel, Prof. Regina Dittmann, and Prof. Rainer Waser, for hosting me at the PGI-7 institute for my PhD studies. I still vividly remember my first day at PGI-7, where the warm and welcoming atmosphere made me feel immediately at ease. My colleagues were always willing to lend a hand with both work and life challenges, and I am particularly grateful to my office mates in PGI-7, Anton Kaus and Lisa Heymann, in office 100a. They patiently listened to my frustrations over unsuccessful experiments and the struggles of writing, and their understanding and encouragement were invaluable.

As a bridge PhD student, I also had the opportunity to work in JCNS-2 under the supervision of Dr. Oleg Petracic and Prof. Thomas Brückel. This experience introduced me to the fields of neutron science and magnetism, driving my enthusiasm for these topics. During my master's studies, I considered these areas to be among the most challenging in condensed matter physics and never anticipated that I would pursue a specialisation in them. However, my time at JCNS-2 completely changed this perspective, as I came to appreciate the power of magnetism and

neutron scattering in explaining fundamentals. I am grateful to the JCNS-2 team for giving me the chance to expand my knowledge in this field. I would also like to thank my colleagues, including Chenyang Yin and Lei Cao, for engaging in ongoing discussions about magnetism and neutron scattering, which greatly enhanced my understanding.

I am deeply grateful to all the instrument scientists at various beamlines worldwide. My sincere thanks to Dr. Valeria Lauter (SNS, USA) for her assistance in conducting neutron reflectivity experiments at beamline BL-4A. Despite the challenges posed by COVID-19 in 2019, your support made it possible, and our efforts resulted in a high-impact publication. I would also like to extend my appreciation to Dr. Christoph Schlüte (DESY, Hamburg) for his consistent support with XPS experiments, even during late evenings and weekends. Finally, I am very thankful to Dr. Moritz Weber (Advanced Light Source, Berkeley, USA) for transporting my samples to the US, independently conducting experiments, and helping with XPS data analysis. Your help has been essential in advancing this research.

This work has been greatly supported by collaborations with other groups within Forschungszentrum Jülich. My sincere thanks go to Dr. András Kovács (ERC) for his assistance with TEM measurements and for his guidance in TEM data analysis. I am also grateful to Dr. Jürgen Schubert and Dr. Omar Concepción from PGI-9 for their help with RBS measurements, which have been crucial in analyzing the A and B site stoichiometry of my samples. Many thanks to Berthold Schmitz, for your constant assistance with the magnetic and electronic transport measurements.

Finally, I would like to express my sincere gratitude to Prof. Thomas Brückel for being my academic supervisor and for offering me the opportunity to undertake this project. Thank you for carefully reviewing this thesis and for your insightful feedback, which continually challenged me to refine my thinking. I am also deeply appreciative of the engaging courses you taught, which provided a strong foundation in magnetism and neutron scattering. I am equally thankful to Prof. Rainer Waser for serving as my second examiner and for his support throughout this project. His support in travel, experiments, and access to instruments at the PGI-7 institute was indispensable. The welcoming and collaborative environment he fosters within PGI-7 made my time there both enjoyable and enriching, and I am truly grateful for that.

# Contents

# 1. Introduction

Oxygen defects play a crucial role in determining the physical properties of complex oxides and their potential applications. Controlling the oxygen vacancies in complex oxides can tune their electronic, magnetic and ionic properties. Such tunability is important for various applications, from memristive devices [1–7] to field-effect and tunnelling devices, [8–10] and from solid oxide fuel cells [11, 12] and gas separation membranes [13, 14] to water splitting catalysts [15–17] and oxygen sensors [18, 19].

In the limit of a high oxygen vacancy concentration, a layered oxygen-vacancy-ordered Brownmillerite (BM) structure can be realized from the Perovskite (PV) framework, with significant oxygen removal from the lattice [20–24]. This transition typically occurs in oxides, such as cobaltites, manganites, and ferrites, which favour low transition metal valence states [22, 25–38]. The topotactic nature of this phase transition allows the controlled incorporation of oxygen vacancies without introducing additional structural defects, thereby maintaining the integrity of the material's mechanical and morphological properties during the transition [26]. Furthermore, the distribution and dynamics of oxygen vacancies are directly related to magnetic and electronic properties, opening avenues for controlling these properties through ionic exchange [39–43].

While this physics has been extensively studied, several key questions remain unclear. First, the impact of vacancy ordering on the magnetic and electronic properties is still not fully understood. While it is generally considered that the PV phase is metallic and ferromagnetic, while the BM phase is insulating and non-ferromagnetic, often showing antiferromagnetic behaviour [44], it is unclear whether the metal-insulator transition and the ferromagnetic-to-non-ferromagnetic transition occur simultaneously with the structural phase transition. Secondly, much of the previous work has focused on single-cycle phase transitions, but the reversibility of these transitions—particularly in terms of structural, chemical, electronic and magnetic properties—remains underexplored. Furthermore, the exact ionic mechanisms driving these phase transitions are not fully established. While previous studies have speculated on these mechanisms, the rate-limiting steps are not yet fully understood [45]. Finally, applying the phase transition in oxide materials to practical uses, such as flexible electronics and sensors, remains challenging due to substrate-induced constraints affecting the phase behaviour. This raises the question of whether free-standing membranes, free from substrate effects, can undergo phase transitions and exhibit comparable functionality to thin-film samples.

To address these open questions, this thesis presents a systematic study of the oxygen-vacancy-

induced phase transition in $La_{0.6}Sr_{0.4}CoO_{3-\delta}$ (LSCO) epitaxial thin films under reducing conditions. The main goal is to explore the interplay between structural, electronic, and magnetic transitions as a function of oxygen content using techniques, including X-ray diffraction (XRD) and Polarized Neutron Reflectometry (PNR). By performing *in-situ* XRD measurements, the kinetics between the PV and BM phase transition are investigated. The reversibility of the phase transitions is studied over 20 cycles to understand the structural, electronic and magnetic properties of the LSCO under repeated phase changes, and the surface chemistry changes are determined through surface-sensitive techniques such as photoelectron spectroscopy (XPS). Furthermore, the ionic mechanisms driving the phase transition are investigated, and the activation energy is determined, revealing the rate-limiting step of the phase transition. Lastly, the study extends to free-standing LSCO + $SrTiO_3$ membranes, investigating their potential to exhibit phase transitions without substrate-induced constraints, thereby offering insights into their applicability in flexible electronics and sensors.

In summary, this thesis aims to provide deeper insights into the nature of the phase transition between PV and BM in complex oxides and its effects on the material properties. Addressing these key questions can improve our understanding of the role of oxygen vacancies in tuning the properties of oxides, thus advancing the development of functional materials for a wide range of applications.

**Thesis Outline**

Chapter 2 provides an introduction to the theoretical background of complex oxide properties. It covers various types of magnetic interactions and orders, followed by the structural properties of PV and BM oxides. It also covers oxygen diffusion and surface exchange processes. As X-ray and neutron scattering methods are extensively used to investigate LSCO samples, the theoretical foundations of scattering theory are also detailed.

Chapter 3 describes the experimental methods and instruments used for characterizing the LSCO thin films. Chapter 4 presents the results of this thesis, including the control of the topotactic phase transition through thermal annealing, the coupling between the structural, electronic, and magnetic properties, the reversibility and dynamics of the phase transition, and the study of free-standing LSCO+$SrTiO_3$ membranes during the phase transition.

Finally, Chapter 5 summarizes and discusses the main findings, while Chapter 6 provides an outlook for future research and Chapter 7 presents the conclusions of the thesis.

# 2. Theoretical background

In this chapter, the theoretical background on cobalt-based transition metal oxides is discussed. The chapter begins with an introduction to the fundamentals of condensed matter magnetism, exchange interactions, and collective behaviors in these materials. Subsequently, I discuss the perovskite and brownmillerite structures. The following sections cover oxygen diffusion and surface exchange kinetics. The chapter concludes with an overview on scattering theory, including diffractometry, reflectometry, and polarized neutron reflectivity techniques.

## 2.1. Physical properties of transition metal oxides

Transition metal oxides (TMOs) [46–48] exhibit a diverse array of physical properties due to the presence of transition metal ions with partially filled d-orbitals, which facilitate complex electron interactions. These interactions are key to their magnetic behavior and lead to exchange interactions and collective behaviors. Thus, it is necessary to explore the basic concepts of magnetism in this section, including the magnetic moment, types of collective behaviors, and exchange interactions.

### 2.1.1. An atom in a magnetic field

The interaction of an atom in a magnetic field plays a crucial role in understanding the magnetic phenomena discussed in this chapter. The energy associated with an electron's spin in a magnetic field aligned along the $z$-axis can be expressed as:

$$E = g\mu_B B m_s \tag{2.1}$$

where $g \approx 2$ is the electron's g-factor, $\mu_B$ is the Bohr magneton, and $m_s = \pm\frac{1}{2}$ is the magnetic spin quantum number. This interaction results in two energy levels, $E \approx \pm\mu_B B$, reflecting the spin's alignment or anti-alignment with the field.

In addition to spin, electrons exhibit an orbital angular momentum. For an electron located at $\mathbf{r}_i$ with momentum $\mathbf{p}_i$, the total orbital angular momentum $\hbar\mathbf{L}$ of the atom is given by [49]:

$$\hbar\mathbf{L} = \sum_i \mathbf{r}_i \times \mathbf{p}_i \tag{2.2}$$

where the summation is taken over all the electrons in the atom.

The unperturbed atomic Hamiltonian, $\mathcal{H}_0$, incorporates the kinetic and potential energy contributions of the $Z$ electrons in the atom:

$$\hat{\mathcal{H}}_0 = \sum_{i=1}^{Z} \left( \frac{\mathbf{p}_i^2}{2m_e} + V_i \right), \tag{2.3}$$

Here, $m_e$ represents the mass of the electron, $\frac{\mathbf{p}_i^2}{2m_e}$ denotes the kinetic energy, and $V_i$ is the potential energy of the $i$-th electron.

When a magnetic field $\mathbf{B}$ is applied, represented as $\mathbf{B} = \nabla \times \mathbf{A}$ through the vector potential $\mathbf{A}$, the kinetic energy of electrons must be modified. Using the gauge

$$\mathbf{A}(\mathbf{r}) = \frac{\mathbf{B} \times \mathbf{r}}{2} \tag{2.4}$$

The kinetic energy becomes:

$$\frac{\left[\mathbf{p}_i + e\mathbf{A}(\mathbf{r}_i)\right]^2}{2m_e} \tag{2.5}$$

The resulting modified Hamiltonian then becomes:

$$\begin{aligned} \hat{\mathcal{H}} &= \sum_{i=1}^{Z} \left( \frac{\left[\mathbf{p}_i + e\mathbf{A}\left(\mathbf{r}_i\right)\right]^2}{2m_e} + V_i \right) + g\mu_B \mathbf{B} \cdot \mathbf{S} \\ &= \sum_{i=1}^{Z} \left( \frac{\mathbf{p}_i^2}{2m_e} + V_i \right) + \mu_B (\mathbf{L} + g\mathbf{S}) \cdot \mathbf{B} + \frac{e^2}{8m_e} \sum_i \left(\mathbf{B} \times \mathbf{r}_i\right)^2 \\ &= \hat{\mathcal{H}}_0 + \mu_B (\mathbf{L} + g\mathbf{S}) \cdot \mathbf{B} + \frac{e^2}{8m_e} \sum_i \left(\mathbf{B} \times \mathbf{r}_i\right)^2 \end{aligned} \tag{2.6}$$

The main contribution to the modified Hamiltonian is typically the second term $\mu_B(\mathbf{L}+g\mathbf{S})\cdot\mathbf{B}$, which arises from the atom's magnetic moment and leads to paramagnetism. However, this term can sometimes vanish under certain conditions. In such cases, the third term, $\frac{e^2}{8m_e}\sum_i(\mathbf{B}\times\mathbf{r}_i)^2$, becomes relevant, representing the atom's diamagnetic response to the applied magnetic field. These terms will be further explained in the sections on diamagnetism (Section 2.1.2) and paramagnetism (Section 2.1.3). [49]

### 2.1.2. Diamagnetism

All material shows some degree of diamagnetism, characterized by a weak, negative magnetic susceptibility. In diamagnetic substances, an applied magnetic field induces a magnetic moment that opposes the field. Although this effect is often described through classical arguments—such as the generation of a back electromotive force (e.m.f.) by the action of the magnetic field on the orbital motion of electrons, as described by Lenz's law. However, the Bohr-van Leeuwen theorem highlights the limitations of classical explanations for magnetic phenomena. Instead,

diamagnetism must be understood as an entirely quantum mechanical effect and should be treated as such.

To illustrate the quantum mechanical origin of diamagnetism, consider an atom with completely filled electronic shells, where the paramagnetic term in the Hamiltonian (Equation 2.6) can be neglected. If $\mathbf{B}$ is parallel to the $z$-axis, then $\mathbf{B} \times \mathbf{r}_i = B(-y_i, x_i, 0)$, and

$$(\mathbf{B} \times \mathbf{r}_i)^2 = B^2 \left(x_i^2 + y_i^2\right) \tag{2.7}$$

The first-order shift in the ground-state energy is then expressed as:

$$\Delta E_0 = \frac{e^2 B^2}{8 m_\mathrm{e}} \sum_{i=1}^{Z} \langle 0 | \left(x_i^2 + y_i^2\right) | 0 \rangle, \tag{2.8}$$

$|0\rangle$ is the ground state wave function. If we assume that the atom is spherically symmetric, $\langle x_i^2 \rangle = \langle y_i^2 \rangle = \frac{1}{3} \langle r_i^2 \rangle$. then we have

$$\Delta E_0 = \frac{e^2 B^2}{12 m_\mathrm{e}} \sum_{i=1}^{Z} \langle 0 | r_i^2 | 0 \rangle. \tag{2.9}$$

For a solid consisting of $N$ ions, each with $Z$ electrons of mass $m_e$, in a volume $V$ with all shelf filled, the magnetization at zero temperature is derived from the Helmholtz free energy $F$, given by:

$$M = -\frac{\partial F}{\partial B} = -\frac{N}{V} \frac{\partial \Delta E_0}{\partial B} = -\frac{N e^2 B}{6 m_\mathrm{e}} \sum_{i=1}^{Z} \langle r_i^2 \rangle. \tag{2.10}$$

Thus, the diamagnetic susceptibility ($\chi_d$) can be obtained as

$$\chi_d = \frac{M}{H} \approx \frac{\mu_0 M}{B}, \quad \text{assuming} \quad \chi_d \ll 1. \tag{2.11}$$

By following this procedure, one arrives at the expression:

$$\chi_d = -\frac{N}{V} \frac{e^2 \mu_0}{6 m_\mathrm{e}} \sum_{i=1}^{Z} \left\langle r_i^2 \right\rangle. \tag{2.12}$$

This expression, derived from first-order perturbation theory, indicates that the diamagnetic susceptibility is temperature-independent. While elevated temperatures may enhance the influence of excited states, their contribution to $\chi_d$ remains negligible. This property makes diamagnetic substrates ideal for studying the magnetic properties of thin film systems, as they provide a stable background that does not interfere with the magnetic measurements of the thin film. For instance, in this thesis, we utilized diamagnetic substrates such as $SrTiO_3$ to

study the magnetic properties of the thin film system. [49]

### 2.1.3. Paramagnetism

Paramagnetism corresponds to a positive magnetic susceptibility so that an applied magnetic field induces a magnetization that aligns parallel to the field. The previous section discusses materials with no unpaired electrons, where the atoms or molecules did not exhibit a magnetic moment unless influenced by an external field. In contrast, this section focuses on atoms that have a non-zero magnetic moment due to the presence of unpaired electrons. Without an external magnetic field, these magnetic moments point in random directions due to thermal fluctuations, as the interactions between neighboring moments are weak and can generally be considered independent. However, when an external magnetic field is applied, the magnetic moments tend to align with the field.

The magnetic moment of an atom is related to its total angular momentum $\mathbf{J}$, which is the sum of its orbital angular momentum $\mathbf{L}$ and spin angular momentum $\mathbf{S}$. Therefore, the total angular momentum is expressed as:

$$\mathbf{J} = \mathbf{L} + \mathbf{S} \tag{2.13}$$

Each of these angular momenta has a corresponding quantum number, $l$ for orbital angular momentum and $s$ for spin angular momentum. The quantum number $J$, which represents the total angular momentum, is related to $l$ and $s$ through the vector sum of the two:

$$J = l + s, l + s - 1, \ldots, |l - s| \tag{2.14}$$

Thus, the total angular momentum quantum number $J$ depends on both the orbital angular momentum quantum number $l$ and the spin quantum number $s$. In the case of an electron (where $s = \frac{1}{2}$), $J$ can take values from $|l - s|$ to $l + s$, with integer steps.

Here, the general case of paramagnetism is considered, where the total angular momentum quantum number $J$ can take any integer or half-integer value. The total angular momentum is related to the Brillouin function $\mathbf{B}_J(y)$, which is given by:

$$\mathbf{B}_J(y) = \frac{2J+1}{2J} \coth\left(\frac{2J+1}{2J} y\right) - \frac{1}{2J} \coth\left(\frac{y}{2J}\right) \tag{2.15}$$

where $y$ is a parameter related to the ratio of the applied magnetic field $B$ to the temperature $T$, typically defined as $y = \frac{g\mu_B B}{k_B T}$, where $g$ is the g-factor, $\mu_B$ is the Bohr magneton, $B$ is the magnetic field, $k_B$ is the Boltzmann constant, and $T$ is the temperature.

The Brillouin function has various limiting cases. For example, when $J \to \infty$, it reduces to a Langevin function ($L(y) = \coth y - \frac{1}{y}$):

$$\mathbf{B}_\infty(y) = L(y), \tag{2.16}$$

and when $J = \frac{1}{2}$, it reduces to a tanh function:

$$\mathbf{B}_{1/2}(y) = \tanh(y). \tag{2.17}$$

A typical value of $y$ can be estimated as follows: for $J = \frac{1}{2}$, $g_J = 2$, with $B = 1\,\mathrm{T}$, the value of $y$ at room temperature is approximately $2 \times 10^{-3}$. Thus, except at very low temperatures and/or in extremely large magnetic fields, the experimental situation will correspond to $y \ll 1$ (and hence the paramagnetic susceptibility $\chi_p \ll 1$). For small $y$, we can derive the following result by using the Maclaurin expansion [50] of $\coth y$:

$$\mathbf{B}_J(y) = \frac{(J+1)y}{3J} + O\left(y^3\right) \tag{2.18}$$

Here, $O(y^3)$ denotes the remainder term that includes all higher-order terms in the expansion, starting from $y^3$. This term represents the error in the approximation, which becomes negligible as $y$ becomes small.

To connect this with the susceptibility:

The magnetization $M$ is related to the applied magnetic field $H$ via the susceptibility $\chi_p$ as:

$$M = \chi_p H \tag{2.19}$$

For small $\chi_p$, the magnetization also depends on the field strength and the properties of the material. The magnetization can be expressed as:

$$M = n\mu_{\text{eff}}\mathbf{B}_J(y) \tag{2.20}$$

where $n$ is the number of magnetic ions per unit volume, and $\mu_{\text{eff}}$ is the effective magnetic moment.

For low magnetic fields, we can approximate the magnetization as:

$$M \approx \frac{n\mu_0\mu_{\text{eff}}^2}{3k_{\text{B}}T}B \tag{2.21}$$

where $k_B$ is the Boltzmann constant, $T$ is the temperature, and $\mu_0$ is the permeability of free space. This leads to the susceptibility expression:

$$\chi_p = \frac{M}{H} \approx \frac{\mu_0 M}{B} = \frac{n\mu_0\mu_{\text{eff}}^2}{3k_{\text{B}}T} \tag{2.22}$$

Here, the approximation assumes that $\chi_p \ll 1$ and that the material exhibits classical paramagnetic behavior (classical Curie law). This dependence of the susceptibility leads to $\chi_p \propto \frac{1}{T}$, so that a graph of $\frac{1}{\chi_p}$ against $T$ is a straight line, and a graph of $\chi_p T$ is constant against $T$.

## 2.1.4. Types of collective behaviors

Collective behaviors in magnetic systems arise from the interactions between individual magnetic moments, leading to the emergence of macroscopic magnetic properties. In this section, we will discuss two types of collective behaviors relevant to this thesis.

### 2.1.4.1. Ferromagnetism

Ferromagnetism is an often encountered magnetic behavior where materials exhibit a spontaneous magnetization, i.e., they can maintain a net magnetic moment in the absence of an external magnetic field, see Fig. 2.1. This property arises from the quantum mechanical exchange interaction, which aligns the magnetic moments of individual atoms or ions parallel to each other within a domain. The key to understanding ferromagnetism lies in the interplay between the quantum mechanical spin of electrons and the Pauli exclusion principle [51–53].

According to the Pauli exclusion principle, two electrons in the same atom cannot have the same set of quantum numbers; therefore, electrons in the same orbital must have opposite spins, resulting in paired spins with no net magnetic moment.

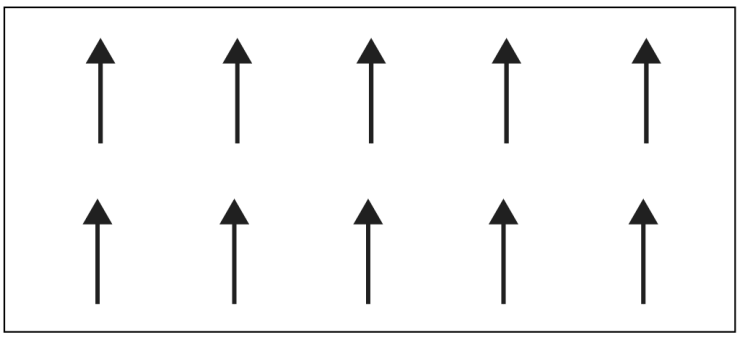

**Figure 2.1.:** Illustration of the magnetic moment alignment in a ferromagnetic material.

In ferromagnetic materials, unpaired electrons in partially filled d or f orbitals lead to the magnetic moment for each atom. The exchange interaction aligns these unpaired spins parallel to each other. This interaction can be understood by considering the overlap of electron wavefunctions. When the wavefunctions of neighboring atoms overlap, the spatial part of the wavefunction must be antisymmetric if the spins are parallel due to the Pauli exclusion prin-

ciple. This antisymmetry reduces the electron-electron repulsion and lowers the system's total energy, making the parallel alignment of spins energetically favorable. [49]

**The value of the Curie temperature** ($T_C$) depends on the magnitude of the exchange interactions and the electronic structure of the constituent atoms. The $T_C$ represents the critical temperature at which the system undergoes a second-order phase transition from a ferromagnetic to a paramagnetic state. Below $T_C$, the free energy of the system is minimized when the magnetic moments are spontaneously aligned, resulting in long-range magnetic order and a net magnetization, as shown in Fig. 2.2 (a). As the temperature approaches $T_C$, thermal fluctuations increase, weakening the exchange interactions that maintain the alignment of spins. At temperatures above $T_C$, the thermal energy overcomes these exchange interactions, causing the magnetic moments to become randomly oriented [54]. This results in a paramagnetic state where the material is magnetized only in the presence of an external magnetic field.

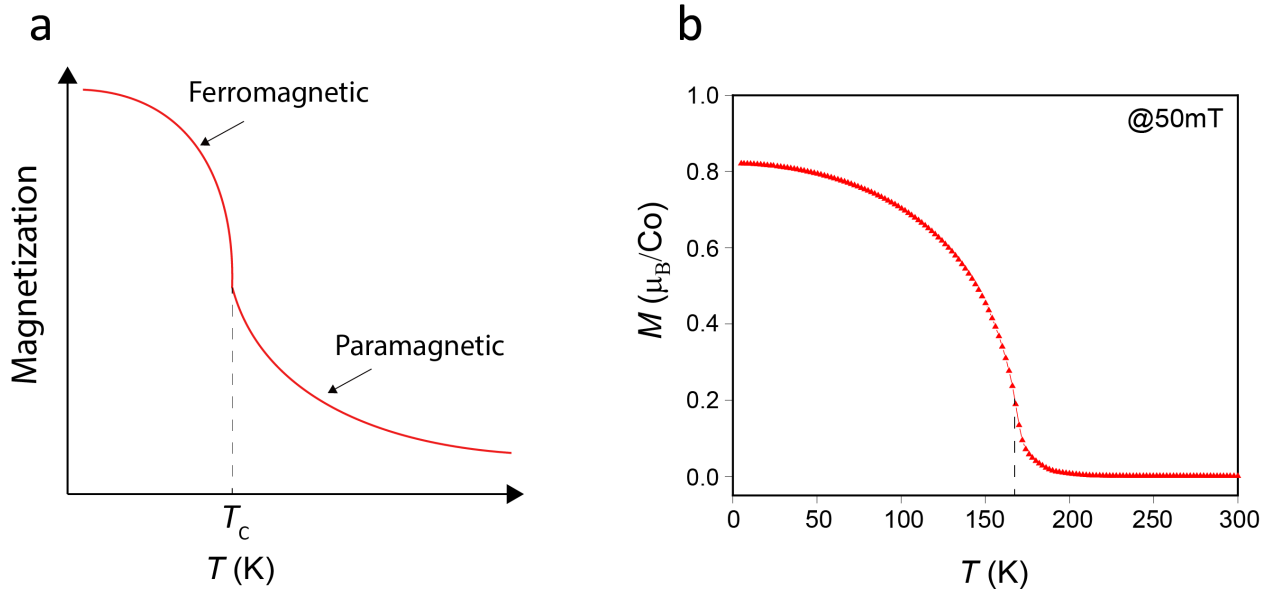


**Figure 2.2.:** Temperature dependence of the field-cooled (FC) magnetic moment. (a) Simulated FC curve showing a clear paramagnetic-to-ferromagnetic transition. The Curie temperature ($T_C$) is identified as the temperature where the magnetic moment starts to increase sharply upon cooling. (b) Experimental FC curve of a 15 nm $La_{0.6}Sr_{0.4}CoO_{3-\delta}$ thin film on a $SrTiO_3$ substrate. $T_C$ is estimated using the dashed line as a guide to the eye. Note that the paramagnetic contribution in the measured curve appears comparatively exaggerated relative to the ferromagnetic component, which may affect the clarity of the transition.

In magnetometry measurements, a small external magnetic field, typically around 50 mT in this thesis, is applied to record the temperature dependence of the magnetic moment, resulting in the field-cooled (FC) curve. The measured FC curve (Fig. 2.2 (b)) is typically less ideal than the theoretical FC curve (Fig. 2.2 (a)), which shows a clear transition from the paramagnetic (PM) to the ferromagnetic (FM) state, as indicated by the dashed line in Fig. 2.2 (a). This discrepancy arises from various factors such as material imperfections (e.g., defects, impurities, grain boundaries), multi-phase compositions, and instrumental limitations, all of which

contribute to a more gradual and less distinct transition. Moreover, the applied magnetic field itself plays a key role in rounding the transition: in the presence of an external field, the second-order PM–FM phase transition becomes smeared due to the field-induced magnetization. As a result, the magnetic moment does not vanish completely above $T_C$, making the transition appear broader. The Curie temperature ($T_C$) is therefore often determined visually as the point of inflection in the FC curve. For more accurate values, fitting to a mean-field model can be employed.

**The hysteresis curve** serves as a typical tool to characterize the magnetic behavior of materials in response to external magnetic fields. When subjected to a cyclic quasi-static magnetic field, ferromagnetic materials exhibit a characteristic looped curve in the plot of magnetization ($M$) versus the applied magnetic field ($H$), as depicted in Fig. 2.3 (a). This hysteresis loop reveals key parameters such as saturation magnetization ($M_s$) and coercivity ($H_c$).

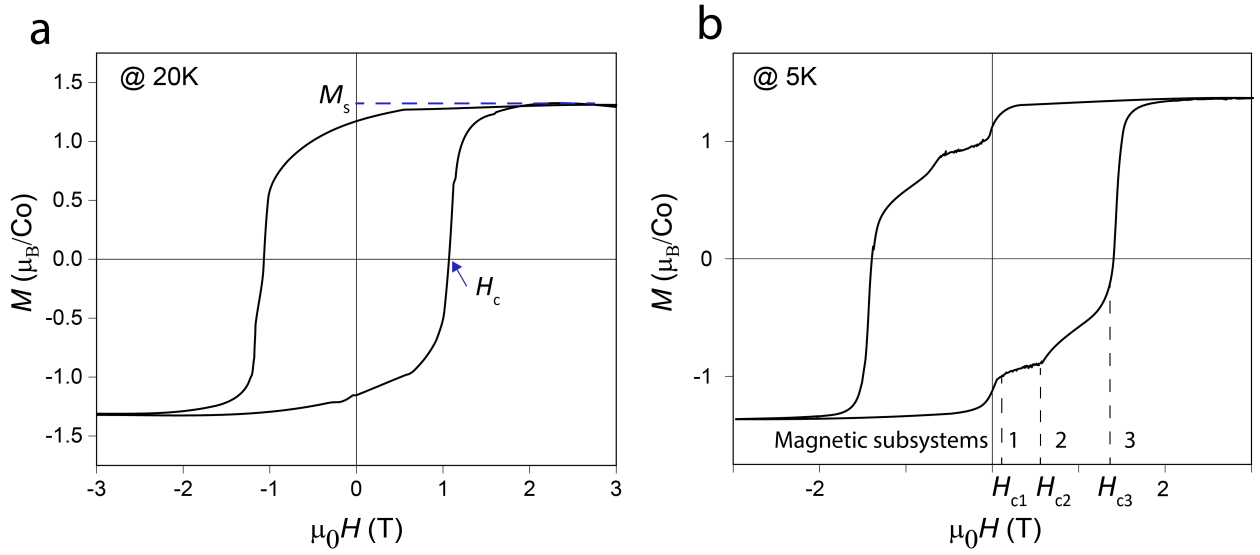


**Figure 2.3.:** Illustration of hysteresis loop. a) Single ferromagnetic system hysteresis, which does not exhibit a "step-like" shape. b) Hysteresis with three magnetic subsystems, where the subsystems can be determined by their corresponding coercivities ($H_{c1}$, $H_{c2}$, and $H_{c3}$).

$M_s$ represents the maximum magnetization attained by a material when all magnetic moments align with the applied magnetic field. In this thesis, we have normalized the saturation magnetization to $\mu_B$/Co. This normalization involves several steps: first, measuring the net magnetic moment of the thin film. Next, determining the total volume of the thin film by multiplying its thickness by the area, with the volume per unit cell obtained from X-ray measurements. Dividing the total volume of the thin film by the volume per unit cell yields the number of unit cells in the sample. Subsequently, dividing the net magnetic moment by the number of unit cells provides the magnetic moment per unit cell, assuming perfect crystalline order. As the magnetic moment of the $La_{0.6}Sr_{0.4}CoO_{3-\delta}$ sample arises solely from the Co ions, we express the normalized magnetization in units of $\mu_B$/Co.

$H_c$ denotes the field required to reduce the magnetization to zero after the sample has been

saturated, as shown in Fig. 2.3 (a). Each magnetic subsystem within the material has its own unique $H_c$. When the sample contains multiple magnetic subsystems, this introduces complexity into the hysteresis loop, resulting often in a "step-like" structure, as shown in Fig. 2.3 (b). These steps occur because each magnetic subsystem responds differently to the applied magnetic field. Then each step in the hysteresis curve corresponds to the coercivity of a different magnetic subsystem. By analyzing these steps and their respective $H_c$ values, we can infer the number and nature of the magnetic subsystems within the sample.

#### 2.1.4.2. Antiferromagnetism

Antiferromagnetic materials exhibit an alternating alignment of magnetic moments (as in Fig. 2.4), resulting in a zero net macroscopic magnetization when no external magnetic field is applied [55].

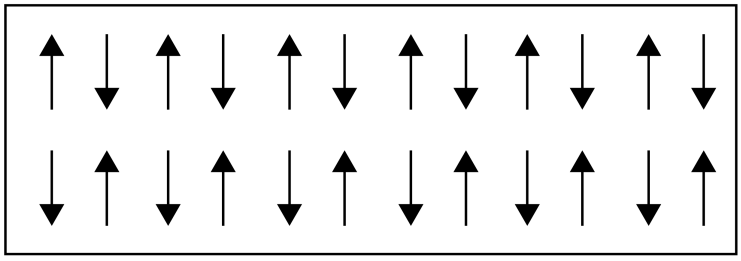

**Figure 2.4.:** Representation of the magnetic moments in an antiferromagnetic system. Adjacent magnetic moments point in opposite directions, leading to zero net magnetization in absence of a magnetic field.

This behavior occurs below the Néel temperature ($T_\mathrm{N}$) which is the phase transition temperature for long-range ordering. The magnetic susceptibility ($\chi_m$) is then:

$$\chi_m = \frac{C}{T + T_\mathrm{N}} \tag{2.23}$$

where $C$ is the material-specific Curie constant and $T$ is the temperature.

To determine the $T_N$ of an antiferromagnetic system, one can analyze the magnetic susceptibility as a function of temperature and the orientation of the applied magnetic field. Below $T_N$, when a magnetic field is applied parallel to the direction of the sublattice magnetization, the parallel susceptibility ($\chi_\parallel$) is minimal ($\chi_\parallel \approx 0$). This is due to the opposing alignment of the moments in the two sublattices, which cancels the net magnetization. However, $\chi_\parallel$ increases sharply as $T_N$ is approached, which is due to the weakening of the antiferromagnetic order caused by thermal fluctuations. In contrast, a field applied perpendicular to the sublattice magnetization causes the moments to tilt slightly, yielding a perpendicular susceptibility ($\chi_\perp$) that is nearly independent of temperature below $T_N$. The sharp increase in $\chi_\parallel$ near $T_N$, alongside the steady behavior of $\chi_\perp$, identifies the Néel temperature as the point where the material transitions from

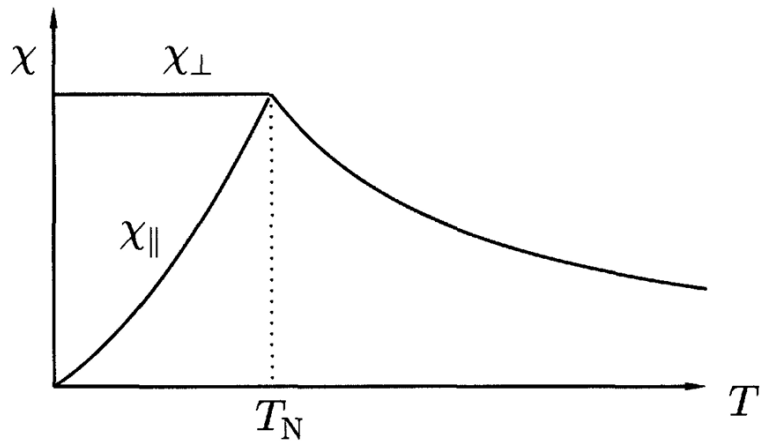


**Figure 2.5.:** Temperature dependence of the parallel ($\chi_\parallel$) and perpendicular ($\chi_\perp$) magnetic susceptibilities, illustrating the behavior of an antiferromagnetic material as it approaches the Néel temperature ($T_N$). This figure is taken from Ref [49].

an antiferromagnetic to a paramagnetic state. These trends are often depicted in susceptibility-temperature plots, as shown in Fig. 2.5. [49]

### 2.1.5. Exchange interactions

The exchange interaction is a quantum mechanical effect that plays usually the dominant role in determining the magnetic properties of solid state systems. It arises from the Pauli exclusion principle and the Coulomb interaction between electrons. In transition metal oxides, the exchange interaction is responsible for the alignment of magnetic moments, leading to various magnetic orders such as ferromagnetism and antiferromagnetism.

The exchange interaction can be described through the Heisenberg model, which considers the interaction between two neighboring spins ($\mathbf{S}_i$ and $\mathbf{S}_j$) as [56] :

$$H_{ex} = -2J\mathbf{S}_i \cdot \mathbf{S}_j \tag{2.24}$$

where $H_{ex}$ is the exchange interaction Hamiltonian and $J$ is the exchange integral. The exchange integral $J$ determines the strength and nature of the interaction: a positive $J$ indicates a ferromagnetic interaction (spins align in the same direction), while a negative $J$ indicates an antiferromagnetic interaction (spins align in opposite directions).

In TMOs, the electron-electron interactions, especially among the d-electrons of the transition metal ions dominate the resulting magnetic properties. These interactions give rise to complex magnetic behaviors, including ferromagnetic and antiferromagnetic ordering. The nature of these magnetic orders is primarily determined by exchange interactions, with double exchange and superexchange being the most significant mechanisms. Thus, the following sections will discuss these two types of exchange interactions in detail.

#### 2.1.5.1. Double exchange interactions in cobalt oxides

Double exchange interactions are an important mechanism in magnetic materials with mixed valence states, first proposed by Clarence Zener [57]. This interaction involves cations with different d-shell occupations, typically differing by one electron, such as $Co^{3+}$ and $Co^{4+}$. In this
.

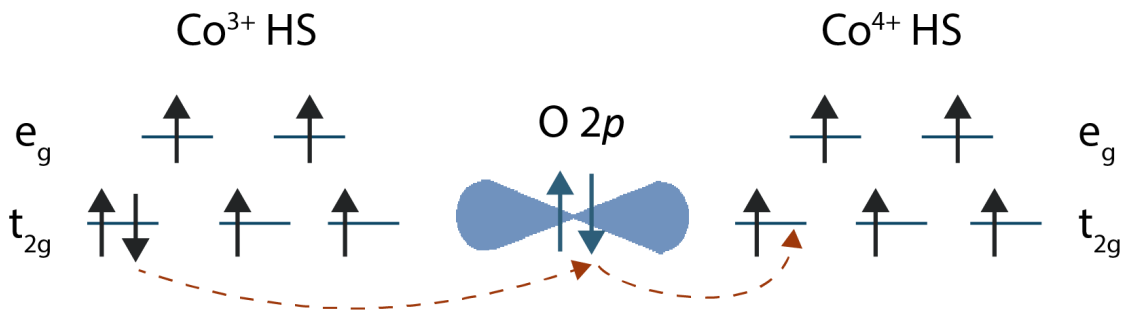


**Figure 2.6.:** The double-exchange mechanism involves the hopping of $t_{2g}$ electrons between $Co^{3+}$ high spin (HS) and $Co^{4+}$ (HS) ions through an intermediate oxygen ion.

scenario, electrons can hop between neighboring cations, leading to a delocalization of electrons and promoting ferromagnetic alignment

In cobalt oxides, one of the channels of the double-exchange mechanism involves the hopping of $t_{2g}$ electrons between $Co^{3+}$ high spin (HS) and $Co^{4+}$ high spin ions through an intermediate oxygen ion (see Fig. 2.6). This process occurs when the spins of the involved electrons are aligned parallel, according to Hund's rules. The alignment minimizes the overall energy of the system, promoting ferromagnetic order. The oxygen ion is critical because it mediates the overlap between the $Co^{3+}$ and $Co^{4+}$ orbitals, enabling spin-polarized electron hopping. If the oxygen ion is missing, this process is no longer possible because the direct overlap of the cobalt orbitals is insufficient to sustain the hopping, disrupting the double-exchange mechanism. The movement of the $t_{2g}$ electrons also provides metallic conductivity, distinguishing it from insulating behavior typically associated with localized electrons.

In $La_{0.6}Sr_{0.4}CoO_{3-\delta}$, the Sr substitution introduces holes, creating a nominal mixture of $Co^{3+}$ ($d^6$) and $Co^{4+}$ ($d^5$) ions. The $Co^{3+}$ ions have an extra electron in the $t_{2g}$ orbital compared to $Co^{4+}$ ions. The hopping of this $t_{2g}$ electron between neighboring $Co^{3+}$ and $Co^{4+}$ ions via oxygen anions, as shown in Fig. 2.6, explains the double-exchange interaction. This electron delocalization not only mediates magnetic exchange coupling but also contributes to the material's conductivity, leading to both metallic and ferromagnetic properties.

#### 2.1.5.2. Superexchange interactions in cobalt oxides

Superexchange interactions are an interaction mechanism in magnetic materials where the magnetic coupling between two ions with the same oxidation state occurs via an intermediary

ion, such as oxygen [58], rather than through direct contact. This interaction is especially significant in cobalt oxides, where the cobalt ions are surrounded by oxygen octahedra. In superexchange scheme, the d-electron occupancy of the involved cations is either the same or differs by two, resulting in localized electrons.

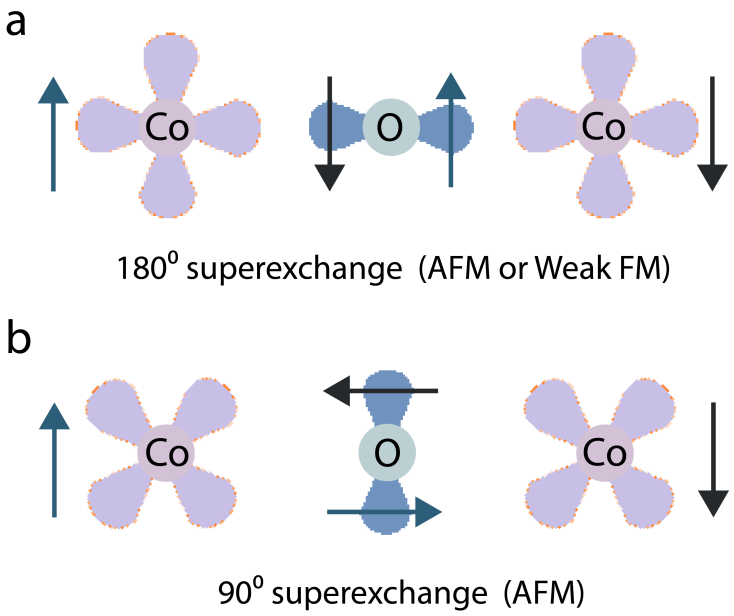


**Figure 2.7.:** Illustration of the superexchange mechanism in cobalt oxides: (a) 180° Co-O-Co bond leading to antiferromagnetic interactions, (b) 90° Co-O-Co bond also resulting in an antiferromagnetic alignment.

In cobalt oxides, the superexchange mechanism typically involves interactions between $Co^{3+}$-$Co^{3+}$ or $Co^{4+}$-$Co^{4+}$ ions mediated through oxygen ions. In a Co-O-Co linkage, the *d*-electrons of one cobalt ion interact indirectly with the *d*-electrons of a neighboring cobalt ion via the *p*-electrons of the oxygen ion. This mediated interaction often results in antiferromagnetic alignment of spins, as electrons tend to align antiparallel to minimize repulsion. The strength and nature of this magnetic coupling are governed by the Goodenough-Kanamori-Anderson (GKA) rules [59–61], which emphasize that bond angles and orbital overlaps between metal ions and oxygen anions significantly influence magnetic properties.

In an ideal 180° Co-O-Co bond (Fig. 2.7 (a)), the interaction is strong and predominantly antiferromagnetic. However, deviations from this angle can weaken the interaction or, under specific conditions, lead to weak ferromagnetic coupling, which is outside the scope of this thesis. Similarly, a 90° Co-O-Co arrangement also results in antiferromagnetic alignment (Fig. 2.7 (b)).

In $La_{0.6}Sr_{0.4}CoO_{3-\delta}$, the mixed valence state and the resulting $Co^{3+}/Co^{4+}$ ratio introduce a complexity in the magnetic interactions. While double exchange facilitates ferromagnetic order through delocalized electrons, superexchange contributes to antiferromagnetic interactions due to localized electrons. The competition and coexistence of these interactions lead to interesting collective magnetic properties.

## 2.2. $La_{0.6}Sr_{0.4}CoO_{3-\delta}$ thin films: Perovskite to Brownmillerite transition

The topotactic phase transformation from perovskite to brownmillerite has gained significant attention in recent years. Materials like $SrCoO_{3-\delta}$, $SrFeO_{3-\delta}$, $La_{1-x}Sr_xCoO_{3-\delta}$ and $La_{1-x}Sr_xMnO_{3-\delta}$ have been extensively studied, with the A-site doping and B-site transition metals playing a key role in determining the oxygen vacancy ordering and stability of the BM phase. In $SrCoO_{3-\delta}$, the transition is readily achieved as cobalt prefers lower oxidation states (3+ in the brownmillerite phase) over higher states (4+ in the perovskite phase) [62]. In contrast, iron in $SrFeO_{3-\delta}$ resists this transition, preferring to maintain a 3+ state, which limits vacancy formation [63]. Manganese and cobalt in $La_{1-x}Sr_xMnO_{3-\delta}$ and $La_{1-x}Sr_xCoO_{3-\delta}$ exhibit greater tunability, with oxygen vacancy behavior governed by Sr doping and the oxidation conditions. These changes directly influence the oxidation states of manganese and cobalt, thereby affecting the material's capacity to accommodate oxygen vacancies and facilitating structural and electronic transitions [64–66].

For $La_{0.6}Sr_{0.4}CoO_{3-\delta}$ thin films, the brownmillerite phase can be induced through thermal annealing in a low oxygen partial pressure environment. This transition leads to notable alterations in the film's structural, electronic, and magnetic properties. To fully understand this transformation, it is important to explore both the perovskite and brownmillerite structures in detail. Section 2.2.1 provides an overview of $La_{0.6}Sr_{0.4}CoO_{3-\delta}$ thin films, leading into Section 2.2.2, which describes the perovskite structure with its pseudo-cubic arrangement and ionic coordination. Section 2.2.3 then focuses on the brownmillerite structure, characterized by ordered layers and oxygen vacancies. Understanding these structural differences will clarify the mechanisms driving the topotactic phase transition in $La_{0.6}Sr_{0.4}CoO_{3-\delta}$ thin films.

### 2.2.1. $La_{0.6}Sr_{0.4}CoO_{3-\delta}$ thin films

$La_{0.6}Sr_{0.4}CoO_{3-\delta}$ (LSCO) is a perovskite oxide known for its intriguing electronic and magnetic properties. Derived from $LaCoO_{3-\delta}$ (LCO), it is formed by substituting lanthanum with strontium, resulting in the perovskite structure $La_{1-x}Sr_xCoO_{3-\delta}$ with specifically $x = 0.4$ in this thesis project. Introducing $Sr^{2+}$ into the LCO lattice alters its properties, both structurally and electronically. $Sr^{2+}$, being larger than $La^{3+}$, increases the average A-site radius and lattice parameter, reducing the rhombohedral distortion of LCO [67]. This structural evolution towards a more cubic symmetry, combined with the mixed oxidation states of Co (which will be discussed in the following paragraph), significantly influences the electronic and magnetic properties of $La_{1-x}Sr_xCoO_{3-\delta}$.

In the $La_{1-x}Sr_xCoO_{3-\delta}$ system, the electronic behavior evolves significantly with varying levels of Sr doping. At $x = 0$, corresponding to undoped $LaCoO_{3-\delta}$, the material is an insulator with $Co^{3+}$ ions predominantly in a low-spin state, resulting in minimal electron hopping and insulating behavior. As Sr doping increases within the range $0 < x < 0.18$, some $Co^{3+}$ ions are

oxidized to $Co^{4+}$, which enhances electron hopping between $Co^{3+}$ and $Co^{4+}$ sites. Although the material remains insulating at low doping levels, an insulator-to-metal transition occurs as $x$ approaches 0.18, marking the onset of metallic behavior. In the moderate to high doping range ($0.18 < x < 0.5$), the material exhibits robust metallic properties, with electronic conduction dominated by double exchange between $Co^{3+}$ and $Co^{4+}$ ions. As doping levels further increase beyond $x = 0.5$, the system becomes increasingly metallic. At the extreme doping level of $x = 1$, corresponding to $SrCoO_{3-\delta}$, the material is fully metallic, with $Co^{4+}$ ions dominating the electronic conduction. [68]

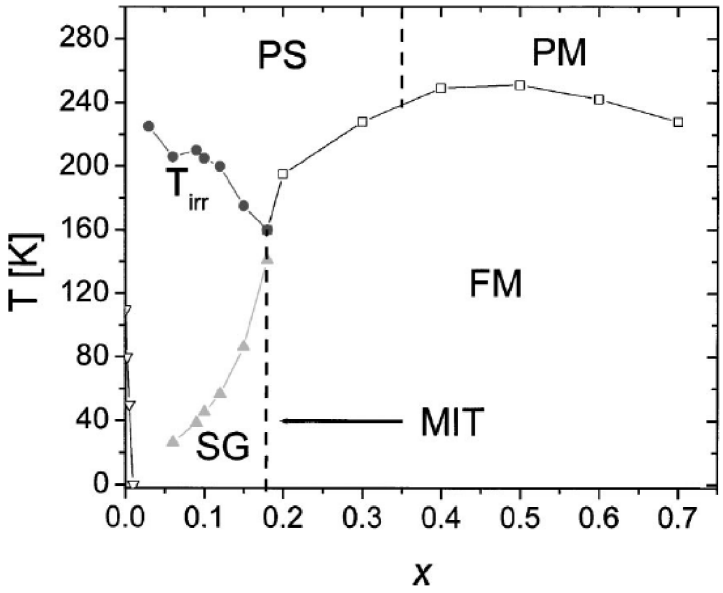


**Figure 2.8.:** Magnetic phase diagram of $La_{1-x}Sr_xCoO_{3-\delta}$ illustrating various magnetic phases for various $x$. PS = paramagnetic semiconductor, PM = paramagnetic metal, FM = ferromagnetic metal, SG = spin glass, MIT = metal-insulator transition, and $T_{irr}$ is the irreversibility temperature which marks the bifurcation of ZFC (zero-field-cooled) and FC dc magnetization curves. This figure is adapted from [68].

Fig. 2.8 [68] depicts the magnetic phase diagram of bulk $La_{1-x}Sr_xCoO_{3-\delta}$. At $x = 0$, corresponding to $LaCoO_{3-\delta}$, the material is a non-magnetic insulator with $Co^{3+}$ ions primarily in a low-spin state, resulting in negligible magnetic interactions. As doping begins ($x < 0.18$), the introduction of $Co^{4+}$ ions induces competing antiferromagnetic ($Co^{3+}/Co^{3+}$) and ferromagnetic ($Co^{3+}/Co^{4+}$) interactions, leading to a spin-glass state where magnetic moments are frozen in a disordered configuration. As Sr doping increases to $0.18 < x < 0.5$, the material transitions into a ferromagnetic phase, driven by enhanced double exchange interactions between $Co^{3+}$ and $Co^{4+}$ ions, which align the magnetic moments over longer distances. However, disordered, glassy regions persist within the ferromagnetic matrix, indicating that, despite the material's overall ferromagnetism, certain areas still exhibit misaligned or disordered magnetic moments. At higher doping levels ($x > 0.5$), the material separates into distinct regions, with small ferromagnetic areas scattered within a mostly non-magnetic or weakly magnetic background. Finally, at $x = 1$, corresponding to $SrCoO_{3-\delta}$, the material exhibits metallic ferromagnetism when $\delta$ is close to 0, largely driven by the presence of $Co^{4+}$ ions. They contribute to the metallic state, but the

ferromagnetic interactions are weakened due to the high degree of electronic delocalization and potential spin-state fluctuations [69]. However, $SrCoO_{3-\delta}$ tends to stabilize in the $SrCoO_{2.5}$ phase, where $\delta$ approaches 0.5. This is because Cobalt ions prefer a lower oxidation state, which can lower the total energy of the system. In this configuration, $Co^{3+}$ ions, particularly in a low-spin state, dominate the system, leading to insulating and antiferromagnetic behavior.

Thus, the as-grown $La_{0.6}Sr_{0.4}CoO_{3-\delta}$ adopts a perovskite cubic structure. This structure exhibits metallic and ferromagnetic properties due to the increased $Co^{4+}$ ratio from the $Sr^{2+}$ doping. The stability of this structure and its relatively straightforward electronic and magnetic states make LSCO an ideal candidate for studying oxygen-vacancy-induced topotactic phase transitions in perovskite oxides. The flexibility of perovskite oxides in accommodating varying oxygen content, along with LSCO's stability (in a defined temperature range), makes thermal annealing in reducing conditions an effective method. This process induces the topotactic transition from the perovskite to the brownmillerite phase, allowing for a comprehensive study of the resulting electronic and magnetic property changes associated with the phase transition.

In the subsequent sections, we discuss deeper the structural characteristics of the pervoskite and brownmillerite phases. Understanding the intrinsic properties of these structures provides a solid foundation for exploring the intricate mechanisms driving the topotactic phase transition. By examining the arrangement of atoms and the role of oxygen vacancies in these phases, we can better understand how these factors influence the overall behavior of the material.

### 2.2.2. Perovskite structure

The perovskite (PV) structure is a widely studied family of crystal structures highly relevant in many areas due to its versatility and occurrence in various functional materials. Named after the mineral perovskite ($CaTiO_3$), this structure is characterized by its specific octahedral lattice arrangement, described by the general formula $ABX_3$.

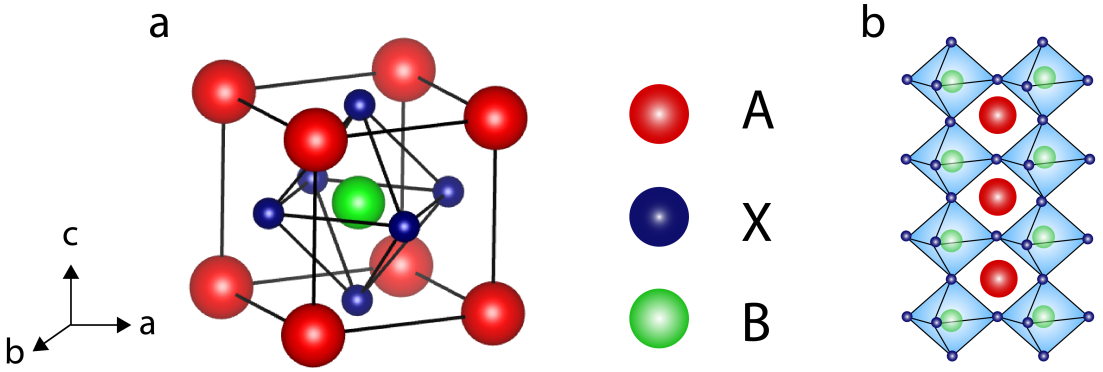


**Figure 2.9.:** Schematic of the perovskite structure. a) The 'A' cations are at the corners of the cube, 'B' cations at the body center, and 'X' anions at the face centers, forming an octahedral coordination around the 'B' cation. The figure is drawn using the VESTA software [70, 71]. b) The repeating octahedral units characterize in particular the structure of perovskite-type materials.

In the ideal PV structure (Fig. 2.9 (a)), the 'A' cation is larger and occupies the corners of the cubic unit cell, while the smaller 'B' cation is located at the body center of the cube. The 'X' anions occupy the face centers, forming an octahedral coordination around the 'B' cation. This configuration can be visualized as a network of corner-sharing $BX_6$ octahedra, with the 'A' cations filling the spaces between them (Fig. 2.9 (b)). The arrangement of these ions in a cubic lattice results in the repetition of the octahedral units throughout the PV single crystal or thin film, providing the structural basis for its diverse properties.

However, deviations from this ideal structure, such as octahedral tilting and distortions, are common in many real perovskites. These distortions, which often occur due to strain or lattice mismatches, play a critical role in altering the material's magnetic properties, particularly near structural defects such as cracks. Octahedral tilting can influence the overlap of the transition metal ion's d-orbitals, thereby modifying the magnetic exchange interactions.

The electronic and magnetic properties of transition metal PV systems are governed by the d-orbitals of the transition metal ions located at the 'B' site. Due to the crystal field effect, these d-orbitals can split into different energy levels, resulting in various electronic configurations that influence the material's conductivity and magnetism. Magnetically, perovskites can exhibit a range of behaviors from ferromagnetism to antiferromagnetism. These behaviors are often dictated by double-exchange and superexchange interactions between the 'B' site cations mediated by the oxygen anions. In the case of double exchange, the crystal field splitting of the d-orbitals allows for electron hopping between mixed-valence 'B' site cations (e.g., $Co^{3+}$ and $Co^{4+}$ in cobaltites), facilitating ferromagnetic ordering. This mechanism relies on the overlap between the Co-3d and O-2p orbitals, which is sensitive to the degree of octahedral distortion and tilting.

Additionally, oxygen vacancies or other anion defects can lead to a lowering of the average valence state of the transition metal ions, such as Co in cobaltites. This changes the effective carrier density, influencing the electronic and magnetic behavior of the material. The presence of random oxygen vacancies can cause local variations in the valence states, disrupting the uniformity of the magnetic and electronic properties. This can result in reduced magnetic ordering or altered conductivity.

### 2.2.3. Brownmillerite structure

The Brownmillerite (BM) structure, named after the mineral Brownmillerite ($Ca_2(Al, Fe)_2O_5$) [72], is characterized by a distinctive arrangement where one oxygen atom is missing in every two unit cells compared to the conventional PV structure. Unlike PVs, which typically exhibit a random distribution of oxygen vacancies, BM compounds maintain an ordered pattern of oxygen vacancies within their lattice. This ordered vacancy arrangement, denoted by the formula $A_2B_2O_5$ (or equivalently $ABO_{2.5}$), places Brownmillerite (BM) within the broader category of ordered oxygen-deficient perovskites, which are described by the general formula

$A_nB_nO_{3n-1}$. Oxygen vacancy ordering (OVO) is observed across a range of compounds with $n$ values including 5, 4, 3, 2, 1.5, 1.33, and 1, corresponding to PV with varying oxygen contents of 2.80, 2.75, 2.67, 2.50, 2.33, 2.25, and 2.00, respectively (with the stoichiometric PV having $n = \infty$) [73, 74]. The relevant case in this thesis hence refers to n=2 in this generalized notation.

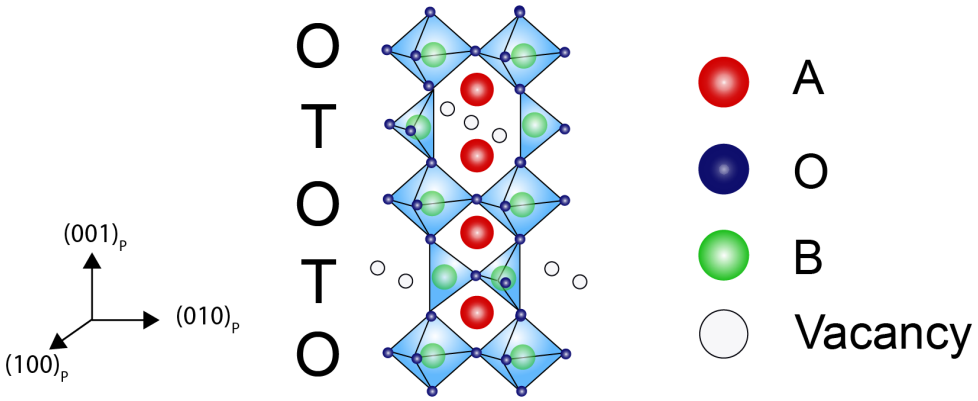


**Figure 2.10.:** Schematic of the Brownmillerite structure: Alternating octahedral and tetrahedral units with oxygen vacancies.

The BM structure is achieved by introducing rows of oxygen vacancies along the $(110)_P$ direction in every alternate $(001)_P$ plane, where the subscript P (Fig. 2.10) denotes directions within the cubic PV cell. Within the (001) layering of the PV structure, typically arranged as – AO – $BO_2$ – AO – $BO_2$ –, vacancies are selectively incorporated into the $BO_2$ planes. This arrangement results in alternating layers of $BO_2$ planes with varying oxygen content, leading to octahedral (O) and tetrahedral (T) coordination (Fig. 2.10), respectively. Thus, the stacking sequence in a BM is – AO – BO – AO – $BO_2$ –. The introduction of oxygen vacancies breaks the cubic symmetry of the original perovskite phase, resulting in an orthorhombic or tetragonal distortion. This symmetry-breaking distortion induces a 45° in-plane rotation of the BM unit cell with respect to the PV cell [32]. As a result, the in-plane lattice constants of the BM structure are larger by a factor of $\sqrt{2}$ compared to the perovskite structure. Consequently, the resulting tetragonal BM unit cell has the following dimensions:

$$a_{BM} = b_{BM} = \sqrt{2}b_{PV} \quad c_{BM} = 4a_{PV} \tag{2.25}$$

Here, $a_{BM}$, $b_{BM}$, and $c_{BM}$ represent the lattice parameters of the BM unit cell along the $a$, $b$, and $c$ axes, respectively, while $a_{PV}$ refers to the lattice parameter of the PV unit cell along the $a$ axis. One should also note that, due to the different chemical environment in the BM structure (including oxygen loss, changes in valence states, and variations in ion radius), an expansion of the lattice parameter $a_{PV}$ is expected.

Examples of BM structures include $LaCoO_{2.5}$ [75], which forms under reducing conditions, and

$La_{1-x}Sr_xMnO_{2.5}$ [76], produced through partial reduction of the parent PV. Other examples are $SrCoO_{2.5}$ [77], $BaInO_{2.5}$ [78], and $SrFeO_{2.5}$ [79]. In bulk LSCO, the formation of the BM phase under normal atmospheric conditions typically requires heavy Sr doping [80]. However, in $La_{0.6}Sr_{0.4}CoO_{3-\delta}$ thin films, the BM phase can emerge under reducing conditions, often facilitated by the effects of epitaxial strain [81–83].

The electronic and magnetic properties of the BM phase exhibit distinct characteristics compared to the PV phase, especially as the oxygen content varies. This variation influences the cation oxidation states, potentially leading to transitions between double exchange and superexchange interactions. Electronically, the BM phase often demonstrates insulating behavior due to ordered oxygen vacancies disrupting the electron conduction pathways. Magnetically, the transition from the PV structure to the BM structure leads to the collapse of the double-exchange mechanism, which is responsible for the ferromagnetic behavior in the PV phase. As this mechanism breaks down, ferromagnetism diminishes, and the BM phase typically exhibits antiferromagnetic or weak ferromagnetic ordering, as reported [84]. This change in magnetic behavior is due to the alternating octahedral and tetrahedral coordination sites in the BM structure, which disrupt the alignment of magnetic moments necessary for strong ferromagnetism. Therefore, by alternating between the PV and BM phases, one could potentially achieve tunable magnetic or electronic switching, allowing controlled transitions between conductive and insulating states or between ferromagnetic and antiferromagnetic states.

## 2.3. Oxygen diffusion and surface exchange

The movement of oxygen ions plays an important role in topotactic phase transitions and may significantly affect the transition rate and the overall timescale of the transition. Therefore, understanding the oxygen mass transport processes, specifically oxygen diffusion and oxygen surface exchange, is crucial. In this section, I will explain the basic principles of oxygen diffusion kinetics and surface exchange, and discuss the fundamental principles governing the topotactic phase transitions in this section.

### 2.3.1. Oxygen diffusion kinetics

In crystalline materials, point defects (like vacancies and interstitials) are the most energetically favourable mechanisms for atomic movement. In perovskites, intrinsic point defects primarily consist of oxygen or cation vacancies instead of interstitials. This is because the high packing density of the perovskite structure makes the formation of interstitials unfavorable. With the existence of point defects, the movement of oxygen ions within the lattice can be facilitated through diffusion and surface exchange mechanisms [48, 85].

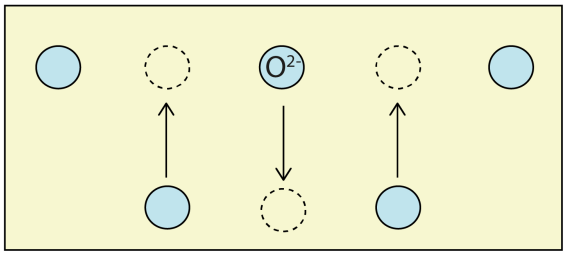


**Figure 2.11.:** Schematic representation of oxygen diffusion in perovskite oxides. Oxygen ions move through the lattice by hopping between oxygen vacancies, driven by thermal energy.

Oxygen diffusion in perovskite oxides mainly occurs within the bulk of the material. Initially, as described in Fig. 2.11, an oxygen ion is located at its regular lattice site. When a nearby oxygen vacancy is present, the ion can "hop" from its current site to the vacancy. This hopping process requires the ion to overcome a specific activation energy. As the oxygen ion moves into the vacancy, the vacancy shifts to the ion's previous position. Through repeated hopping events, either randomly or systematically across the lattice, oxygen ions effectively diffuse through the bulk [86]. The diffusion pathways in this case are typically determined by the arrangement of oxygen ions and vacancies within the lattice, occurring along the most energetically favorable routes. In perovskite structures, oxygen ions often diffuse along the (001) or (010) crystallographic directions [87].

A key parameter that characterizes the rate of oxygen diffusion is the diffusion coefficient ($D$). Since diffusion is a thermally activated process, the diffusion coefficient is typically modelled by the Arrhenius law, which describes its temperature dependence ($T$) as follows:

$$D = D_0 \exp\left(-\frac{E_a}{k_B T}\right) \tag{2.26}$$

In this equation, $D_0$ represents the pre-exponential factor, which corresponds to the diffusion coefficient at an infinitely high temperature, or equivalently, when the activation energy is negligible. The term $E_a$ denotes the activation energy for diffusion, reflecting the energy barrier that oxygen ions must overcome to move from one lattice site to another. Here, $k_B$ is the Boltzmann constant, and $T$ the temperature. The Arrhenius law describes, that at lower temperatures, the diffusion coefficient is small because oxygen ions have limited thermal energy, making it less likely for them to hop into neighboring vacancies. As the temperature increases, the ions acquire more energy, which enhances the frequency of successful hops, leading to a higher diffusion coefficient. Consequently, the diffusion coefficient increases exponentially with temperature. However, diffusion requires more than just thermal energy; a concentration gradient is the primary driving force behind net diffusion. In the absence of such a gradient, although individual oxygen ions may move due to random thermal motion, there will be no net mass transport. It is only when a concentration gradient exists—where oxygen ions are more concentrated in one region than another—that a net current of ions will flow, moving from areas of higher concentration to lower concentration, thus creating directional mass transport.

### 2.3.2. Oxygen surface exchange kinetics

In addition to diffusion, oxygen ions in the material also participate in a surface exchange process. This process involves the incorporation of oxygen from the surrounding environment (such as air or an oxygen-enriched atmosphere) into the material, as well as the release of oxygen from the material to the environment [88, 89]. The surface exchange process is fundamentally a redox reaction, as shown in Fig. 2.12, requiring electron transfer between the oxygen species. When an oxygen molecule ($O_2$) from the environment is incorporated into the material, it undergoes reduction, where electrons from the oxide's lattice are donated to the oxygen molecule, converting it into $O^{2-}$ ions that can then be integrated into the oxide lattice. Conversely, during oxygen release, $O^{2-}$ ions are oxidized, releasing electrons back to the material as the ions leave the lattice as neutral $O_2$ molecules. This exchange of electrons is crucial for the surface exchange process, as the transition between neutral oxygen and $O^{2-}$ ions allows oxygen incorporation and release. The rate of this process is characterized by the surface exchange coefficient ($k$). Like the diffusion coefficient, this rate can be quantitatively modeled by the Arrhenius law:

$$k = K_0 \cdot \exp\left(\frac{-E_a'}{k_B T}\right) \tag{2.27}$$

Here, $K_0$ represents the pre-exponential factor, while $E_a'$ denotes the activation energy for the oxygen exchange process. $k_B$ is the Boltzmann constant, and $T$ is the temperature. Similar to

oxygen diffusion, the surface exchange coefficient $k$ is strongly influenced by temperature. As expressed in Equation 2.27, an increase in temperature causes the exponential term to decrease (since $\frac{E'_a}{k_B T}$ becomes smaller), which in turn results in an increase in $k$. This indicates the typical enhancement of oxygen exchange rates at higher temperatures under certain oxygen partial pressures.

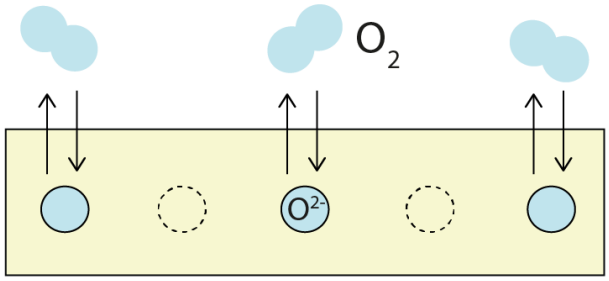


**Figure 2.12.:** Illustration of the oxygen surface exchange process in perovskite oxides. Oxygen molecules from the surrounding environment are incorporated into the material or released back into the atmosphere.

In addition to increasing the temperature, noble metals such as platinum and silver can significantly enhance the oxygen surface exchange rate in complex oxides. These noble metals act as catalysts by providing additional electronic states, facilitating the redox process at the surface. They donate electrons to oxygen molecules, aiding their incorporation into the oxide lattice, or accept electrons from $O^{2-}$ ions during the release of oxygen. By lowering the energy barrier for these oxygen exchange reactions, noble metals accelerate the overall surface exchange rate.

### 2.3.3. Rate-limiting process

At a given temperature and oxygen partial pressure, oxides typically strive to reach their thermodynamic equilibrium state, which may be either a (defective) perovskite or a brownmillerite structure, depending on the surrounding oxygen environment. Therefore, any change in the ambient oxygen partial pressure will initiate a dynamic process that includes both oxygen ion diffusion from/to the surface and oxygen surface exchange. In the particular case of an ion-triggered phase transition, this process also involves the growth of the new phase. Specifically, the phase boundary propagates as oxygen vacancies redistribute, causing regions of the brownmillerite phase to nucleate and expand. The movement of this phase boundary is similarly governed by thermally activated kinetics and can be described using an Arrhenius-type equation, as discussed in Fong's work on oxygen diffusion and phase boundary propagation [90].

In a system where oxygen diffusion, surface exchange, and nucleation of a new phase occur simultaneously, the overall rate at which oxygen is absorbed or released is governed by the slowest of these processes. For instance, if surface exchange and nucleation are slow but diffusion through the bulk is rapid, the surface exchange becomes the rate-limiting step, controlling how quickly oxygen enters or exits the material. Conversely, if surface exchange is fast but diffusion

and nucleation are slow, the oxygen transport will be limited by the slower bulk diffusion and nucleation processes.

To determine the rate-limiting step in a system, one can compare the activation energy of the overall process with reference activation energies for phase nucleation, oxygen diffusion, and surface exchange within the same or a similar system. The activation energy can be obtained by analyzing the relationship between the system's characteristic time and temperature. If the process follows Arrhenius behavior, this relationship will be linear, with a slope of $-\frac{E_a}{k_B}$, where $E_a$ is the activation energy and $k_B$ is the Boltzmann constant. This enables the calculation of the system's activation energy, which can then be compared to known values to identify the rate-limiting step. For further mathematical details, see Chapter 4.6.

It is important to note that the absolute values of the surface exchange coefficient ($k$) and the diffusion coefficient ($D$) can vary over several orders of magnitude. Therefore, under experimental conditions, either $k$ or $D$ could dominate the reaction kinetics, making it critical to evaluate both parameters. In certain cases, within a limited temperature range where both $k$ and $D$ contribute similarly to the time constants of the process, non-trivial relaxation behavior and deviations from Arrhenius-type behavior have been observed [91, 92]. These deviations highlight the complex interplay between diffusion and surface exchange kinetics, especially near phase transition boundaries.

## 2.4. Scattering theory

Scattering techniques are powerful, non-destructive tools for studying the structural and magnetic properties of materials. In this thesis, X-rays, neutrons, and electrons are utilized to probe and characterize the physical properties of complex oxide thin film systems. Polarized Neutron Reflectivity offers a unique advantage over X-ray Reflectivity as it allows simultaneous probing of both magnetic and structural properties. Moreover, the scattering cross-section for neutrons is particularly advantageous for probing lighter elements like oxygen content with higher accuracy compared to X-rays. This section will start with an overview of the basics of scattering, followed by a detailed discussion of more specialized topics, including diffraction, reflectivity, and polarized neutron reflectivity in the subsequent sections.

### 2.4.1. Basics of scattering

In this thesis, the scattering techniques employed are confined to elastic scattering, i.e. where the energy of the scattered beam remains equal to that of the incident beam. The discussion here is therefore focused on elastic scattering. The Fraunhofer approximation is typically used for the mathematical treatment of this process.

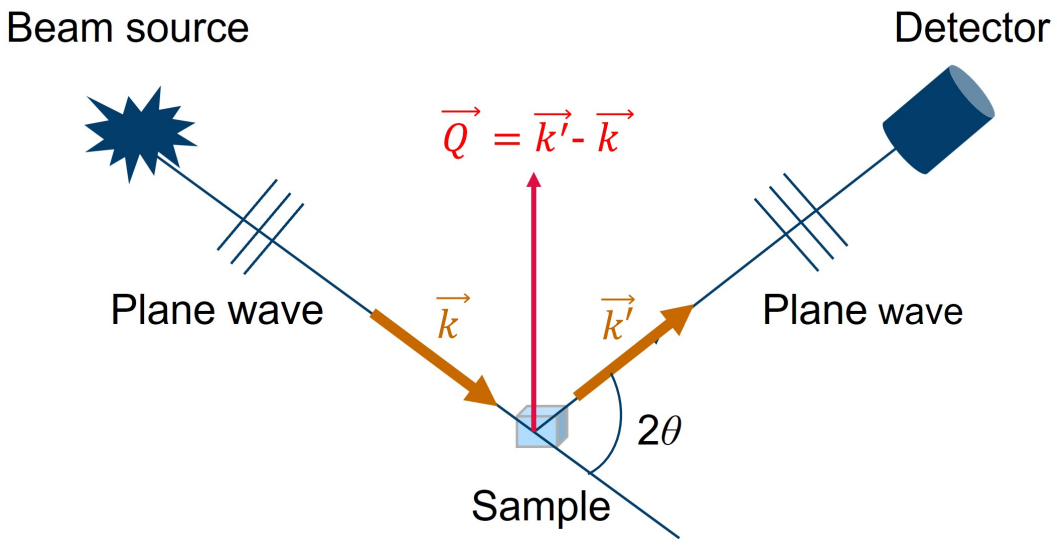


**Figure 2.13.:** Schematic representation of the scattering process in the Fraunhofer approximation. The incident plane wave with wave vector $\vec{k}$ interacts with the sample and is scattered into a wave with wave vector $\vec{k'}$. The scattering vector $\vec{Q}$ is defined as the difference vector between the scattered and incident wave vectors.

In the Fraunhofer approximation, the scattering process can be described using wave vectors, as illustrated in Fig.2.13. The wave vector of the incident beam is denoted by $\vec{k}$, while the wave vector of the scattered beam is $\vec{k'}$. The scattering vector $\vec{Q}$, is defined as the difference vector between these two vectors:

$$\vec{Q} = \vec{k'} - \vec{k} \tag{2.28}$$

The magnitude of the scattering vector $Q$ in an elastic scattering process can be expressed as:

$$Q = |\vec{Q}| = \sqrt{2k^2(1 - \cos(2\theta))} = \frac{4\pi}{\lambda}\sin(\theta) \tag{2.29}$$

where $k = \frac{2\pi}{\lambda}$ is the magnitude of the wave vector and $\lambda$ is the wavelength of the incident beam. The angle $\theta$ is the scattering angle, which is the angle between the incident and scattered beams.

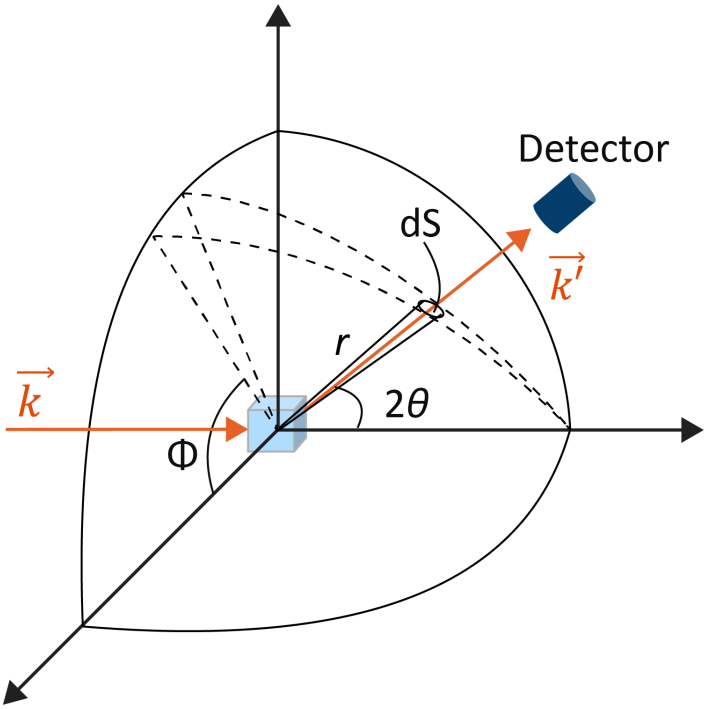


**Figure 2.14.:** Differential cross-section $\frac{d\sigma}{d\Omega}$ as a function of the scattering angle $\theta$. The total cross-section $\sigma$ is related to the area covered by the detector and the distance from the sample to the detector.

The scattered intensity is measured by a detector that covers a solid angle $d\Omega = \frac{dS}{r^2}$ (see Fig. 2.14), where $dS$ is the detector area and $r$ is the distance to the detector. The total cross-section $\sigma$ represents the total number of scattered particles integrated over all angles. Thus, $\frac{d\sigma}{d\Omega}$ represents the differential scattering cross-section, which describes how many particles are scattered into a particular solid angle for a given incident flux. This quantity can be understood as the probability per incident particle that it will be scattered into the solid angle $d\Omega$. It is defined as:

$$\frac{d\sigma}{d\Omega} = \frac{dn}{J d\Omega} \tag{2.30}$$

where $dn$ is the number of particles scattered into the solid angle $d\Omega$, and $J$ is the incident particle flux. The inclusion of $J$ ensures that we account for the total number of particles being

sent into the system; while the absolute number of scattered particles increases with $J$, the probability per particle (the differential cross-section) remains constant.

In order to connect experimental observations with scattering theory, it is necessary to define the scattering amplitude, which characterizes the interaction of waves with the sample. Within the framework of Born approximation, the scattering amplitude is expressed as:

$$A(\overrightarrow{Q}) \propto A_0 \cdot \int \rho_s(\overrightarrow{r}) \cdot e^{i\overrightarrow{Q}\cdot\overrightarrow{r}}\, d^3r, \tag{2.31}$$

where $A_0$ represents the amplitude of the incident wave, and $\rho_s(\overrightarrow{r})$ is the scattering density at position $\overrightarrow{r}$. This expression explains how the scattering amplitude depends on the spatial distribution of the scattering density and the scattering vector $\overrightarrow{Q}$.

At the microscopic level, the scattering process is described using quantum mechanics. By solving the Schrödinger equation for the system, one can derive that the differential cross-section is related to the scattering amplitude $A(\overrightarrow{Q})$ through the following relationship:

$$\frac{d\sigma}{d\Omega} \propto |A(\overrightarrow{Q})|^2. \tag{2.32}$$

On the other hand, the scattered intensity $I(\overrightarrow{Q})$ is also related to the differential cross-section through the following relationship:

$$I(\overrightarrow{Q}) \propto \frac{d\sigma}{d\Omega}. \tag{2.33}$$

Thus, the scattering intensity is proportional to the square of the scattering amplitude:

$$I(\overrightarrow{Q}) \propto |A(\overrightarrow{Q})|^2. \tag{2.34}$$

By measuring the scattered intensity $I(\overrightarrow{Q})$ and comparing it to theoretical models of $A(\overrightarrow{Q})$ as shown in Equation 2.31, one can extract the scattering density $\rho_s(\overrightarrow{r})$ and other structural parameters of the sample.

### 2.4.2. X-ray diffractometry

X-ray diffraction is a powerful technique for determining the crystalline structure of a sample. There are two key principles underlying X-ray diffraction. The first principle is that it relies on the elastic (Thomson) scattering of photons. In this process, the incident X-ray photon is scattered by an electron, but the wavelength of the X-ray remains unchanged; only the direction of propagation is altered, as illustrated in Fig. 2.15.

The second principle is that the wavelength of X-rays is comparable to the interatomic distances

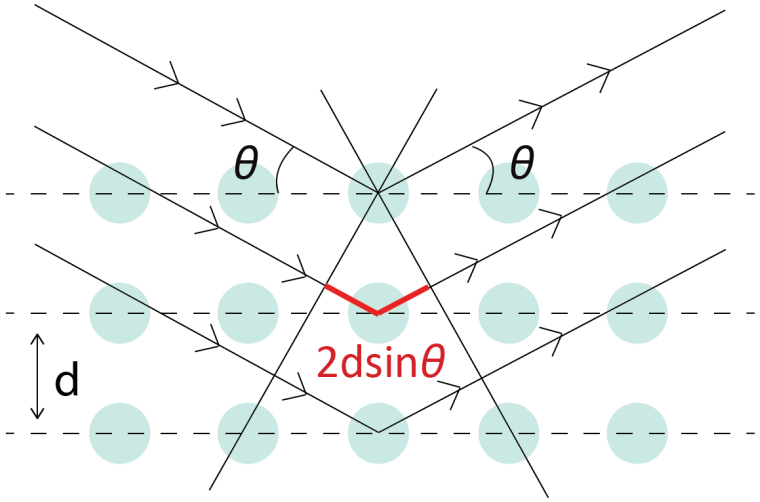


**Figure 2.15.:** Schematic representation of X-ray diffraction, illustrating how incident X-rays interact with a crystal lattice.

in crystals, which typically range from 0.15 to 0.5 nm [93]. This similarity in scale results in constructive and destructive interference phenomena. These interference effects are quantitatively described by Bragg's law, which states that constructive interference occurs when the path difference between X-rays scattered from successive crystal planes is an integer multiple of the wavelength $\lambda$ [94]:

$$n\lambda = 2d_{hkl}\sin\theta \tag{2.35}$$

where: $n$ is the order of reflection, $\lambda$ is the wavelength of the incident X-ray, $d_{hkl}$ is the interplanar spacing for planes with Miller indices $hkl$, $\theta$ is the angle of incidence (also known as the Bragg angle).

In reciprocal space, Bragg's equation corresponds to the Laue condition. The Laue condition can be mathematically expressed as:

$$\vec{Q} = \vec{G} \tag{2.36}$$

Here, $\vec{G}$ represents the Laue vector, which corresponds to a reciprocal lattice vector and is associated with the periodicity of the crystal structure. It can be visualized within Ewald's sphere, as depicted in Fig. 2.16. Each point on this sphere corresponds to a specific set of crystal planes, with the distance between these points being inversely proportional to the spacing between the planes in real space.

The Laue vector $\vec{G}_{hkl}$, associated with the Miller indices $(hkl)$, is defined as [95]:

$$\left|\vec{G}_{hkl}\right| = \frac{2\pi}{d_{hkl}} = \left|h\,\vec{b}_1 + k\,\vec{b}_2 + l\,\vec{b}_3\right| \tag{2.37}$$

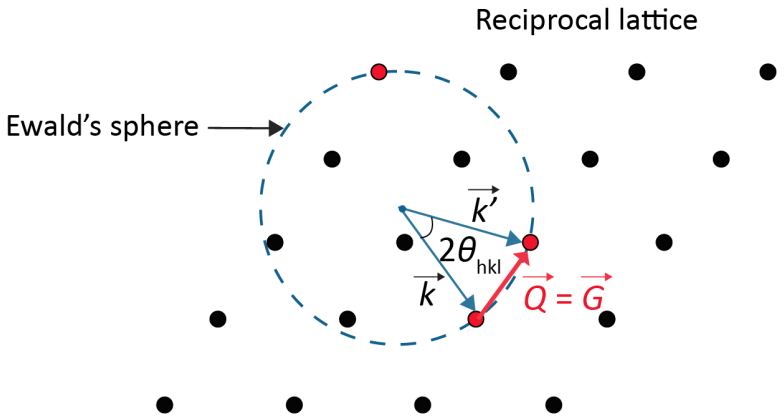


**Figure 2.16.:** Ewald's sphere construction in reciprocal lattice (Laue condition).

Here, $\vec{b}_1$, $\vec{b}_2$, and $\vec{b}_3$ are the reciprocal lattice primitive vectors. These vectors are related to the real-space primitive vectors $\vec{a}_1$, $\vec{a}_2$, and $\vec{a}_3$ through the following relationships:

$$\vec{b}_1 = \frac{2\pi\left(\vec{a}_2 \times \vec{a}_3\right)}{\vec{a}_1 \cdot \left(\vec{a}_2 \times \vec{a}_3\right)}, \quad \vec{b}_2 = \frac{2\pi\left(\vec{a}_3 \times \vec{a}_1\right)}{\vec{a}_2 \cdot \left(\vec{a}_3 \times \vec{a}_1\right)}, \quad \vec{b}_3 = \frac{2\pi\left(\vec{a}_1 \times \vec{a}_2\right)}{\vec{a}_3 \cdot \left(\vec{a}_1 \times \vec{a}_2\right)} \tag{2.38}$$

In X-ray diffraction, the angle $2\theta$ is varied by adjusting the incident angle of the X-rays and the detector position relative to the sample. This variation allows the diffractometer to scan different values of the scattering vector $\vec{Q}$, which correspond to different lattice planes within the crystal. As the incident angle changes, the X-rays interact with various planes, producing diffraction peaks when the Bragg condition is satisfied. This enables us to obtain structural details such as lattice spacing and symmetry, based on the relationships from Eq. 3.1 to 2.38. The scattering cross-section, introduced earlier in the general discussion of scattering, is measured through the intensity of the diffracted beams. In X-ray diffraction, the intensity of these diffracted beams is related to the probability of scattering events occurring and can be used in determining the electron density distribution within the crystal.

### 2.4.3. Polarized neutron reflectivity

Polarized neutron reflectivity (PNR) is a powerful technique for investigating both the structural and magnetic properties of thin films. In contrast to X-rays, which interact primarily with the electron clouds and probe the electron scattering density, neutrons interact with both the nuclei and magnetic moments within the material. Consequently, neutron reflectivity can probe not only the nuclear scattering density but also the magnetic scattering density. It typically involves using a very small incident angle, usually within a few degrees or less. A typical reflection geometry on a flat surface is illustrated in Fig. 2.17, where the incident angle is equal to the reflection angle. When the incident angle is below the critical angle $\theta_c$, the neutron beam undergoes total reflection. The critical angle is defined as:

$$\theta_c = \arcsin\left(\frac{1}{n}\right), \quad \theta_c \simeq \lambda\sqrt{\frac{n_{\mathrm{SLD}}}{\pi}} \tag{2.39}$$

where $\lambda$ is the wavelength of the neutron beam, $n$ is the refractive index of the sample(as shown in Fig. 2.17) and $n_{\mathrm{SLD}}$ is the nuclear scattering length density for neutrons. Thus, the larger the $n_{\mathrm{SLD}}$ of a material, the larger the critical angle $\theta_c$.

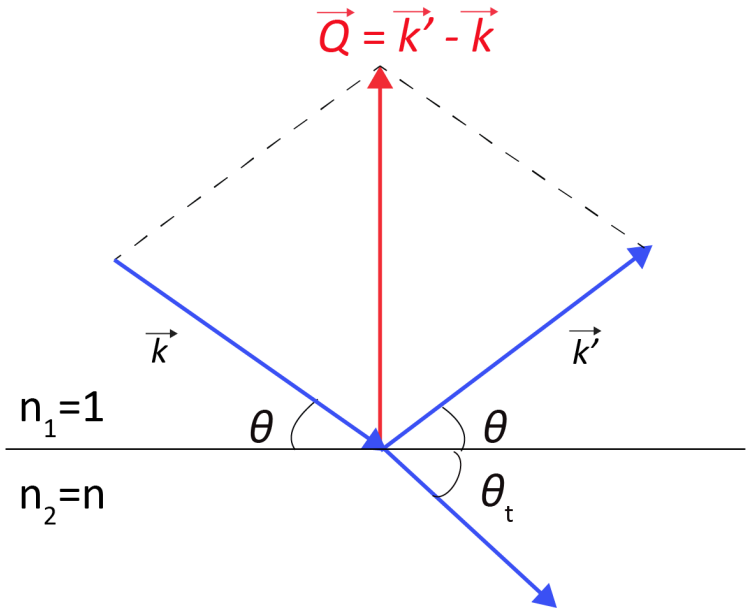


**Figure 2.17.:** Geometry of a neutron reflectivity experiment.

When the incident angle exceeds the critical angle $\theta_c$, the beam can partially transmit through the sample. Assuming an ideal, smooth surface, the reflection $R$ and transmission $T$ coefficients can be calculated using the Fresnel formulas:

$$R = \left|\frac{\theta - n\theta_t}{\theta + n\theta_t}\right|^2 \tag{2.40}$$

$$T = \left|\frac{2\theta}{\theta + n\theta_t}\right|^2 \tag{2.41}$$

where $n$ is the index of refraction of the material, and $\theta_t$ is the angle of the transmitted beam.

The interaction of neutrons with the material results in a scattering potential that is essential for understanding their behavior during reflectivity experiments. This potential encompasses both the scattering length density and the magnetic moment interactions. The scattering potential for neutrons is given by:

$$V(\vec{r}) = \frac{2\pi\hbar^2}{m}\rho_N b - \gamma_n \mu_N \vec{\sigma} \cdot \vec{B} \tag{2.42}$$

Here, the first term represents the nuclear potential, where $\rho_N$ is the nuclear scattering length density, which quantifies the number of nucleons (protons and neutrons) per unit volume and

influences how neutrons scatter elastically off nuclei, and $b$ is the scattering length, indicating the strength of the interaction between neutrons and the target nuclei. The variable $m$ denotes the mass of the neutron. The second term accounts for the magnetic component of the scattering potential. In this term, $\gamma_n$ is the gyromagnetic ratio for neutrons ($\gamma_n = -1.913$), $\mu_N$ is the nuclear magneton, $\vec{B}$ is the magnetic flux density, and $\vec{\sigma} = \{\hat{\sigma}_x, \hat{\sigma}_y, \hat{\sigma}_z\}$ denotes the spin operator composed of Pauli matrices. It is important to note that in a ferromagnetic sample, the aligned spins can create a non-zero term for $\vec{\sigma} \cdot \vec{B}$, even without an external magnetic field.

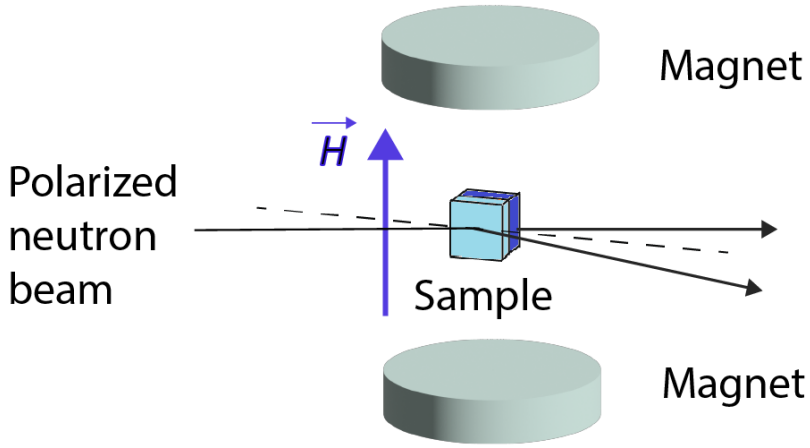


**Figure 2.18.:** Typical setup of the neutron reflectivity experiment, where $\vec{H}$ represents the magnetic field.

The typical setup of a polarized neutron reflectivity experiment is illustrated in Fig. 2.18. In this setup, the sample is placed between two magnets that generate a magnetic field. The incoming neutron beam is polarized either parallel or anti-parallel to this magnetic field. These two polarization states, $\psi_+(\mathbf{r})$ and $\psi_-(\mathbf{r})$, correspond to "spin-up" and "spin-down" relative to the quantization axis.

Given that the total energy of the neutron is $E = \frac{\hbar^2 k_0^2}{2m}$, the three-dimensional Schrödinger equation for the neutron wave function can be expressed as follows:

$$\psi_+''(z) + \left[k_z^2 - 4\pi b\rho_N + \frac{2m\gamma_n\mu_n}{\hbar^2}B_\parallel\right]\psi_+(z) + \frac{2m\gamma_n\mu_n}{\hbar^2}B_\perp\psi_-(z) = 0 \tag{2.43}$$

$$\psi_-''(z) + \left[k_z^2 - 4\pi b\rho_N - \frac{2m\gamma_n\mu_n}{\hbar^2}B_\parallel\right]\psi_-(z) + \frac{2m\gamma_n\mu_n}{\hbar^2}B_\perp\psi_+(z) = 0 \tag{2.44}$$

Here, $B_\parallel$ and $B_\perp$ represent the components of the magnetic field in the sample that are parallel and perpendicular to the neutron guide field, respectively.

When considering the parallel component $B_\parallel$ in the equations, the differential equations for the spin-up and spin-down wave functions become decoupled. This decoupling means that the nuclear and magnetic scattering intensities are observed in what are known as the non-spin-flip

channels. Specifically, in the spin-up channel (denoted as $R^{++}$), the reflected intensity includes the sum of both the nuclear and magnetic contributions. In contrast, the spin-down channel ($R^{--}$) shows the difference between the nuclear and magnetic contributions. For instance, in a ferromagnetic system under a saturating magnetic field, the field aligns all magnetic moments, making the magnetic term significant. The term associated with $B_{\parallel}$ is non-zero, leading to enhanced reflected intensity from both nuclear and magnetic scattering. In this case, $B_{\perp}$ is negligible. Conversely, in a non-ferromagnetic system, due to the lack of long-range magnetic order, the magnetic contribution is weak or absent. As a result, the term related to $B_{\parallel}$ is effectively zero, and the reflected intensities in both spin channels mainly reflect nuclear scattering alone.

For the perpendicular component $B_{\perp}$, if $B_{\perp} \neq 0$, the differential equations remain coupled, leading to spin-flip events. In these spin-flip channels, the reflected intensity contains pure magnetic information, allowing signals that directly correspond to the magnetic properties of the sample to be observed. Thus, polarized neutron reflectivity can act as a tool in studying both the nuclear and magnetic depth profiles for thin film systems.

Thus, polarized neutron reflectivity can act as a tool in studying both the nuclear and magnetic depth profiles for thin film systems. This capability makes PNR particularly useful for detecting compositional changes within the film, such as variations in oxygen content. In perovskite oxide thin films, where the oxygen stoichiometry can vary from 2.5 to 3, PNR allows precise characterization of oxygen content by fitting the nuclear scattering length density. However, this method relies on the assumption that oxygen is the only element with variable stoichiometry within the thin film and that the thin film exhibits a significantly higher scattering density than the substrate. Consequently, the measured scattering length density is primarily influenced by the thin film itself.

Nuclear scattering density quantifies the effectiveness of neutron interactions with atomic nuclei in a material. It is defined as the sum of the scattering lengths of all nuclei within a given volume. A higher nuclear scattering density indicates stronger scattering. The nuclear scattering length density, $n_{\mathrm{SLD}}$, can be expressed as:

$$n_{\mathrm{SLD}} = \rho_N \cdot b_{\mathrm{nuclear}} \tag{2.45}$$

In this equation, $\rho_N$ represents the nuclear number density, and $b_{\mathrm{nuclear}}$ is the average nuclear scattering length of the constituent elements.

Moreover, the nuclear scattering length density can also be expressed in terms of the individual elemental scattering lengths, $b_i$, weighted by their stoichiometric coefficients, $c_i$, and normalized by the volume of the unit cell, $V_m$. For example, in the case of the material $La_{0.6}Sr_{0.4}CoO_{3-\delta}$:

$$n_{\mathrm{SLD}} = \frac{\sum_i b_i \cdot c_i}{V_m} = \frac{0.6 \cdot b_{\mathrm{La}} + 0.4 \cdot b_{\mathrm{Sr}} + b_{\mathrm{Co}} + (3-\delta) \cdot b_{\mathrm{O}}}{V_m} \tag{2.46}$$

Here, $b_{\mathrm{La}}$, $b_{\mathrm{Sr}}$, $b_{\mathrm{Co}}$, and $b_{\mathrm{O}}$ denote the nuclear scattering lengths of La, Sr, Co, and O atoms, respectively. These values are constants, while $\delta$ and $\frac{1}{V_m}$ serve as the fitting variables. By fitting $n_{\mathrm{SLD}}$, one can accurately extract the oxygen content in the thin film system." improve it and find the connection between the two equations.

It is important to note that if multiple elements in the system exhibit variable stoichiometry, PNR is not a suitable method for determining oxygen stoichiometry, as fitting multiple variables would result in high uncertainty. Additionally, if the substrate has a higher $n_{\mathrm{SLD}}$ than the thin film, the method would not accurately reflect the oxygen content of the film, since the $n_{\mathrm{SLD}}$ would be dominated by the substrate. However, these limitations do not apply to systems like $La_{0.6}Sr_{0.4}CoO_{3-\delta}$, which has a higher $n_{\mathrm{SLD}}$ than the substrate even in the Brownmillerite phase and maintains constant A-site and B-site stoichiometry. This makes it an ideal candidate for determining oxygen stoichiometry using polarized neutron reflectivity.

# 3. Experimental methods

In this chapter, I will describe the experimental techniques used to investigate the structural, electronic, chemical, and magnetic properties of the materials studied in this thesis. The methods outlined in the following sections include Pulsed Laser Deposition for the growth of thin films; Atomic Force Microscopy for surface topography and roughness analysis; X-ray Diffraction and Reciprocal Space Mapping for structural characterization and crystallographic information; Polarized Neutron Reflectivity for probing depth-dependent magnetic and structural profiles and determining the oxygen content; electronic transport measurements using the Physical Properties Measurement System to evaluate electrical conductivity and related properties; Superconducting Quantum Interference Device magnetometry for magnetic characterization of materials; and Rutherford Backscattering Spectrometry and X-ray Photoelectron Spectroscopy for chemical composition analysis.

## 3.1. Pulsed laser deposition

Pulsed Laser Deposition (PLD) is a thin-film deposition technique that involves the use of high-energy laser pulses to ablate material from a target and deposit it onto a substrate. This method is particularly valued for oxide materials for its ability to produce high-quality, epitaxial thin films with precise control over composition and thickness.

In PLD (see Fig. 3.1), a high-energy UV laser is directed at a ceramic target within a specially designed chamber with low oxygen partial pressure. The laser pulses strike the target, generating a plasma (ionized gas). This plasma then travels towards a nearby substrate, the surface on which the film will be deposited. As the plasma reaches the substrate, the material from the target is deposited onto it, forming a thin film.

The kinetic energy of the ablated species (atoms or molecules that are ejected or ablated from the target material) during Pulsed Laser Deposition is influenced by their collisions with ambient gas molecules, which are affected by the partial pressure of oxygen in the chamber. These interactions determine the energy distribution of the particles as they travel towards the substrate. After interacting with the oxygen molecules, a portion of these particles reaches the substrate surface and adheres to it. The substrate typically exhibits a step-terrace morphology, resulting in an anisotropic energetic landscape where certain sites are more favorable for nucleation and film growth. To facilitate the mobility of adatoms and adsorbed species (adspecies)

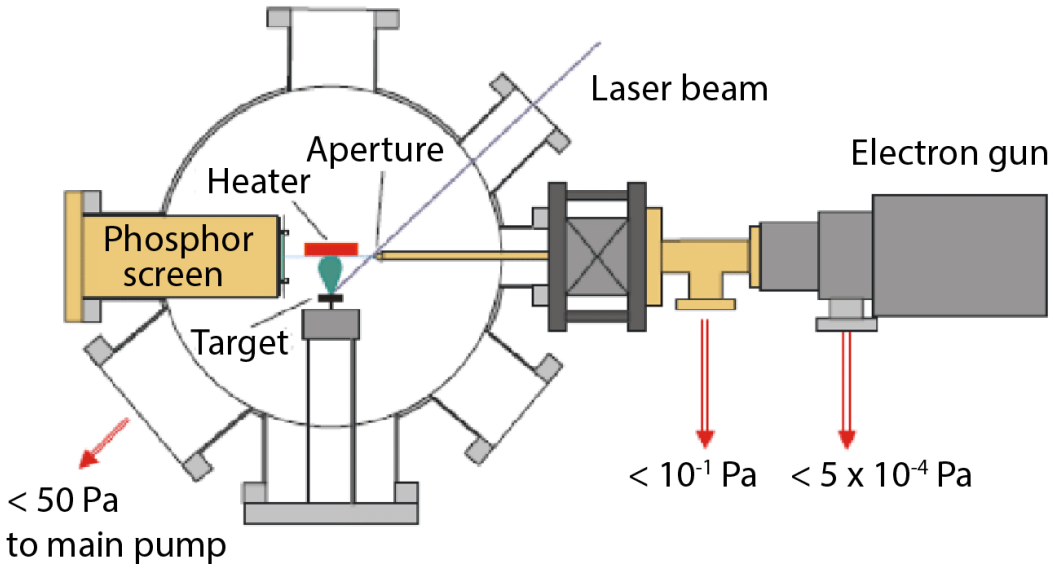


**Figure 3.1.:** Schematic illustration of the PLD setup (taken from [96]). A high-energy laser is directed at a ceramic target inside a vacuum chamber with a controlled oxygen atmosphere, generating a plasma plume. The plasma travels toward the substrate, where the ablated material is deposited, forming a thin film.

along the surface, the substrate is heated, providing the necessary thermal energy for surface diffusion. Therefore, the growth dynamics of the thin film is governed by the kinetic energy of the mobile adspecies, the surface energy of the substrate, and the interface energy between the substrate and the thin film material. [97]

By optimizing the growth parameters, such as temperature, pressure, and laser energy, one can achieve a uniform deposition of material in epitaxial growth. In this process, the deposited material replicates the atomic structure of the crystalline substrate, facilitating the growth of a high-quality, single-crystalline thin film. A key factor in achieving successful epitaxial growth is the use of a substrate with a crystal structure that is compatible with the thin film material, such as using a perovskite substrate for the growth of perovskite thin films. Even though the target material may consist of multiple grains with random crystallographic orientations, epitaxial growth enables the formation of a thin film with a uniform, single-crystal structure.

**Reflection high-energy electron diffraction (RHEED)** is employed to monitor the growth of thin films during Pulsed Laser Deposition. In this technique, a high-energy electron beam is directed at a very shallow angle onto the surface of the substrate. The high-energy electrons interact with the surface atoms, producing a diffraction pattern that is projected onto a phosphor screen. By analyzing changes in this diffraction pattern, particularly the intensity oscillations, RHEED provides real-time feedback on the growth process, allowing for precise control of deposition parameters and ensuring the formation of high-quality, atomically smooth thin films.

The growth mode of a thin film depends not only on the mobility of the adspecies but also on thermodynamic factors. When adspecies possess a large mobility, they can spread easily across

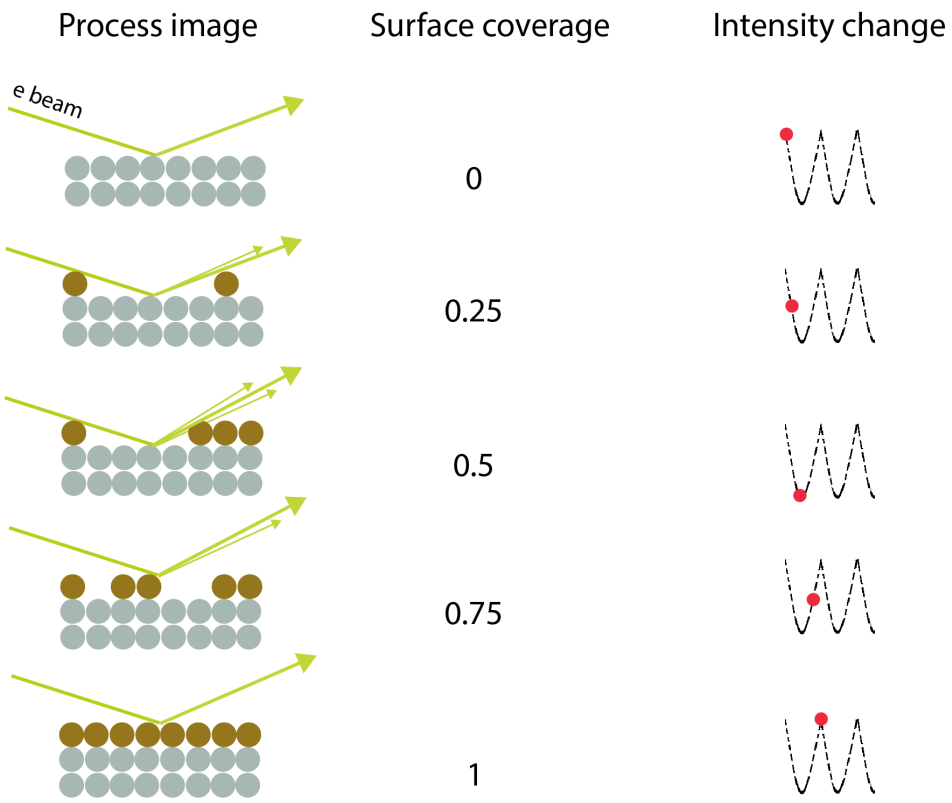


**Figure 3.2.:** RHEED monitoring of thin film growth: Electrons are directed at a grazing angle onto the film surface, with the diffracted signal reflecting changes in surface coverage during deposition and nucleation. The evolution of intensity provides real-time information into the growth process.

the substrate surface, leading to two-dimensional (2D) layer-by-layer growth, i.e. Frank-van-der-Merwe growth. In this mode, the adspecies migrate to energetically favorable sites, such as step edges, forming a complete atomic layer before the next layer begins to grow. If mobility is exceptionally high, adspecies can diffuse continuously along step edges, resulting in step-flow growth, where distinct layers are not visible. As the mobility decreases, nucleation may occur before the underlying monolayer is complete, leading to Stranski-Krastanov growth, where three-dimensional (3D) islands form on top of existing terraces. When mobility is very low, island formation becomes more pronounced, resulting in Volmer-Weber growth, characterized by distinct 3D islands rather than continuous layers. Additionally, thermodynamic factors, such as the interface energy between the thin film and substrate, can also drive three-dimensional growth. For instance, if the interface energy is large, three-dimensional growth can occur even if adspecies mobility is sufficient for two-dimensional growth. In some cases, such as at room temperature where mobility is minimal, smooth films may still form due to favorable interface energies, preventing the development of 3D structures. [98–101]

Since RHEED intensity responds to changes in step density [102] (such as step ledges, nucleation sites, and 3D islands) which are related to surface coverage, it enables precise tracking of growth with monolayer accuracy (see Fig. 3.2). In layer-by-layer growth, one can observe distinct intensity oscillations as each new layer forms. During step flow growth, the step density remains

steady, resulting in a constant RHEED intensity. However, when 3D islands form, the pattern changes, and the RHEED intensity decreases due to increased surface roughness.[103]

## 3.2. Atomic Force Microscopy

Atomic Force Microscopy (AFM) in tapping mode (AC-mode) was used to characterize the surface morphology of the substrates and thin film samples (*Cypher AFM*, *Oxford Instruments Asylum Research Inc.*). The key components of an AFM system include a sharp tip, a flexible cantilever, a laser diode, a photodetector, and a piezoelectric transducer/scanner (as shown in Fig. 3.3). Its working principle relies on the interaction between the tip and the sample surface. In detail, when the AFM tip scans the surface, forces between the tip and the sample (such as Van der Waals forces, electrostatic forces, or chemical forces) cause the cantilever to bend or deflect. These minute deflections are detected using laser reflection: a laser beam is directed onto the back of the cantilever and reflected onto the photodetector. By analyzing the deflections, AFM can map the height and morphology of the sample's surface.[104]

In tapping mode, the cantilever oscillates near its resonance frequency, and the interaction between the probe and the sample modifies the amplitude and the phase of the oscillation [105]. These parameters reflect surface characteristics such as roughness and mechanical properties (hardness, elasticity, etc.). A feedback system continuously adjusts the distance between the probe and the sample to maintain a stable interaction. Thus, this mode allows for the determination of both surface morphology and phase information of the sample.

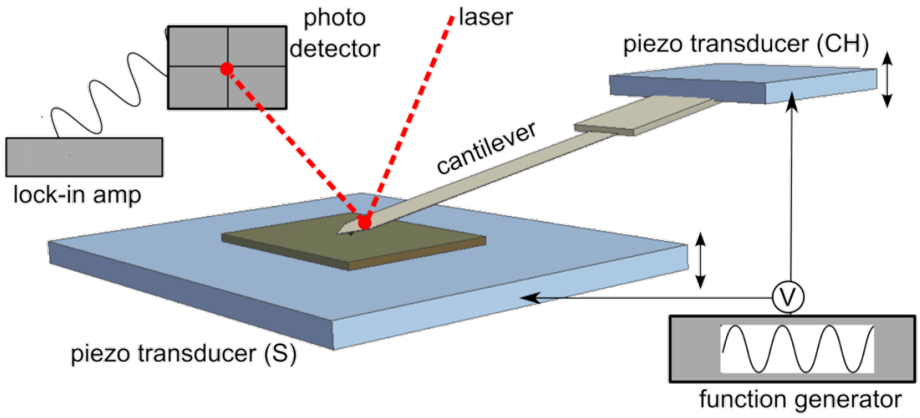


**Figure 3.3.:** Schematic illustration of an atomic force microscope, adapted from [106].

In this thesis, silicon tips with a curvature of less than 8 nm were employed for surface analysis. Typically, a scan frequency between 1.0 and 1.7 Hz was used to capture 512-pixel images, with a scan range of $5\,\mu\text{m} \times 5\,\mu\text{m}$. The topographical data obtained were analyzed with a focus on atomic scale features using *Gwyddion* version 2.52. The analysis involved linear and polynomial background corrections to eliminate noise and artifacts while enhancing image clarity and contrast. Specifically, this process included plane leveling to correct overall tilt, median alignment to address small-scale irregularities, and setting the (z)-zero level on a step terrace to ensure accurate height measurements.

## 3.3. X-ray diffraction

X-ray diffraction (XRD) is a very useful technique for investigating the structure of thin films. The working principle of this technique is that when X-rays interact with the thin film, they are scattered by the electron orbitals of individual atoms, creating a diffraction pattern that reflects the periodic arrangement of atomic planes within the crystal. This scattering results in constructive and destructive interference, which manifests as a diffraction pattern. Analyzing this pattern provides information about the crystal structure and allows e.g. for the measurement of the interplanar spacings.

As outlined in Section 2.4.2, Bragg's law provides the relationship between the angle of X-ray incidence and the crystal lattice spacing. Its mathematical expression is given by:

$$n\lambda = 2d_{hkl}\sin\theta \tag{3.1}$$

where $n$ denotes the order of reflection, $\lambda$ represents the wavelength of the incident X-rays, $d_{hkl}$ is the interplanar spacing for planes with Miller indices $hkl$, and $\theta$ is the angle of incidence, also known as the Bragg angle. By adjusting $2\theta$, the lattice parameter can be easily calculated.

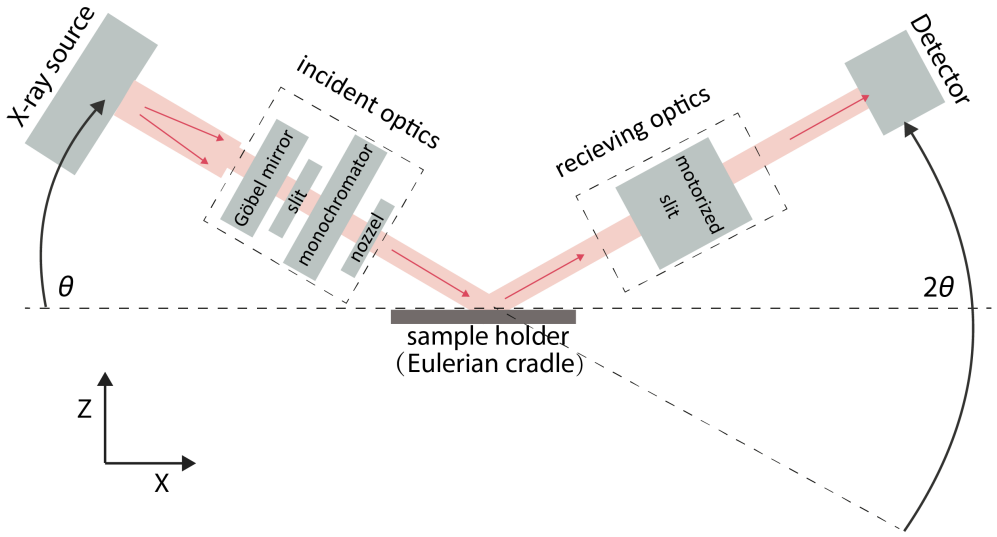


**Figure 3.4.:** Schematic of the Bruker AXS D8 Advance X-ray reflectometer setup.

In this thesis, XRD measurements were performed using a Bruker AXS D8 Advance X-ray reflectometer, as shown in Fig. 3.4. The setup includes several key components. The X-ray source is a Cu source, generating Cu-K$\alpha_1$, Cu-K$\alpha_2$, Cu-K$\beta$, and continuous Bremsstrahlung radiation. After passing through the monochromator, the beam is primarily Cu-K$\alpha_1$ radiation at 1.54 Å. The incident optics, including slits, a nozzle, a Göbel mirror, and the monochromator, focus and monochromatize the X-ray beam. The sample holder features an Eulerian cradle that allows for tuning height ($z$), rotation ($\Phi$), and tilt ($\Psi$) adjustments, enabling positioning and alignment of the sample. The receiving optics, equipped with a motorized slit, collect and direct the diffracted X-rays toward the detector. The LYNXEYE XE detector is a 1D stripe

detector, which enables fast measurements for Reciprocal Space Mapping.

During the measurement, the thin films were aligned by adjusting the sample height ($z$), rotation ($\Phi$), and tilt ($\Psi$) using rocking curve analysis centered around the (002) diffraction peak of the substrate. Measurements were conducted in high-resolution mode. A divergence slit of 0.6 mm was used on the primary side of the incident optics, while the motorized secondary slit was set to 0.8 mm. The linear opening of the detector was adjusted to 0.6 mm, corresponding to 8 channels of the detector array. In $2\theta$-$\omega$ scan, measurements were taken with a 0.01° increment and a 1-second duration per step. For XRD rocking curve analysis, the $2\theta$ and $\omega$ positions of the motors were aligned to the maximum of the (002) thin film signal. Both XRD and rocking curve measurements were carried out in 0D detector mode. Reciprocal space mapping (RSM) around the asymmetric (013) diffraction peak was performed in grazing exit geometry using the 1D detector mode, with the motorized secondary slit fully open at 9.5 mm and the linear opening of the detector set to 14.325 mm.

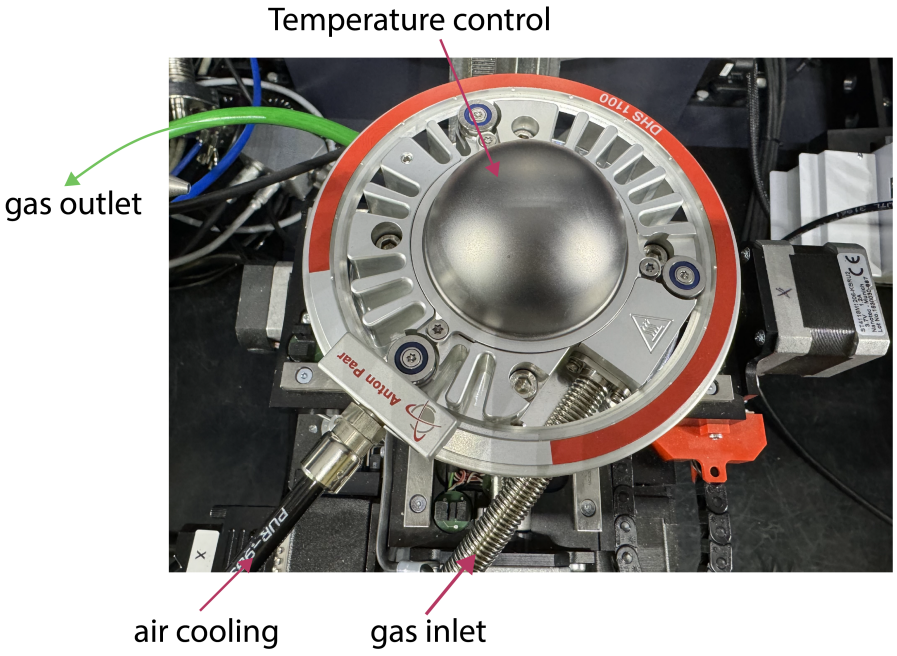


**Figure 3.5.:** High-temperature XRD setup: The sample is positioned on a ceramic plate, which is heated from the backside and enclosed by a graphite dome. Temperature control is achieved with pressurized air, and the ambient atmosphere is regulated using a continuous flow of either oxygen or a 4% hydrogen/argon gas mixture.

*In-situ* high-temperature X-ray diffraction (HT-XRD) experiments were conducted using a closed graphite chamber (Anton Paar DHS 1100 Domed Hot Stage), which provided control of both temperature and gas flow, as shown in Fig. 3.5. The process starts by placing the thin film samples onto the sample stage and fixing them in place with clips to ensure stability during the experiment. Temperature control is achieved by heating the ceramic plate from the backside, while air cooling was used to ensure thermal stability throughout the experiment. To maintain a stable atmospheric environment around the sample, a constant gas flow of 0.1 LPM was applied. When changes in the oxygen partial pressure were required, such as during

the sample reduction process, a higher gas flow rate of around 0.5 LPM is used. This faster gas flow facilitates quick gas exchange within the dome. Before starting the high-temperature measurements, the sample is carefully aligned using the (002) diffraction peak of the substrate at room temperature and at the target temperature, ensuring reproducible data collection throughout the experiment.

The following outlines the details involved in the HT-XRD measurement: Initially, the sample is aligned at room temperature using the (002) diffraction peak of the STO substrate. After increasing the temperature, the thermal expansion of the STO substrate is accounted for. The out-of-plane lattice parameter at the target temperature is calculated based on the lattice expansion coefficient. Using this calculated lattice constant, adjustments are made to the angle of the (002) diffraction peak to ensure proper alignment of the sample at elevated temperatures. This alignment process is essential for obtaining reproducible diffraction data. Additionally, measurement times were kept consistent across varying temperatures to ensure the comparability of results.

## 3.4. Polarized Neutron Reflectivity

The magnetic depth profiles of the thin film samples were investigated by polarized neutron reflectometry (PNR). In this thesis, PNR measurements were carried out at the Magnetism Reflectometer MAGREF at BL-4A [107] at the Spallation Neutron Source (SNS), Oak Ridge National Laboratory, USA.

The aim of a neutron specular reflectivity experiment is to measure the reflectivity as a function of the scattering wave vector $Q$ perpendicular to the sample surface:

$$Q = \frac{4\pi}{\lambda} \sin\theta \tag{3.2}$$

In a pulsed, time-of-flight (TOF) based neutron experiment, measurements are conducted by varying the wavelength $\lambda$ of the neutrons, which is determined by their time of flight from the pulsed source. The angle of incidence $\theta$ on the sample can be fixed, with the TOF approach allowing precise energy and wavelength analysis (see Chapter 2.4 for a detailed discussion of the scattering mechanism).

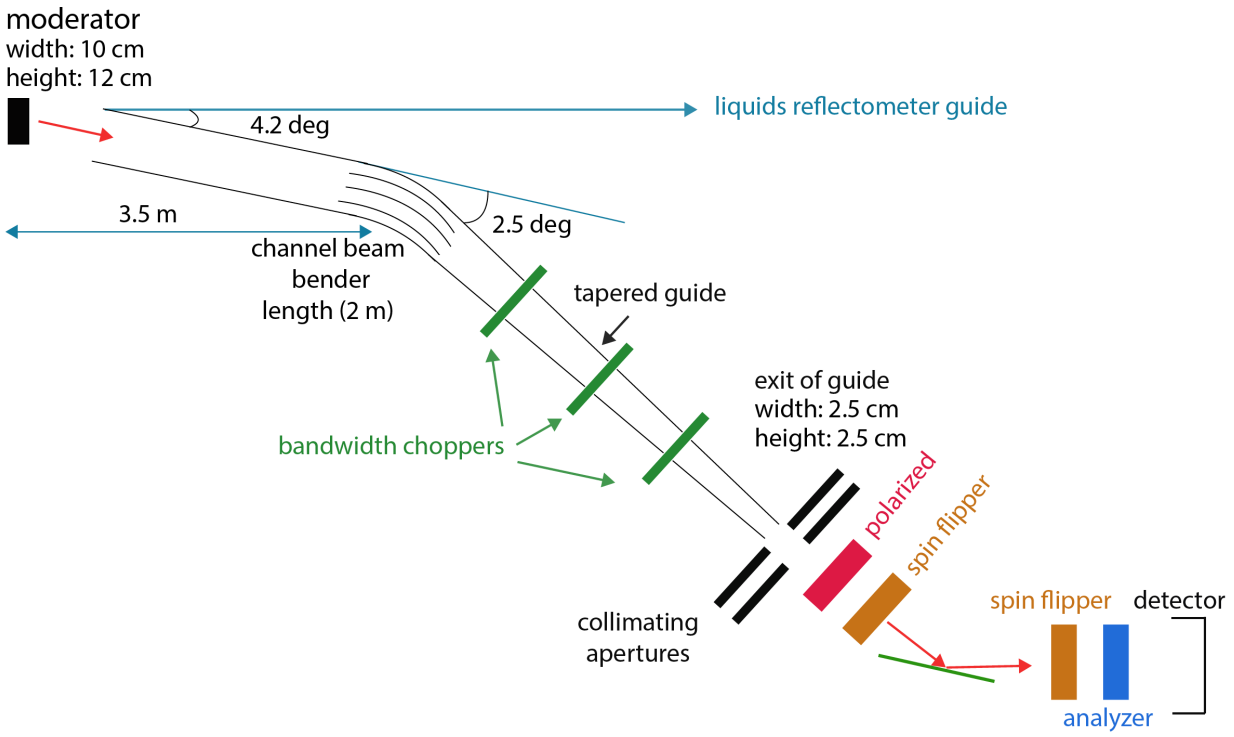


**Figure 3.6.:** Overview of the Magnetism Reflectometer MAGREF at the Spallation Neutron Source (SNS). The figure illustrates the key components and setup of it, including the channel beam bender used for neutron deflection, the tapered neutron guide for focusing the beam, and the bandwidth choppers for selecting specific wavelengths. This figure is drawn based on [108] and information from the SNS website [109].

Unlike monochromatic instruments with a fixed wavelength $\lambda$, measurements on MAGREF are performed at a fixed angle $\theta$. It utilizes the TOF technique as mentioned above, where a pulsed neutron beam with a range of wavelengths is directed at the sample. The velocity of neutrons

is inversely proportional to their wavelength, so that the wavelength is directly related to the time $t$ it takes for a neutron to travel from the pulsed source to the detector over a distance $L$. This relationship is given by:

$$\lambda = \frac{h}{mL} \cdot t \tag{3.3}$$

where $h$ is Planck's constant and $m$ is the neutron mass. Since neutrons of different wavelengths arrive at the detector at different times, recording their arrival times allows us to determine their wavelengths using equation 3.3. Given that $Q$ depends on the wavelength (as shown in equation 3.2), measuring neutrons at various times enables us to sample a broad range of $Q$-values. However, in reflectivity measurements, each wavelength corresponds to a specific $Q$ value. If the $Q$ range covered by varying the wavelength alone is insufficient, it is necessary to use multiple angles of incidence $\theta$ to extend the $Q$-range. Typically, measurements at each angle take approximately 15 min to a few hours depending on several factors such as the desired resolution and the scattering intensity. Adjusting the angle of incidence allows us to capture a broader range of $Q$-values.

The overview of the MAGREF instrument is shown in Fig. 3.6. Neutrons from the moderator are initially deflected by 2.5 degrees using a channel beam bender made of supermirrors, which are specifically designed to reflect neutrons at their critical angle to minimize the loss of intensity. This deflection is crucial to ensure adequate separation from nearby instruments, such as a liquid reflectometer, and to deliver a "clean" neutron beam to the sample, free from fast neutrons and gamma radiation. The beam is then directed through a tapered neutron guide coated with supermirrors. This guide focuses the neutron beam both horizontally and vertically, narrowing it to a size suitable for typical sample areas, which are generally several square centimeters. Bandwidth choppers are employed to select a specific wavelength range (from 1.8 to 14 Å) to prevent frame overlap. Frame overlap occurs when slow neutrons from one pulse mix with faster neutrons from the subsequent pulse, making it difficult for time-of-flight detection to distinguish between them. The choppers, which are rotating disks with neutron-transparent windows, accomplish this task by allowing only neutrons within a specific speed range to pass through. Additionally, the second of the three choppers is specifically designed to absorb very slow neutrons. The instrument also includes collimation slits, a position-sensitive detector, and polarizing and analyzing devices.[108]

MAGREF is equipped with *in-situ* annealing capabilities, with temperatures ranging from 750 K to 5 K. For the annealing experiments conducted in this thesis, the conditions matched those used in ex-situ experiments. The samples were exposed to a vacuum of $1 \times 10^{-6}$ mbar at temperatures of 400 °C or 450 °C. Heating was applied from the backside using a copper heater, similar to our lab heater, but positioned in a vertical orientation. After this treatment, the samples were cooled to 300 K and 120 K for polarized neutron reflectometry (PNR) measurements. The magnetic field is applied parallel to the sample, similar to the orientation used in

MPMS SQUID-magnetometry measurements. The incident neutron beam was polarized with spins either parallel (spin-up) or anti-parallel (spin-down) to the direction of the magnetic field. Reflectivity curves for spin-up (+) and spin-down (-) neutrons were recorded as a function of $Q$. During the experiment, an external magnetic field of 1 T, close to the saturation field, was applied parallel to the film plane to minimize spin-flip scattering. The reflectivity data obtained at 300 K and 120 K were analyzed using the GenX software [110].

## 3.5. X-ray photoelectron spectroscopy

X-ray photoelectron spectroscopy (XPS) is a surface-sensitive technique for the non-destructive analysis of the elemental composition and electronic structure. The process involves irradiating the sample with X-rays, which causes photoelectrons to be emitted from the material's surface, as illustrated in Fig. 3.7. XPS measures the kinetic energy $E_k$ of these emitted photoelectrons using a hemispherical analyzer, which allows for the determination of the concentration of electrons per kinetic energy interval. The kinetic energy is related to the binding energy $E_b$ by the equation:

$$E_b = h\nu - E_k - \phi \tag{3.4}$$

where $h\nu$ is the energy of the incident X-rays, and $\phi$ is the work function of the spectrometer. By analyzing the binding energy $E_b$, XPS provides detailed information about the elements present in the sample, their chemical states, and their concentrations. XPS is typically surface-sensitive, with a probing depths of 1-10 nm. However, this depth can vary depending on the incident photon energy and the detection angle. Techniques like HAXPES, which use higher photon energies, can probe deeper into the sample, allowing for the analysis of thicker films. The resulting spectrum, which plots binding energy against intensity, provides information of the surface chemistry and composition.

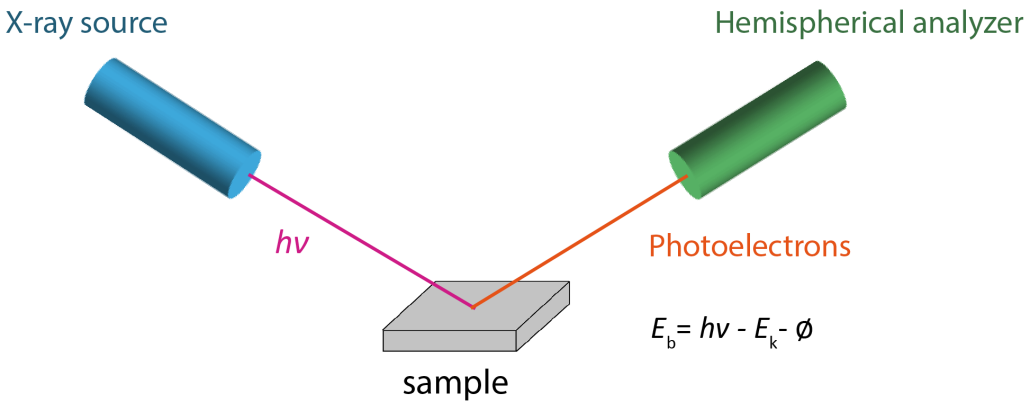


**Figure 3.7.:** Schematic representation of photoelectron emission from a sample surface.

The Hard X-ray Photoelectron Spectroscopy (HAXPES) experiments were carried out at the P22 beamline of PETRA III at DESY, utilizing photon energies ranging from 2.4 keV to 15 keV. The beamline is equipped with a 2-meter-long spectroscopy undulator, delivering a maximum flux of approximately $2 \times 10^{13}$ photons per second at 6 keV. The base pressure was maintained at $1 \times 10^{-9}$ mbar, ensuring optimal conditions for high-resolution measurements. Spectra were acquired using a hemispherical analyzer with an energy resolution of $\Delta E/E = 1.4 \times 10^{-4}$. For the HAXPES experiments presented in this thesis, the photon energy was fixed at 3.4 keV, providing an information depth of 3.7 nm to 4.6 nm. Core-level spectra of Sr 3$d$, La 3$d$, Co 2$p$, and O 1$s$, as well as valence band spectra from the ex-situ annealed samples, were measured

with an incident angle of 60°.

The Ambient-Pressure Soft X-ray Photoelectron Spectroscopy (AP-XPS) experiments were performed at Beamline 9.3.2 of the Advanced Light Source (ALS). This beamline offers photon energies ranging from 200 eV to 900 eV, which provide higher surface sensitivity compared to the HAXPES measurements. Additionally, the setup enables *in-situ* annealing under controlled gas atmospheres, including a $H_2$ environment, and can operate at elevated temperatures of up to 600°C. For this thesis, Sr 3*d*, La 4*d*, Co 3*p*, and O 1*s* core-level spectra were recorded during a thermal reduction treatment ($p(H_2) = 0.1$ mbar, $T = 350$°C, $t = 130$ min), with valence band spectra periodically recorded. The photon energy for these measurements was fixed at $h\nu = 680$ eV, corresponding to an information depth of 0.5 to 1.3 nm.

## 3.6. Magnetic Property Measurement System

A SQUID magnetometer, model Magnetic Property Measurement System (MPMS) from Quantum Design [111] was utilized to measure the macroscopic magnetic properties of the samples. It uses a superconducting magnet capable of generating a vertical magnetic field in the range of −7 T to 7 T. The system operates over a temperature range from 5 K to 380 K, enabled by a liquid helium cooling system that ensures temperature control during measurements. Fig. 3.8 illustrates the core components and working principles of the MPMS system. The sample is mounted in a straw-like holder, allowing it to move vertically through the pick-up coils of a second-order gradiometer. As the sample moves, its magnetic moment induces a current in the coils, which is used to detect tiny changes in the magnetic field.

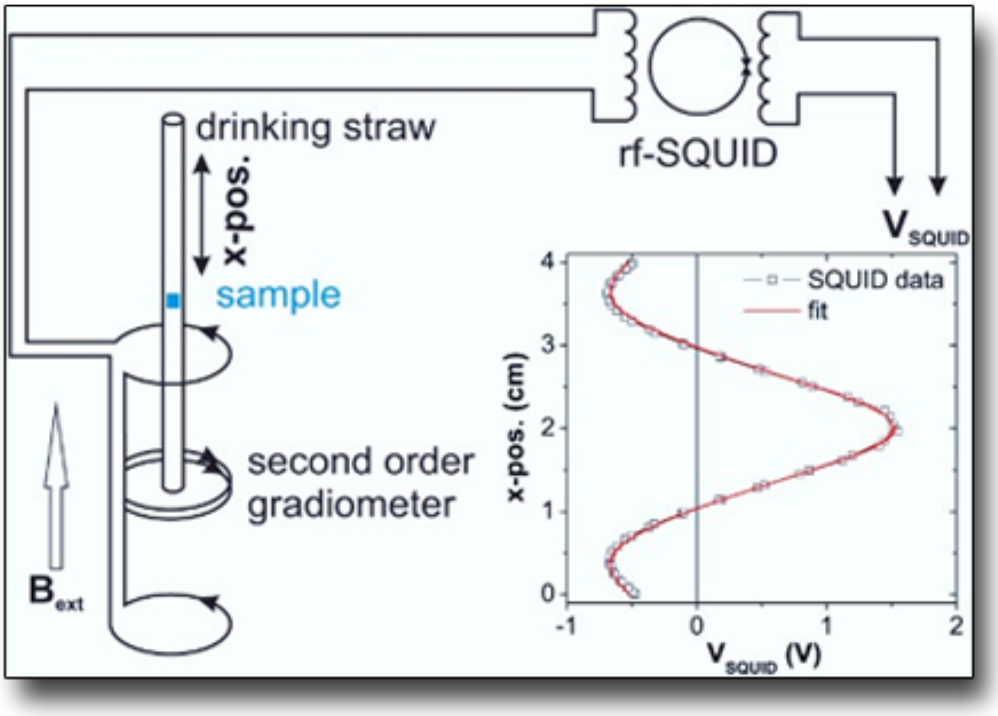


**Figure 3.8.:** Detection system of a Quantum Design MPMS SQUID magnetometer, with the sample mounted in a straw. Adapted from [112].

The pick-up coil is coupled with a radio-frequency Superconducting Quantum Interference Device (rf-SQUID), which is the core element of the system. A SQUID consists of a superconducting loop interrupted by a Josephson junction, integrated with an $LC$ (inductor + capacitor) circuit. The magnetic flux generated by the current from the pick-up coils induces a circulating current in the SQUID ring, allowing for the measurement of magnetic moments with very high sensitivity—down to the order of $10^{-11}\,\mathrm{Am}^2$.

The MPMS operates in two modes: Direct Current (DC) mode and Reciprocating Sample Option (RSO) mode. In DC mode, the sample moves through the pick-up coil in discrete steps, while in RSO mode, the sample oscillates around a set position. The RSO mode generally provides faster measurements with better noise suppression compared to the DC mode, making it particularly advantageous for high-precision magnetic characterization.

In this thesis, the MPMS is used to measure both the field-cooled (FC) curve and the hysteresis curve of LSCO at various temperatures. For the field-cooled measurements, a small magnetic field of 5 mT is applied. During the hysteresis measurements, the magnetic field is swept from -5 T to 5 T. All measurements are performed in the RSO mode. Each data point represents the average of three individual measurements.

## 3.7. Physical Properties Measurement System

The Physical Property Measurement System (PPMS) from Quantum Design was used to investigate the physical properties of the sample. This system is capable of measuring heat capacity, thermal transport, and electrical transport properties over a wide range of magnetic fields, from -9 T to 9 T, and temperatures, from 1.9 K to 400 K. Additionally, magnetization and AC susceptibility can be assessed using a vibrating-sample magnetometer (VSM), which offers a sensitivity of approximately $10^{-9}$ A m$^2$, slightly lower than that of the MPMS system. In this study, only the "Resistivity Option" of the PPMS was utilized.

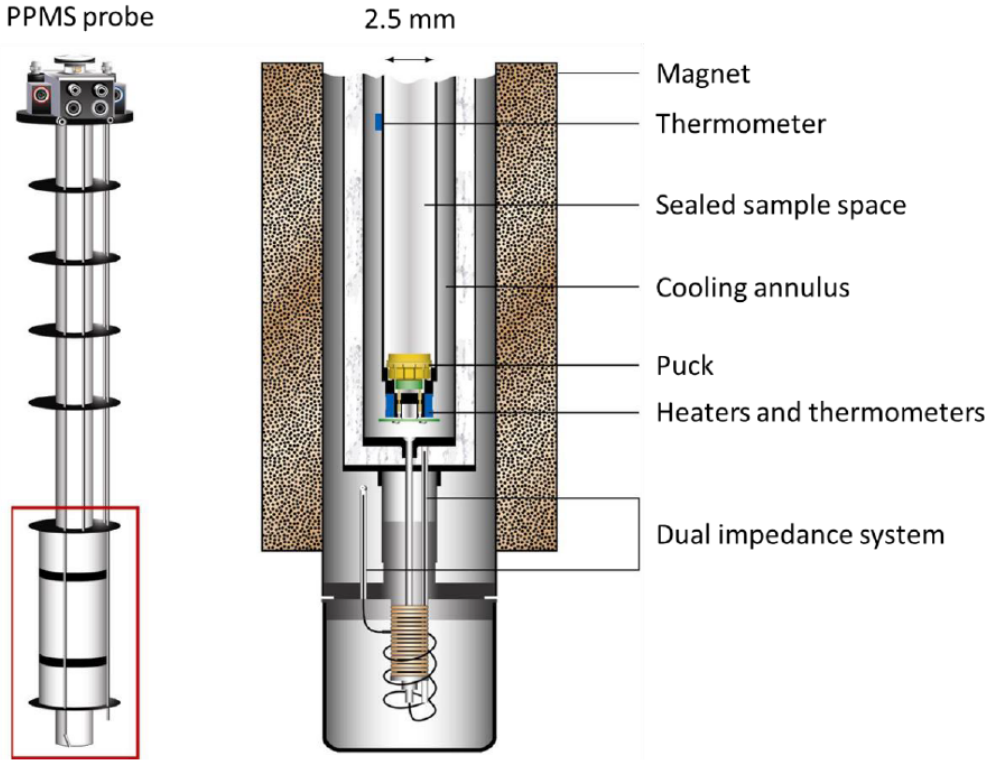


**Figure 3.9.:** The PPMS probe and the cross-section of the probe's sample area. Adapted from [113].

Fig. 3.9 illustrates the PPMS probe and the cross-section of its sample area. The sample chamber features a 12-pin connector at its base, pre-wired to the system's electronics. This connector accommodates a removable sample insert or "puck", which serves as the foundation for all PPMS measurement inserts. For resistivity measurements, the sample puck (see Fig. 3.10) includes four contacts per bridge board channel, providing one positive and one negative contact for current and voltage. The sample is contacted in the van-der-Pauw geometry. By manually rotating the sample to align with vertical and horizontal directions, the corresponding resistances were measured. In each measurement, two consecutive temperature sweeps were conducted with varied electrical contacts to measure the resistances. According to the van-der-Pauw method, the sheet resistance $R_s$ is calculated using the resistances measured in the vertical direction ($R_{\mathrm{AB,CD}}$) and horizontal direction ($R_{\mathrm{BC,DA}}$). However, when $R_{\mathrm{AB,CD}}$ and $R_{\mathrm{BC,DA}}$ are not identical, an asymmetry correction factor $f$ must be applied. This correction factor adjusts for the asymmetry between the two resistances and is close to 1 only when $R_{\mathrm{AB,CD}} \approx R_{\mathrm{BC,DA}}$. In this

case, we did not apply the correction factor, because the measured resistances were sufficiently close in value, and the correction was considered negligible. The sheet resistance is related to these resistances by the corrected equation:

$$R_s = \frac{\pi}{\ln 2} \cdot \frac{R_{\mathrm{AB,CD}} + R_{\mathrm{BC,DA}}}{2} \cdot f \tag{3.5}$$


**Figure 3.10.:** The PPMS sample puck used for resistivity measurements. The puck features four contacts per bridge board channel, allowing for current and voltage measurements in the van-der-Pauw geometry.

In this equation, $R_{\mathrm{AB,CD}}$ is the resistance measured between contacts A and B with current flowing through contacts C and D, while $R_{\mathrm{BC,DA}}$ is the resistance measured between contacts B and C with current flowing through contacts D and A. This formula provides the sheet resistance by averaging these resistances and scaling by the factor $\frac{\pi}{\ln 2}$, which accounts for the geometry of the sample and the configuration of the contacts.

Additionally, samples are attached to the puck using aluminum (Al) wires bonded through a wire-bonding machine at the instiutute PGI-7, Forschungszentrum Jülich. However, directly bonding Al wires to the LSCO film would result in high Schottky-type contact resistance due to the significant difference in the work function between Al and LSCO. To reduce this contact resistance, platinum (Pt) was sputtered onto the four corners of the sample before wire-bonding, as Pt has a work function closer to that of Al. This process lowers the contact resistance and enables the formation of an Ohmic contact, which can ensure more accurate resistance measurements.

## 3.8. Rutherford Backscattering Spectrometry

Rutherford Backscattering Spectrometry (RBS) is used in this thesis to investigate the cation stoichiometry of LSCO. It works by directing a beam of high-energy ions onto a sample and measuring the backscattered ions. Unlike X-ray Photoelectron Spectroscopy (XPS), which typically analyzes a shallower depth, RBS can probe depths of about 2 $\mu$m when using helium ions ($^4He^+$). This capability allows RBS to provide information not only about the elemental composition but also about the depth distribution of different elements within the sample. The accuracy of RBS is generally within a few percent, depending on the scattering atoms involved. It is particularly effective for detecting heavy elements and is less sensitive to lighter elements, such as oxygen.

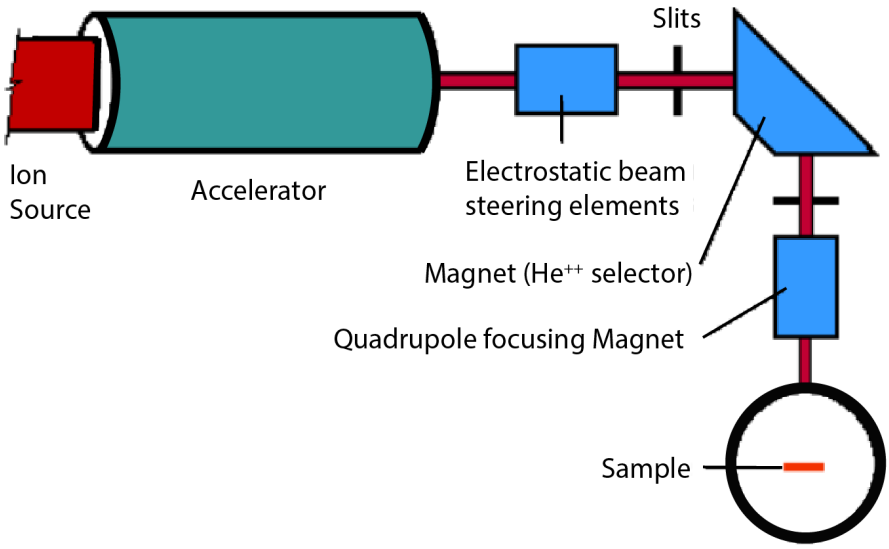


**Figure 3.11.:** Schematic of a Rutherford Backscattering Spectrometry setup used to investigate the cation stoichiometry of LSCO. This figure is adapted from the one provided in [114].

As shown in Fig. 3.11, a typical RBS setup consists of an ion source that generates high-energy ions, such as protons or alpha particles. These ions are then accelerated to the desired energy level by an accelerator. The ion beam is directed towards the sample using electrostatic beam steering elements. As the beam reaches the sample, a quadrupole focusing magnet maintains the beam's focus and reduces divergence. After impacting onto the sample, some ions are backscattered and detected by the detector, which measures their energy and intensity to provide information about the material's composition and structure.

In this thesis, RBS measurements were conducted by Dr. Jürgen Schubert and Dr. Omar Concepción from the PGI-9 institute using a Tandetron accelerator. Helium ions ($^4He^+$) were accelerated to 1.4 MeV and used as probes. As these high-energy helium ions impinge on the sample, a fraction of them are backscattered and detected. By measuring the energy loss of these backscattered ions, the RBS technique can obtain depth profiles of various atomic species extending to several micrometers within the sample. The RBS spectrum typically shows the number of backscattered particles detected as a function of their energy. The data were

subsequently analyzed using the RUMP software package [115, 116].

# 4. Results

## 4.1. Sample preparation

### 4.1.1. Epitaxial thin films

This section will explain the substrate preparation, thin film deposition, and the characterization of the surface morphology of the obtained epitaxial LSCO thin films.

#### 4.1.1.1. Preparation of $SrTiO_3$ substrates

The substrate plays an important role in expitaxial thin film growth since it can largely alter the thin film quality. On the one side, the substrate needs to have a small lattice mismatch compared with the thin film. Normally, a lattice mismatch less than 3% to 4% is considered as an ideal parameter for epitaxial thin film growth.[117] On the other side, the substrate should have a good thermal stability and similar thermal expansion value since thermal instability and a large thermal expansion value can lead to strain-induced structural transformation during high-temperature thin film deposition, such as $BaTiO_3$ substrates for manganese oxide thin films [118].

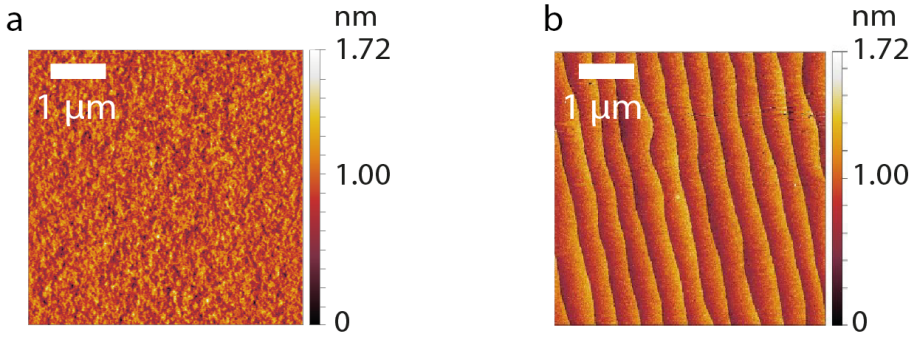


**Figure 4.1.:** a) AFM image of the STO bare substrate. The surface roughness of this substrate is around 176 pm. b) AFM image of a STO bare substrate after BHF termination and high-temperature annealing. The surface roughness of this substrate is around 153 pm.

Strain-induced structural phase transitions can largely alter the physical properties of the thin film. Thus, one usually avoids using such substrate in the systematic study of oxygen-vacancy-induced topotactic phase transitions in LSCO thin films. Furthermore, the substrate's surface

morphology is equally vital in thin film deposition processes, necessitating a smooth and clean surface to ensure uniform and defect-free thin film growth.

Consequently, (001)-$SrTiO_3$ (STO) substrates are chosen for the deposition of LSCO thin films based on the fact that single crystalline STO has a small lattice mismatch (around 1%) with LSCO bulk lattice constant (3.86 Å) and with a thermal expansion coefficient value of 9.4 $\times$ $10^{-6}$/°C [119]. In order to achieve $TiO_2$-terminated surfaces, the substrates are etched by buffered hydrofluoric acid (BHF) and thermally treated at 950 °C for 2 hours [120]. Fig. 4.1 (a) shows the bare STO substrate without any treatment. After etching by BHF and annealing at 950 °C for 2 hours, a well-defined step terrace structure is achieved (see Fig. 4.1 (b)). The step terraces originate from the crystallographic lattice planes and the polished surface, which are typical features of atomically defined surfaces. The width of the terrace may vary from substrate to substrate. However, the respective step terrace height is normally at the order of single unit cells of the perovskite lattice as visible by an AFM line scan across the terrace steps shown in Fig. 4.1.[121]

#### 4.1.1.2. PLD growth of LSCO epitaxial thin films

The epitaxial LSCO thin films were grown by pulsed laser deposition (KrF, $\lambda$=248nm). The growth of LSCO thin films was conducted at 650°C under an oxygen partial pressure of 0.053 mbar, with laser fluence and repetition rate set at 2 J $cm^{-2}$ and 5 Hz, respectively. These growth parameters were optimized based on the findings in Ref. [122] and remained consistent across all samples to ensure reproducibility.

During the growth, RHEED was employed to monitor the film growth and to control the film thickness. Fig. 4.2(a) shows the RHEED intensity evolution during the 20 nm thin film growth. The intensity oscillations in the early stage of film growth indicate the initial layer-by-layer growth mode while the intensity stabilization in the later time indicates a step-flow-like growth mode [123]. One oscillation in Fig. 4.2(a) represents the growth of one monolayer of LSCO and 20 nm (53 monolayers) were grown in total. By calculating the growth rate from the initial RHEED intensity oscillations, the thickness of the thin film was estimated. The surface morphology of the sample before and after film growth is documented by the RHEED pattern and AFM (Fig. 4.2(b) and (c)). The RHEED pattern of both the STO substrate (before the thin film growth) and LSCO thin film shows clear specular spots and a symmetric streaky diffraction pattern, indicating a smooth surface of the sample before and after sample growth. However, the further broadened diffraction spots of the thin film are indicative of a slightly roughened surface compared to the STO substrate. Furthermore, the AFM images in Fig. 4.2(c) indicate that the surface morphology remains smooth before and after the film growth.

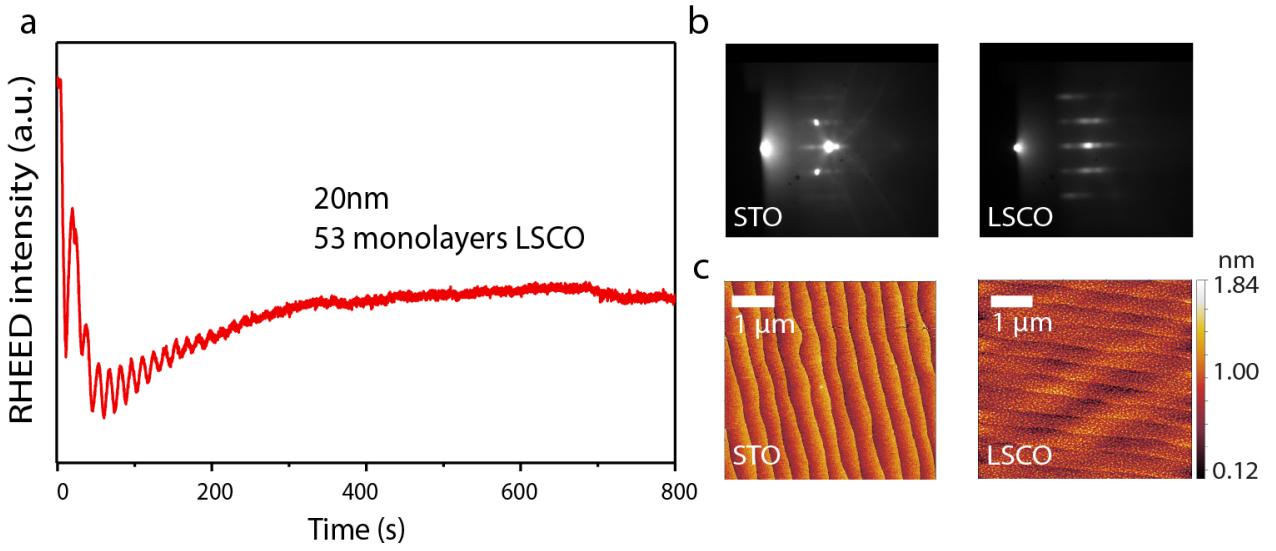


**Figure 4.2.:** LSCO thin film growth characterization. a) 20 nm (53 monolayers) LSCO growth monitored by RHEED. Each oscillation represents the deposition of one monolayer. b) RHEED pattern of the bare STO substrate with the specular spot and corresponding diffraction spots appearing on the Laue circle of a two-dimensional surface; A 53 monolayers LSCO thin film with further broadened spots, indicative of a slightly roughened surface. c) AFM scan of the STO substrate before thin film deposition and the AFM scan of the LSCO thin film after the deposition. The AFM images with different step terrace direction are due to the angle difference of the sample while performing the measurements.

## 4.2. Structural and physical properties of LSCO thin films

This section focuses on elucidating the structural and physical attributes of as-grown LSCO thin films across various thicknesses. The investigation entails a comprehensive characterization of the film's structure through methods such as XRD, AFM, RSM, and HAADF-STEM. Additionally, systematic studies of electronic and magnetic properties will be conducted using the PPMS and the MPMS. This integrated approach aims to establish a connection between the structural properties and the ensuing physical characteristics of the as-grown LSCO thin films.

### 4.2.1. Structural properties

The structural properties of LSCO thin films are characterized by XRD, RSM, AFM and STEM techniques. Here, we investigate the structural properties of LSCO thin films from a thickness of 10 nm to 80 nm to study the changes in structural properties as a function of film thickness. The as-grown sample has a typical PV structure as indicated by the PV peaks denoted as $(002)_{PV}$ peaks in the XRD, see Fig. 4.3, which is consistent with the comparably oxidizing growth conditions. The peaks, together with clear Kiessig fringes demonstrate that the films have a coherent crystal structure with a defined interface and surface morphology. Increasing the thickness of the films does not change the out-of-plane lattice constant of the sample. As can be seen in Fig. 4.3(b), the LSCO thin film peak is located at 48.1°, corresponding to a

lattice constant of 3.77 Å, which is slightly smaller than the bulk LSCO lattice constant (around 3.86 Å). These values align with the tensile strain experienced by LSCO when it is deposited on the larger lattice constant substrate (i.e. STO).

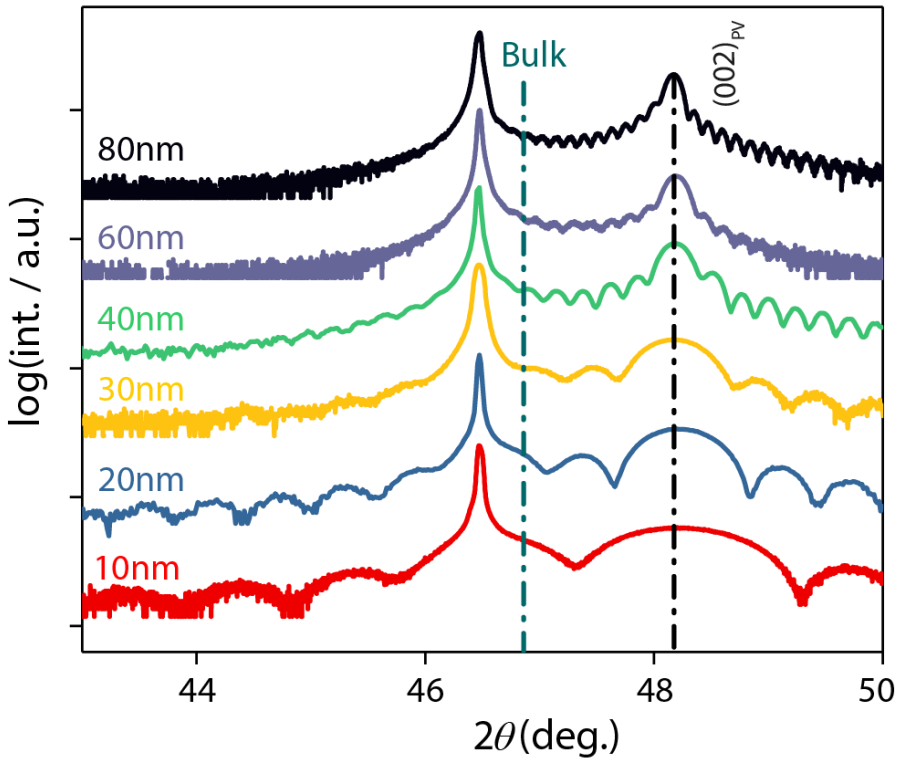


**Figure 4.3.:** XRD of LSCO thin films for thicknesses between 10 nm to 80 nm.

To investigate the in-plane lattice constant of LSCO films with varying thicknesses and to correlate it with in-plane strain, RSM measurements were employed. The RSM in grazing incidence geometry around the asymmetric $(013)_+$ diffraction peak is presented in Fig. 4.4. It reveals a fully strained crystal lattice of the perovskite thin film, based on the in-plane lattice constant of the STO substrate. As observed, the thin film lattice adopts the in-plane lattice constant of the underlying STO substrate. Furthermore, with an increase in the thickness of the thin film, the thin film peak exhibits a slight broadening or smearing. A summary of both in-plane and out-of-plane lattice constant alterations is presented in Fig. 4.5. As shown in Fig. 4.5, the in-plane lattice constant of the LSCO films is very similar to that of the STO substrate, around 3.905 Å. This similarity is a result of the LSCO thin films experiencing tensile strain from the STO substrate as the bulk lattice constant of LSCO (3.86 Å) is smaller than the one of the STO substrate. Therefore, the in-plane lattice constant of LSCO films becomes elongated. Since the in-plane lattice constant becomes larger, the out-of-plane lattice constant is compressed, resulting in a lattice constant from 3.77 Å to 3.78 Å for thickness between 10 nm to 80 nm. By comparing both the in-plane and out-of-plane lattice constant change of the thin films for different thicknesses, we find as lattice mismatch, defined as $L_s = \frac{C_s - C_l}{C_l}$ ; where $L_s$ is the lattice mismatch, $C_s$ is the substrate lattice constant and $C_l$ is the thin film lattice constant, is nearly the same (around 3.3%).

For a more in-depth analysis of the structural characteristics of LSCO films with varying thick-

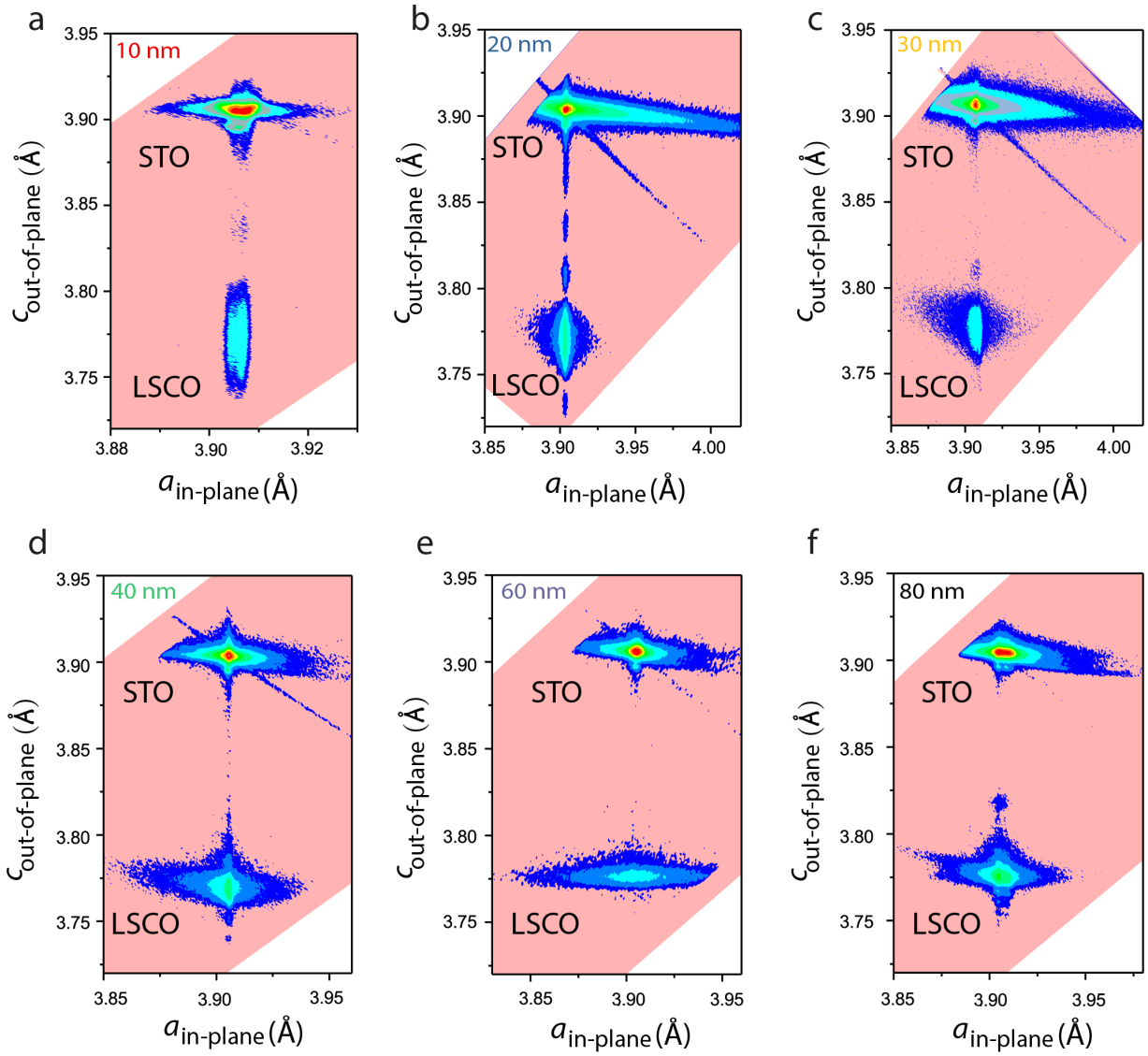


**Figure 4.4.:** Reciprocal Space Mapping around the $(013)_+$ diffraction peak of LSCO thin films, for various thicknesses from 10 nm to 80 nm. The upper 2D peak represents the STO substrate, whereas the lower peak represents the LSCO thin film. It demonstrates that the in-plane lattice constant of samples with different thicknesses is nearly identical to that of the STO substrate. The out-of-plane lattice constant ranges from 3.76 Å to 3.77 Å.

nesses, AFM was utilized to investigate the surface morphology. Fig. 4.6 shows the surface morphology of LSCO thin films with a thickness between 10 nm to 80 nm. For thicknesses below 20 nm, the thin films exhibit smooth surfaces and visible surface terraces, as seen in Fig. 4.6(a) and (b). When the thickness exceeds 20 nm, the films begin to develop additional features on the surface, as seen in Fig. 4.6(c) to (f). These features appear as "lines" in the AFM images, indicating the crack formation as reported in Refs. [124] and [125]. Increasing the thickness of the film widens these features, leading to a rougher surface. The roughness increases from 184 pm (20 nm LSCO film) to 814.8pm (80 nm LSCO film).

To further study this structure, HAADF-STEM was subsequently applied to 20 nm, 40 nm, and 80 nm LSCO films. The results are displayed in Fig. 4.7. From the STEM images, the 20

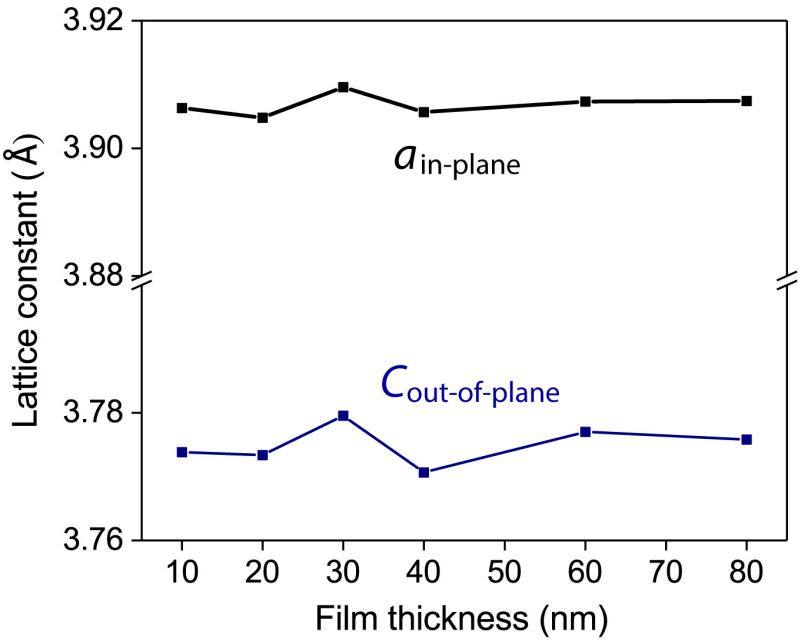


**Figure 4.5.:** The variation in the in-plane and out-of-plane lattice constants of LSCO thin films with a thickness range of 10 nm to 80 nm.

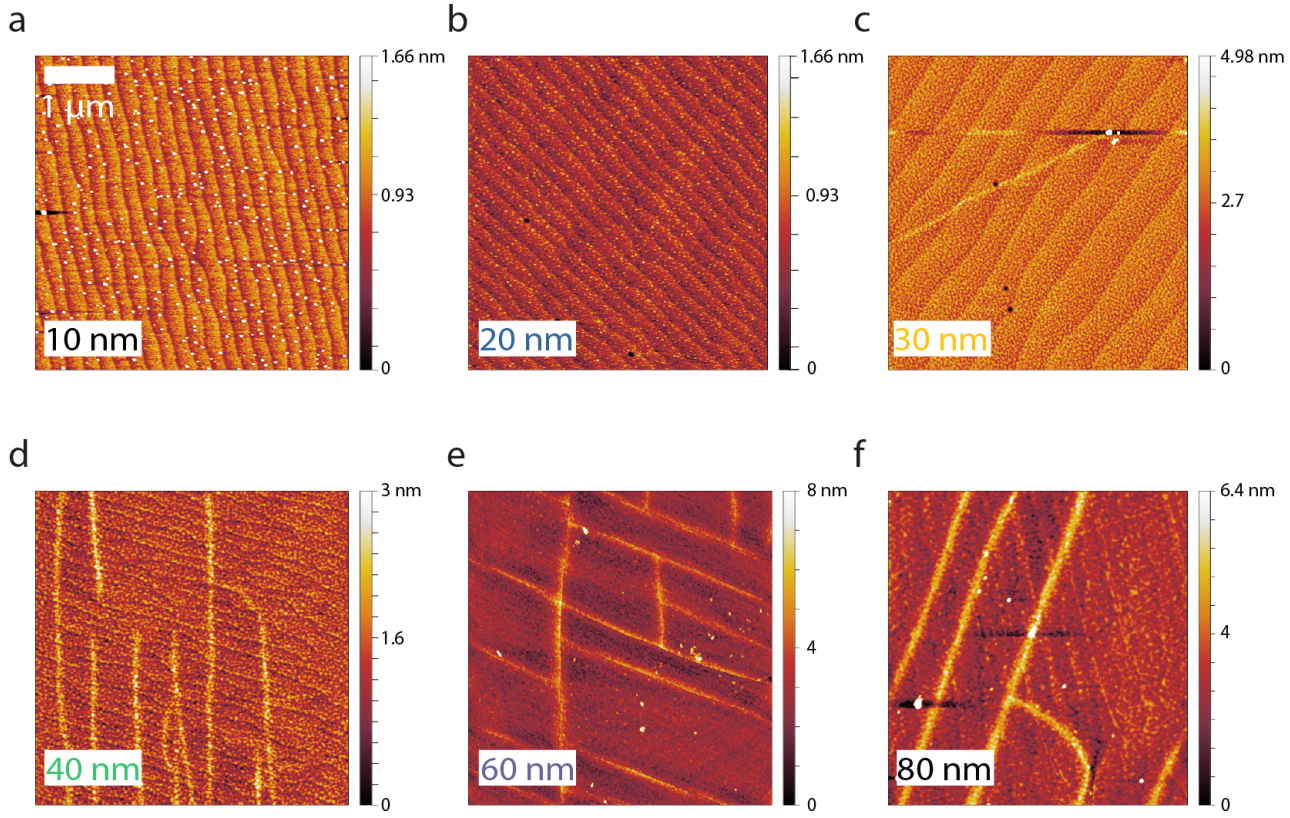


**Figure 4.6.:** AFM images of LSCO thin films with a thickness ranging from 10 to 80 nm. At a thickness below 20 nm, the sample appears to be smooth with clear surface terraces and no additional features on the surface. However, at thicknesses above 20 nm, "line"-like features begin to appear on the surface.

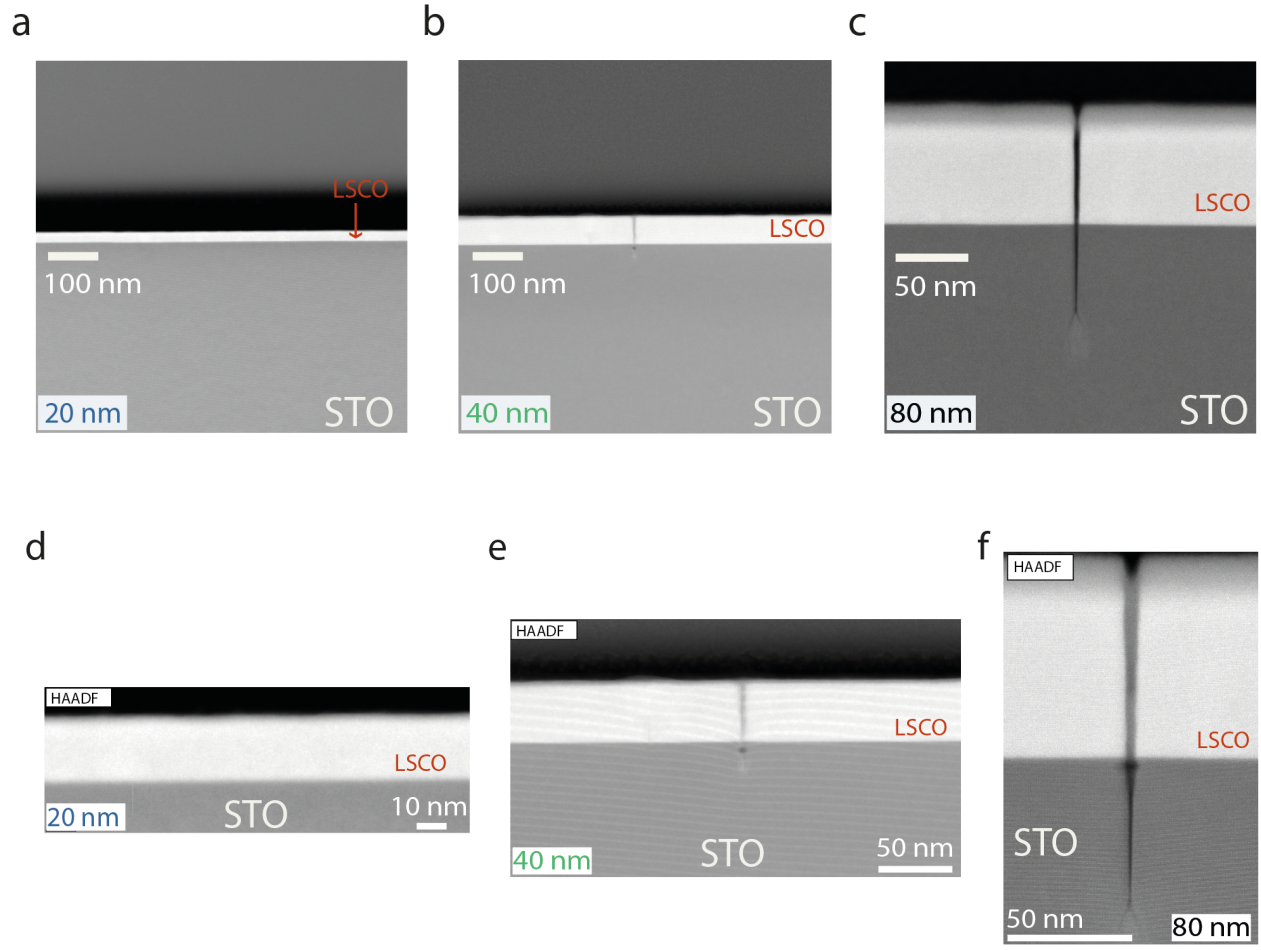


**Figure 4.7.:** HAADF-STEM images (a-f) of LSCO thin films for 20 nm, 40 nm, and 80 nm thickness, respectively. The images reveal that the film begins to crack for thicknesses larger than 20 nm, aligning with the "line"-like features in the AFM images. This experiment was conducted at the Ernst Ruska Center, Forschungszentrum Juelich GmbH, by Dr. András Kovács.

nm film did not form any cracks. As the thickness of the thin film increases to 40 nm, crack formation becomes apparent. When the thickness is increased to 80 nm, the crack becomes even larger, so that the crack even propagates to the substrate. Consequently, it can be inferred that the "line" features observed in Fig 4.6(c) to (f) correspond to the formation of cracks in the thin films.

Such results suggest that there are two possible relaxation processes present in LSCO thin films. At thicknesses below 20 nm, LSCO films grow perfectly epitaxial with smooth surfaces and visible terraced as the film is fully strained. However, above this critical thickness, instead of strain relaxation, vertical cracks are formed as the cracks are more energetically favourable [126]. Consequently, to maintain a smooth surface, the thickness of LSCO thin films should not exceed 20 nm.

### 4.2.2. Electronic properties

The sheet resistance of the LSCO thin film is determined through the conventional van-der-Pauw method. The measurements were conducted by gradually lowering the temperature from 300K to 5K, employing 5×5 $mm^2$ samples to average both horizontal and vertical resistances of the specimen. As illustrated in Fig. 4.8, the room temperature sheet resistance of the 10 nm thin film is 158 Ω while the 20 nm film has a sheet resistance almost half that of the 10 nm film (69 Ω). This aligns with the Ohm law that the sheet resistance is inversely proportional to the film thickness, as the thickness increases from 10 nm to 20 nm. However, this does not apply to the thin films with a thickness larger than 20 nm. The room temperature sheet resistance of 30 nm (232.4 Ω) and 40 nm (689 Ω) films is larger than that of the 20 nm and 10 nm films, while the films become insulating at thicknesses above 40 nm. This is due to the emergence of cracks that appear above a thickness of 20 nm, as discussed in Section 4.2.1. For films with a thickness between 30 nm and 40 nm, the crack density remains low enough to sustain conducting paths within the thin film. However, when the thickness exceeds 40 nm, there is a notable increase in crack density. With the occurrence of these cracks, the LSCO film with thickness above 40 nm transitions to a macroscopic insulating state, as there is no possible conductive path inside the film.

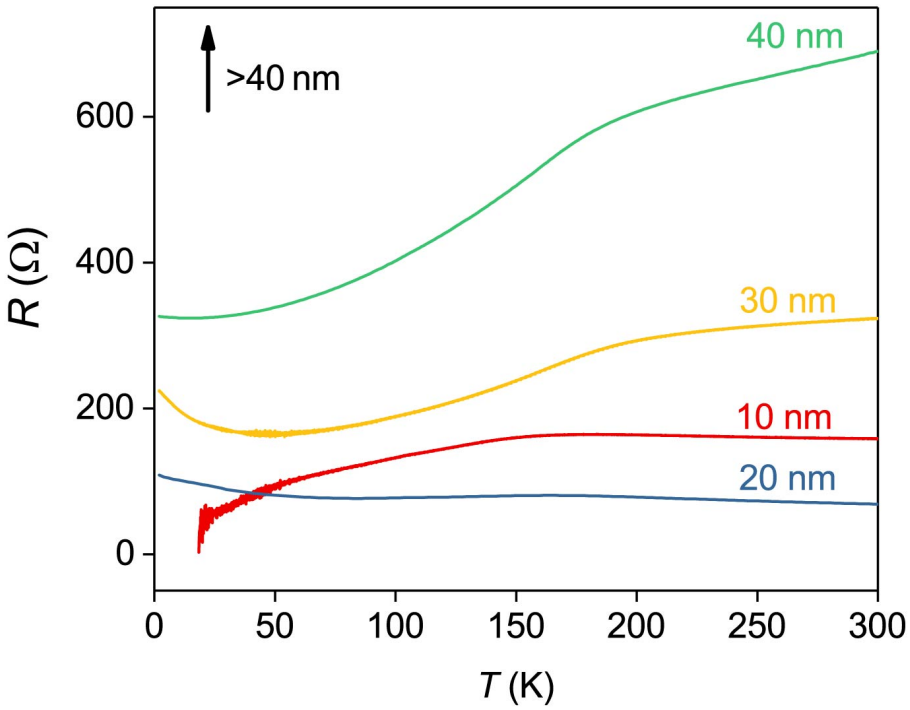


**Figure 4.8.:** Sheet resistance versus temperature curve of LSCO thin films for a thickness of 10 nm (red), 20 nm (blue), 30 nm (yellow), and 40 nm (green). For thicknesses larger than 40 nm, the resistance measurement exceeds the measurable range of the PPMS system, as indicated by a black arrow in the graph.

In summary, the results suggest that crack formation has a significant effect on the resistance of LSCO thin films. When the thickness is less than 20 nm, the sample is conductive on a macroscopic length scale and follows Ohm's law, which states that the sheet resistance is

inversely proportional to the thickness of the film. Nonetheless, when the thickness ranges from 30 nm to 40 nm, cracks begin to form, resulting in higher resistance on the macroscopic length scale compared to those films that are less than 20 nm thick. When the thickness exceeds 40 nm, the thin films become macroscopically insulating because the cracks deepen into the substrate, preventing any conductive path within the films.

### 4.2.3. Magnetic subsystems induced by crack formation

In Fig. 4.9(a), the magnetic characteristics of LSCO thin films exhibit a ferromagnetic behavior within the thickness range of 10 nm to 80 nm, with a corresponding Curie temperature between 160K and 180K. This matches previous reports on the magnetic behavior of LSCO thin films [127]. The Curie temperature is determined from the clear kink of the usual order parameter curve of a ferromagnet as found from FC magnetization as function of temperature in Fig. 4.9 (a). Magnetization curves as function of field at room temperature are depicted in Fig. 4.9 (b). Notably, for thicknesses below 30 nm, the thin films do not exhibit any hysteresis curve, revealing only the diamagnetic background of the STO substrate. However, beyond 30 nm thickness, the samples display ferromagnetism, featuring a modest coercive field below 0.4 T (The coercive field is determined from the hysteresis graph as the magnetic field value where the magnetization crosses zero.) and a saturation magnetization of approximately 0.2 $\mu_{\mathrm{B}}/V_m$. Note that the saturation magnetization per unit volume $\mu_{\mathrm{B}}/V_m$ is determined by dividing the total magnetic moment of the LSCO thin film by the number of unit cells in the film.

At a temperature of 5K, Fig. 4.10 depicts the field-dependent curves. As the thickness increases, multiple inflection points are observed in the hysteresis curve. Each inflection point represents one part of the system realigning in the same direction, constituting a distinct magnetic subsystem associated with a specific Curie temperature. Below 20 nm thickness, the films manifest a single magnetic system with a saturation magnetization of 1.5 $\mu_{\mathrm{B}}/V_m$ and a coercive field at 1.8 T (20 nm) and 1.85 T (10 nm), identified as System 1 in Fig. 4.10. Conversely, for thicknesses above 20 nm, multiple magnetic systems emerge. The thickness above 20 nm in Fig. 4.10 reveals the presence of more than one inflection point, indicating the existence of more than one magnetic subsystem beyond 20 nm thickness. At 30 nm thickness, two distinct subsystems are observable, denoted as Systems 1 and 2 in Fig. 4.10. Moreover, for thicknesses exceeding 30 nm, three subsystems (Systems 1, 2, and 3) are shown. In this context, we identify each magnetic subsystem by examining its coercive field.

To further analyze the magnetic subsystems quantitatively, we applied a first derivative to the field-dependent curves depicted in Fig. 4.10 to pinpoint the corresponding coercive field of each magnetic subsystem. For example, Fig. 4.11(a) presents the first derivative of the field-dependent curve for the 40 nm LSCO thin film, revealing three discernible peaks that correspond to the coercive fields of the three distinct magnetic subsystems. Using the same way, we extract the coercive field data across the thickness range from 10 nm to 80 nm, as illustrated in Fig. 4.11(b).

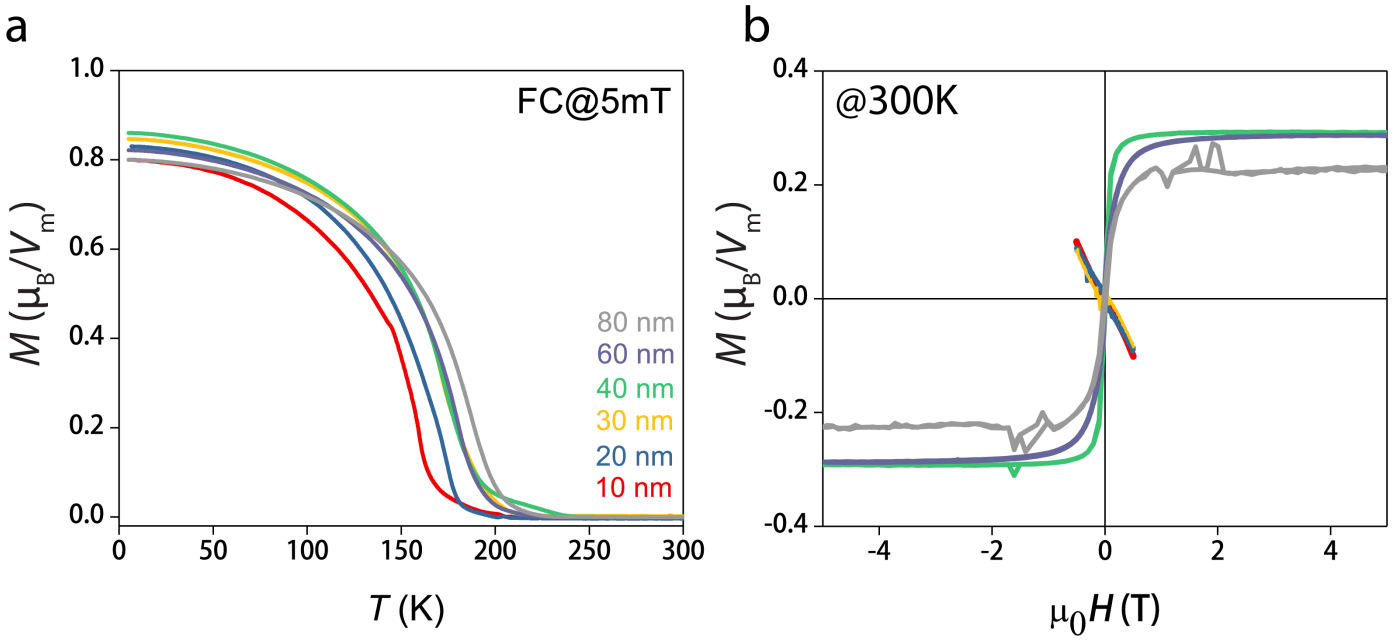


**Figure 4.9.:** (a) Field-cooled magnetization curves of LSCO thin films with thicknesses ranging from 10 nm to 80 nm. Notably, the magnetization remains non-zero at room temperature. (b) Room-temperature field-dependent magnetization (hysteresis) curves for the same thickness range. For the 10 nm to 30 nm films, only a small negative slope is observed, which is attributed to the diamagnetic signal from the STO substrate. No ferromagnetic signal is detected in these films, as confirmed by the absence of hysteresis.

As shown in Fig. 4.11(b), magnetic system 1 manifests consistently across all thicknesses of the LSCO thin film, exhibiting a coercive field ranging from approximately 1.4 T to 1.85 T. This system emerges as the primary magnetic feature within the LSCO thin film. The Curie temperature of this primary system, as indicated by the field-cooled curve in Fig. 4.9(a), is estimated to fall within the range of 160 K to 180 K. As for magnetic subsystem 2, it appears at thicknesses above 20 nm, characterized by a coercive field falling within the range of 0.5 T to 1.1 T. Regarding subsystem 3, it displays a notably small coercive field, measuring below 0.4 T, and appears at thicknesses above 30 nm. These features align with the room temperature ferromagnetism observed in Fig. 4.9(b), where a small coercive field is evident only beyond 30 nm thickness, featuring a Curie temperature exceeding 300K and a coercive field below 0.4 T. This correlation underscores the unique magnetic behavior of subsystem 3, specifically tied to the existed room temperature ferromagnetic properties delineated in Fig. 4.9(b).

Furthermore, to delve deeper into the study of the Curie temperature of the three magnetic subsystems, a temperature-dependent hysteresis curve was applied to the 80 nm LSCO thin film, as depicted in Fig. 4.12(a). The relationship between the saturation magnetization and temperature is elucidated in Fig. 4.12(b). In Fig. 4.12(b), three distinct slopes are discernible in the saturation magnetization versus temperature curve, aligning with the characteristics of the three different magnetic subsystems. Notably, the high-temperature region, at a temper-

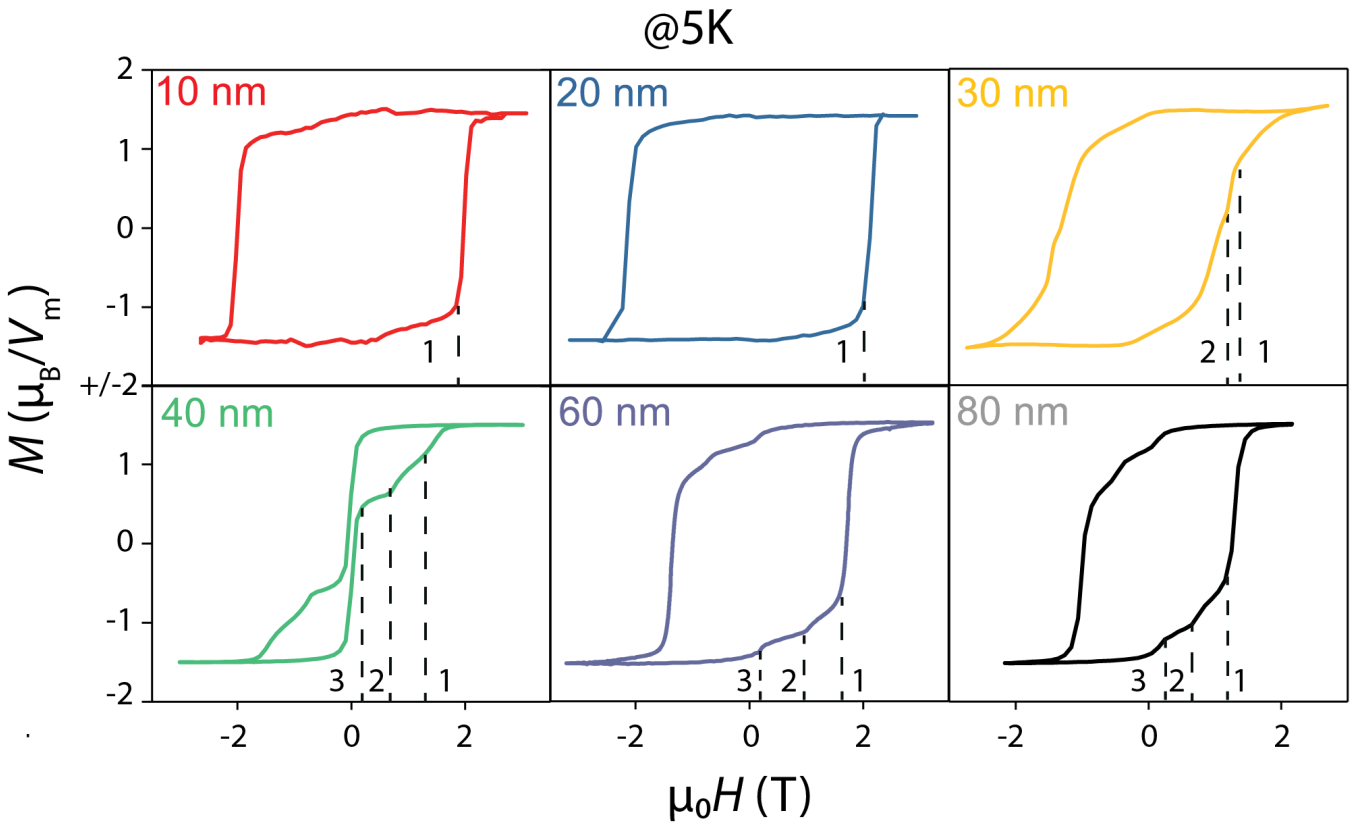


**Figure 4.10.:** Field-dependent hysteresis curves of LSCO thin films at 5K reveals a distinct magnetic behavior. Below a thickness of 20 nm, a singular magnetic system is observed. Conversely, for thicknesses exceeding 20 nm, the emergence of magnetic subsystems 2 and 3 is apparent.

ature between 225 K to 300 K, exhibiting room temperature ferromagnetism, corresponds to subsystem 3, as discussed earlier. The middle region, at a temperature between 125K to 225 K, represents the primary system of the LSCO thin film, characterized by a Curie temperature at approximately 170 K (determined by the FC curve in Fig.4.9(a)), corresponding to magnetic subsystem 1. Consequently, the low-temperature region, at a temperature between 5K to 125K, corresponds to magnetic subsystem 2, featuring a Curie temperature of below 125K. In summary, the Curie temperatures of magnetic subsystems 1, 2, and 3 are determined to be 170K, below 125K, and exceeding 300K, respectively.

Moreover, the noteworthy phenomenon is that the magnetic subsystem becomes evident at thicknesses above 20 nm, a critical threshold associated with crack formation. As the thickness above 30 nm, coinciding with an increased presence of cracks in the sample, a room-temperature magnetic subsystem emerges. This correlation suggests a connection between the appearance of magnetic subsystems and the occurrence of structural cracks in the material. One possible scenario revolves around the nature of Cobalt (Co)-type oxides, which is prone to inducing spin-state transitions through strain change induced by lattice distortion [128] [129]. As Co has various spin types ($Co^{2+}$, $Co^{3+}$, and $Co^{4+}$ in high spin, intermediate spin, and low spin), spin transitions may occur in the cracks as the strain field change within the cracks, leading to the formation of new magnetic domains within these structural imperfections. Consistently,

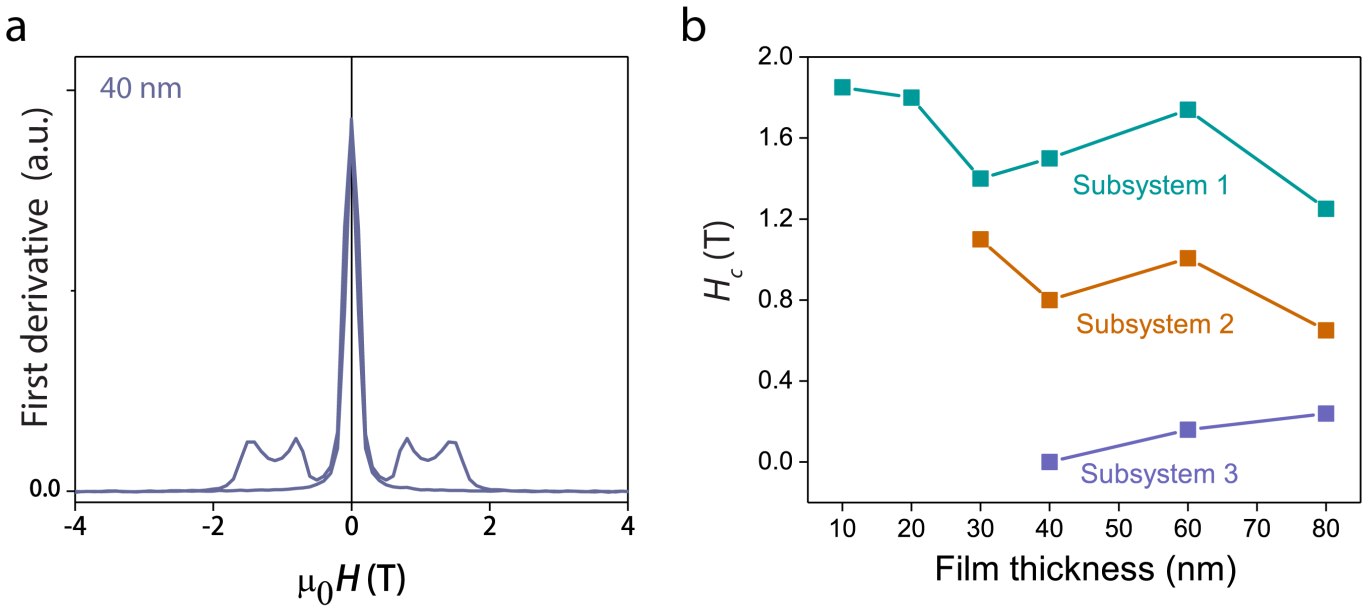


**Figure 4.11.:** a) The first derivative of the hysteresis curve for the 40 nm LSCO thin film reveals three distinct peaks, each corresponding to different magnetic subsystems. b) A comprehensive summary outlining the relationship between the three magnetic subsystems, the thickness of the LSCO thin films, and their respective coercive fields.

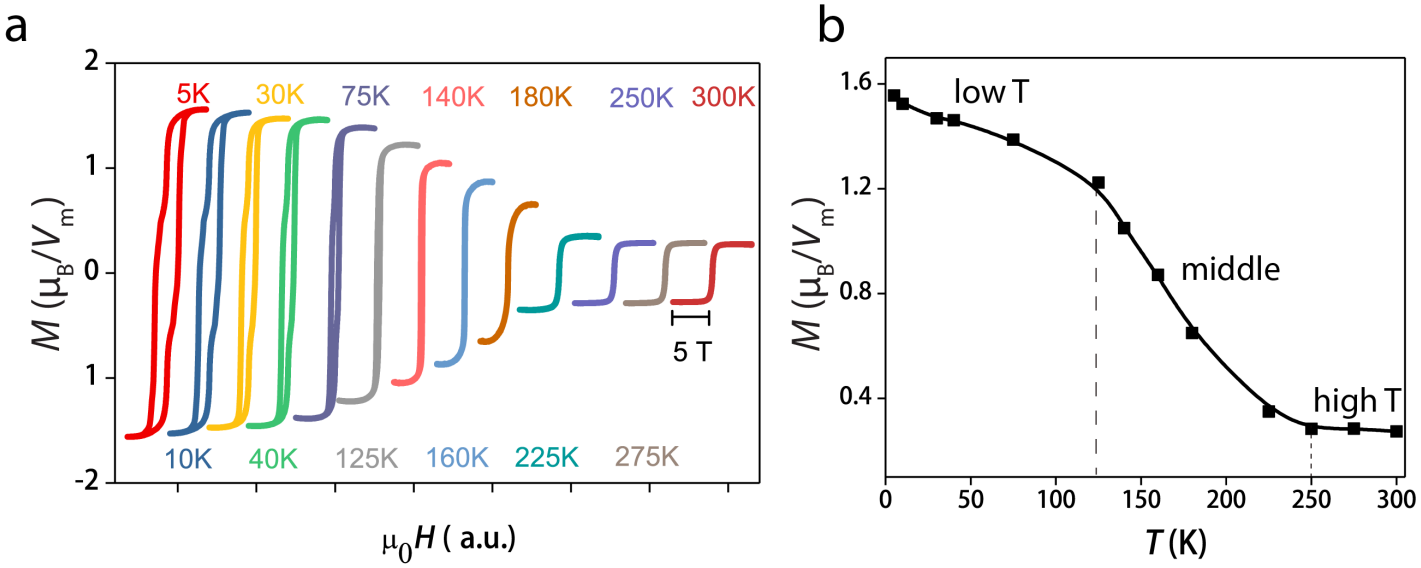


**Figure 4.12.:** a) Hysteresis curves of the 80 nm LSCO thin film, were recorded over a temperature range from 5K to 300K. b) Saturation magnetization of the LSCO thin film at temperatures ranging from 5K to 300K, revealing the presence of three distinct ferromagnetic subsystems characterized by different Curie temperatures.

the magnetic subsystem becomes apparent as the film thickness reaches the critical threshold for crack formation (above 20 nm). To maintain a pure magnetic system of the LSCO thin film, it is advisable to restrict the thickness of the film to below 20 nm for studies involving

field-dependent curves. This aims to mitigate the potential influence of structural cracks on the emergence and characteristics of magnetic subsystems, ensuring a more accurate examination of the film's magnetic behavior.

## 4.3. Control of topotactic phase transition in LSCO films

Having characterized the structural properties of the as-grown LSCO thin film, we now shift our focus to a detailed examination of the phase transition process. By exposing the as-grown layers to a reducing atmosphere, we can induce the removal of oxygen from the lattice, facilitating the formation of the BM phase. This phase transition is achieved through vacuum treatment or exposure to $Ar/H_2$ gas mixtures at slightly elevated temperatures.

The as-grown LSCO thin film exhibits a characteristic perovskite structure, identified by the presence of $(001)_{PV}$ and $(002)_{PV}$ peaks in the XRD diffractogram, as shown in Fig. 4.13 (a). This structural configuration involves the repetition of an octahedral structure, as depicted in Fig. 4.13 (b). However, subsequent treatment of the LSCO thin film at 450 ℃ and $10^{-6}$ mbar for 2 hours induces a structural transformation. In Fig. 4.13 (a), the altered structure is evident in the green curve, revealing additional peaks labelled as $(002)_{BM}$, $(004)_{BM}$, $(006)_{BM}$, and $(008)_{BM}$. These peaks indicate the emergence of a new structure in the sample following the 2-hour annealing at 450 ℃. This newly formed structure is identified as the brownmillerite (BM) phase, characterized by the alternation of octahedral and tetrahedral Co coordination, as illustrated in Fig. 4.13 (c). The identification of the BM phase is confirmed by the presence of these additional peaks, which result from the doubling of the unit cell due to the alternating octahedral and tetrahedral arrangements. These coherent peaks, such as $(002)_{BM}$, $(004)_{BM}$, and others observed, arise because of the regular and repeating arrangement of tetrahedral and octahedral sites along (001) crystallographic directions. This distinctive structural arrangement leads to the specific diffraction pattern observed, which matches the known signature of the BM structure.

To investigate the electronic and magnetic properties of the PV and BM phases, we conducted measurements focusing on magnetization and electric transport behaviors using PPMS and MPMS. As illustrated in Fig. 4.14, the as-grown LSCO thin film exhibits typical metallic and ferromagnetic characteristics due to the double exchange interaction between high spin $Co^{3+}$ and high spin $Co^{4+}$ [131, 132]. The field-dependence of magnetization is shown in Fig. 4.14 (b), while the determined magnetic moment per Co ion versus temperature is shown in Fig. 4.14 (c). It documents the ferromagnetism of the as-grown thin film with a $T_c$ around 180 K and with a saturation magnetization around 1.5 $\mu_B$/ Co at 5 K, consistent with Ref. [133]. However, the magnetization is immediately reduced to nearly zero after 2 h annealing at 450 °C. This is confirmed by both the temperature-dependent and the field-dependent measurements of the magnetization. This observed behavior aligns with previous findings concerning the magnetic properties of the pure BM phase in LSCO and comparable cobaltites [134]. Thus, the structural transformation from pure PV to pure BM phase appears to be associated with the transition from metal to insulator (MIT) and from ferromagnetic to non-ferromagnetic states (ferro-to-non-ferro). Hence, we can generally control the two phases corresponding to the final states on both sides of the structural transition. This forms the basic starting point for more detail in subsequent investigations.

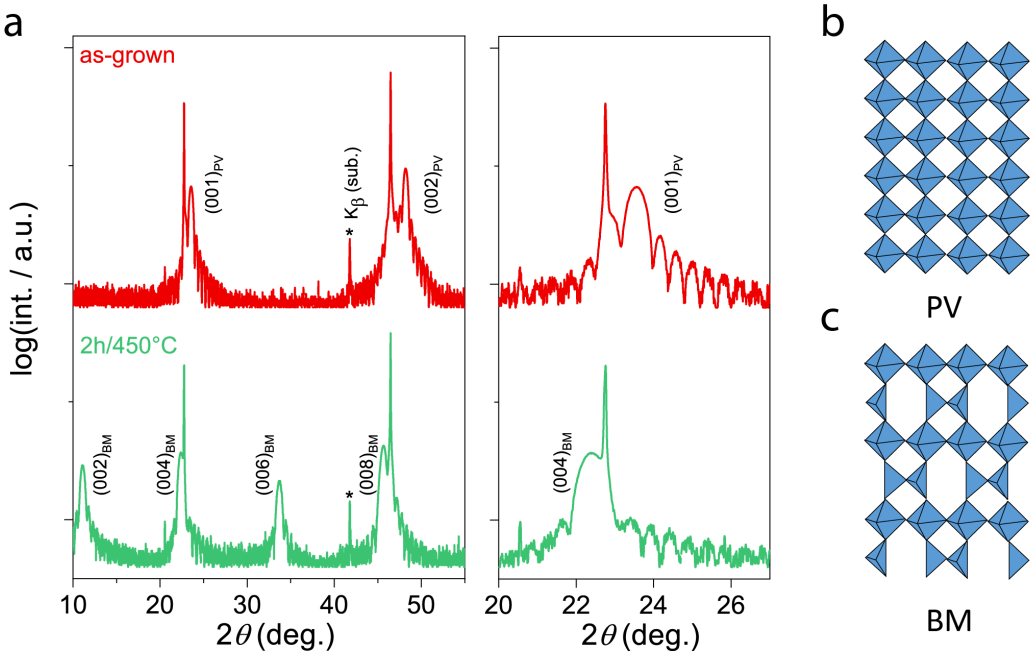


**Figure 4.13.:** a) XRD diffractogram of the as-grown and after 2 h/450 °C annealing (BM phase) LSCO thin film. The appearance of the additional peaks in the 2 h/450 °C LSCO thin film indicates the formation of the BM structure. b) Theoretical structure of the perovskite (repetition of the octahedral structure) and brownmillerite (alternation of the octahedral and tetrahedral structure) LSCO thin film[130].

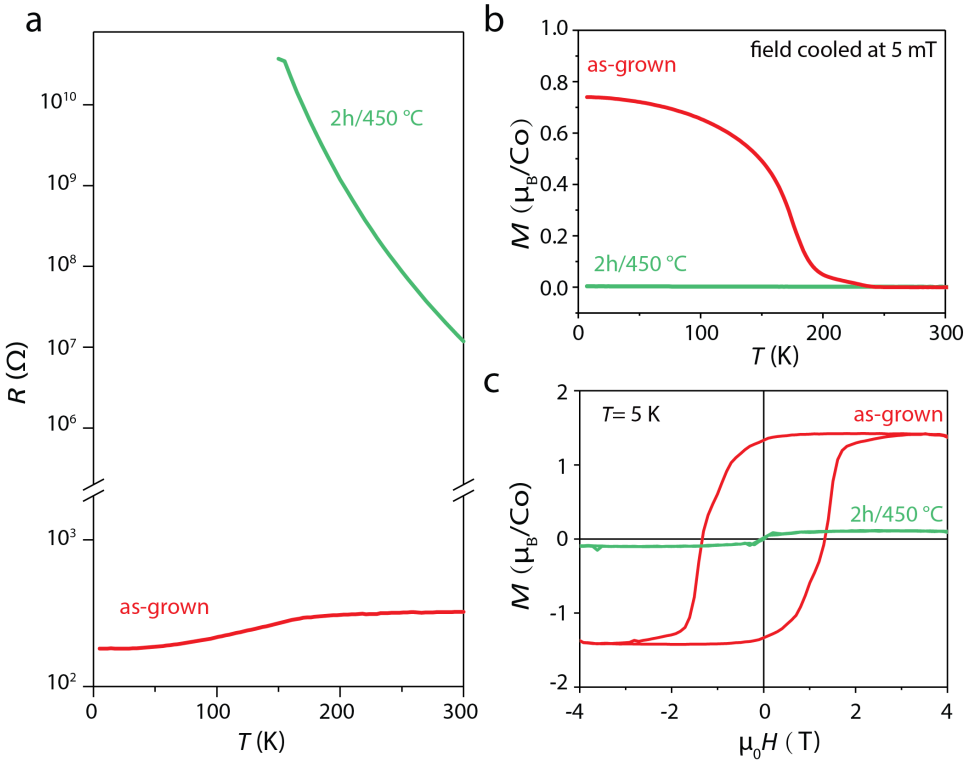


**Figure 4.14.:** Magnetic and transport properties of the as-grown samples and after 2 h annealing at 450 °C. a) Sheet resistance of the as-grown and 2 h/450 °C annealed LSCO sample (note that resistance above $10^{10}$ Ω is outside the measurable range of the PPMS). b) Temperature dependence of magnetization $M$ (T) curves under field cooling, measured by applying an in-plane magnetic field $\mu_0 H = 5$ mT. c) Magnetic hysteresis loops measured at 5 K for LSCO films.

## 4.4. Inverstigation of quenched intermediate states

It has been illustrated in Section 4.3 that the PV phase typically reflects a metallic and ferro-magnetic state [135], while the BM phase is usually characterized by insulating and non-ferromagnetic (often anti-ferromagnetic) behavior [136]. However, the question remains whether the observed phase transitions from metal to insulator and from FM-to-non-FM coincide directly with the structural transition. To answer this question, we study the evolution of the physical properties of LSCO epitaxial thin films upon exposure to reducing environments. The content of this chapter is based on my first-author publication [137]). My main contributions include sample preparation, measurements, data analysis, and manuscript writing.

### 4.4.1. Structural analysis

To investigate the intermediate states, we utilized 20 nm thick epitaxial LSCO [68, 138, 139] thin films. These films were subjected to varying annealing temperatures and durations under vacuum conditions to achieve different intermediate states. Fig. 4.15 (a) and (b) show XRD data of the as-grown sample in comparison to the sample after vacuum-annealing (at $1{\times}10^{-6}$ mbar) for 1 h at 400°C, 2 h at 400°C, 4 h at 400°C, and 2 h of annealing at an increased temperature of 450°C. The as-grown sample has a typical PV structure as indicated by the PV peaks denoted as $(001)_{\mathrm{PV}}$ and $(002)_{\mathrm{PV}}$. The peaks together with clear Kiessig fringes (apparent in the enlarged view in Fig. 4.15 (b)) demonstrate that the films possess a coherent crystal structure with the defined interface and surface morphology. After vacuum-annealing the sample at 400°C for one hour and two hours, the $(001)_{\mathrm{PV}}$ and $(002)_{\mathrm{PV}}$ peaks of the as-grown film shift towards a lower angle, indicating an increase in the PV out-of-plane lattice constant, which is due to lattice expansion. With further annealing of the sample for two more hours at 400°C, the lattice further expands, indicated by the continuous shift of the film peak towards the substrate peaks. Meanwhile, additional peaks denoted as $(002)_{\mathrm{BM}}$, $(004)_{\mathrm{BM}}$, $(006)_{\mathrm{BM}}$ and $(008)_{\mathrm{BM}}$ appear, indicating the initial formation of the BM long range ordered structure of LSCO [133, 140].

As evident from Fig. 4.15 (b), the main PV shoulder (black arrow) resides at larger angles compared to the substrate, which appears at 1 h at 400°C, 2 h at 400°C, and 4 h at 400°C data. At the same time, the rising intensity at the lower angle side of the (001) substrate peak (purple arrow in Fig. 4.15 (b)) coincides with the $(004)_{\mathrm{BM}}$ peak of the BM phase, matching the lattice constant of the $(002)_{\mathrm{BM}}$ peak observed at $2\theta$=11.1°, which firstly appear at 4 h at 400°C data. This, combined with the PV phase (depicted by the black arrow), suggests the coexistence of both the PV and BM phases on intermediate time scales (4 h at 400°C) during the phase transition. Finally, the pure BM phase is achieved by annealing the sample for two hours at 450°C, now showing merely BM peaks, while the remaining PV shoulder disappeared.

The detailed image in Fig. 4.15 (b) reveals distinct Kiessig fringes observed consistently across all intermediate states and the final BM phase, indicating that the sample morphology re-

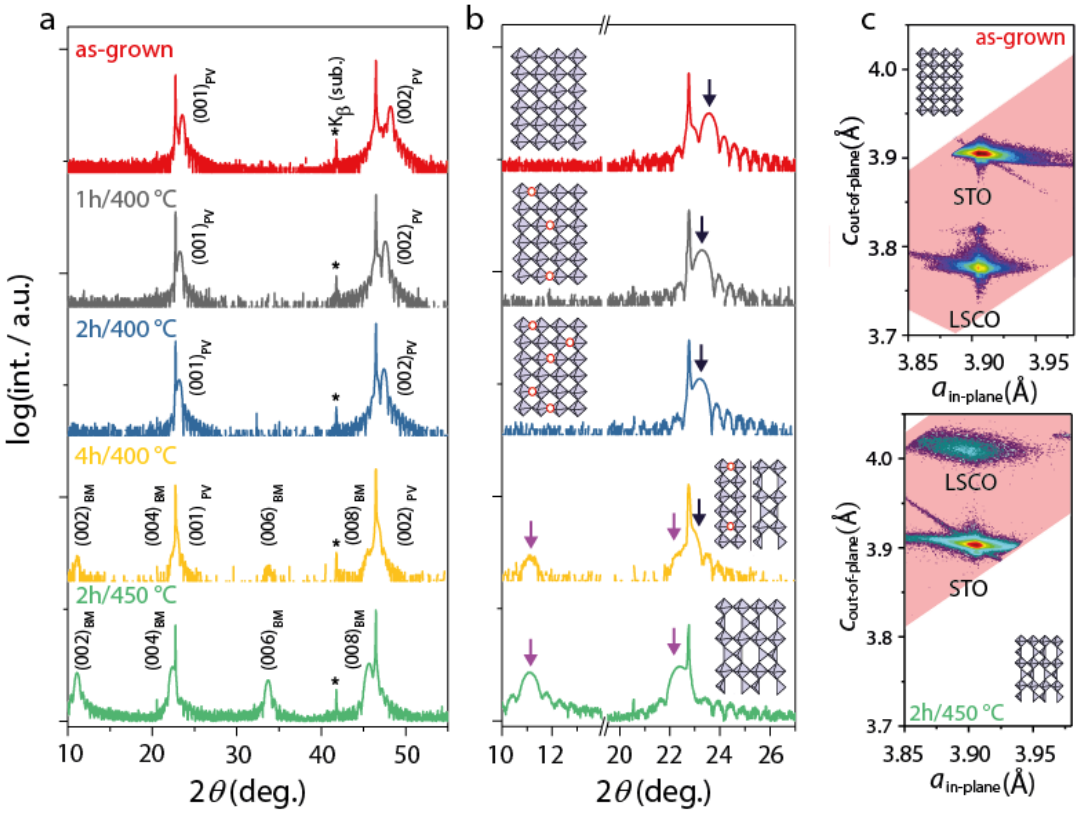


**Figure 4.15.:** Structural evolution of LSCO thin films during the topotactic phase transition from PV to BM. a) XRD diffractograms of as-grown PV structure LSCO thin film (red); LSCO thin film after 1 h of annealing at 400°C (grey); 2 h of annealing at 400°C (blue); LSCO thin film after 4 h annealing at 400°C (yellow); LSCO thin film after 2 h annealing at 450°C (green). b) Enlarged view on $2\theta$ of 10-27°of the corresponding XRD diffractograms from Fig. 4.15 (a). c) The RSM of the as-grown and after 2 h annealing at 450°C LSCO thin films. [137]

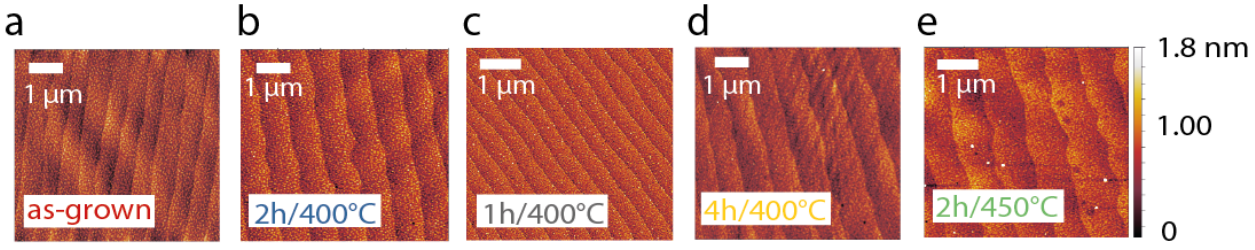


**Figure 4.16.:** Surface morphology of LSCO in four different states monitored by atomic force microscopy (AFM)

mained unchanged during the phase transition. This suggests structural stability throughout the transformation process. Furthermore, the reciprocal space map (RSM) data presented in Fig. 4.15 (c) highlights the in-plane lattice parameters of both the as-grown and fully reduced films. The maintained in-plane lattice parameters during the phase transition indicate that the in-plane strain is preserved, underscoring the stability of the crystalline structure throughout the transformation process. The evolution of the surface morphology, depicted in Fig. 4.16, shows that the surface maintains a clear step-terrace structure similar to that of the as-grown

thin film, even in the presence of a mixed PV and BM phase in intermediate reduction states. This observation suggests that the perovskite to brownmillerite (PV-BM) phase transition occurs locally without significant disruption to the surface morphology. This may indicate that the coexisting PV and BM phases overcome their lattice mismatch through local strain and structural distortion at the phase boundary, rather than surface relaxation, which prevents an increase in surface roughness or even cracking during the transition. This is in accordance with the damped thickness oscillations observed in the XRD experiments of the intermediate states (Fig. 4.15 (b)), indicating the presence of a larger level of structural disorder within the lattice of the mixed phase.

### 4.4.2. Magnetic properties and charge-transport

In order to correlate the structural properties of the annealed LSCO thin films with the magnetic and electronic properties, SQUID magnetometry and electronic charge transport experiments were performed. Fig. 4.17 (a) plots the electrical resistance of LSCO for the different states of the topotactic phase transition. The sheet resistance decreases upon cooling down for the as-grown film, indicating a metallic behavior of the initial film as expected. However, the sample that was annealed for 1 h at 400°C already shows insulating behavior, reflected by an increasing resistance during cooling. At temperatures below 100 K, the resistance is above the measurable range of the PPMS. This observation indicates that an electronic MIT already occurred in the initial phase of the reduction process. After annealing for 1 h at 400°C, 2 h at 400°C, 4 h at 400°C and 2 h at 450°C, the LSCO thin films show the same insulating behavior as the reduced PV thin film, evidencing the occurrence of the electronic phase transition upon the early reduction process.

The magnetic properties for the different states of LSCO films during the topotactic phase transition are shown in Fig. 4.17 (b) and (c). The determined magnetic moment per Co ion versus temperature is shown in Fig. 4.17 (b), while the field-dependence of magnetization is shown in Fig. 4.17 (c). It shows the ferromagnetism of the as-grown LSCO thin film with a $T_c$ around 180 K and with a saturation magnetization around 1.5 $\mu_B$/Co at 5 K, as in Section 4.3. However, the magnetization is immediately reduced to nearly zero after 1 h annealing at 400°C. This is confirmed by both the temperature-dependent and the field-dependent measurements of the magnetization. This suggests that a magnetic transition from robust ferromagnetic behavior to non-ferromagnetic behavior occurs already after 1-2 h of annealing at 400°C, which refers to the reduced PV phase. After annealing for 2 h at 400°C, 4 h at 400°C, and 2 h at 450°C, the magnetization of the LSCO thin film further reduces and almost vanishes. This behavior is consistent with previous results obtained for the magnetic properties of the final BM phase of LSCO and comparable cobaltites [134] and the results discussed in Section 4.3.

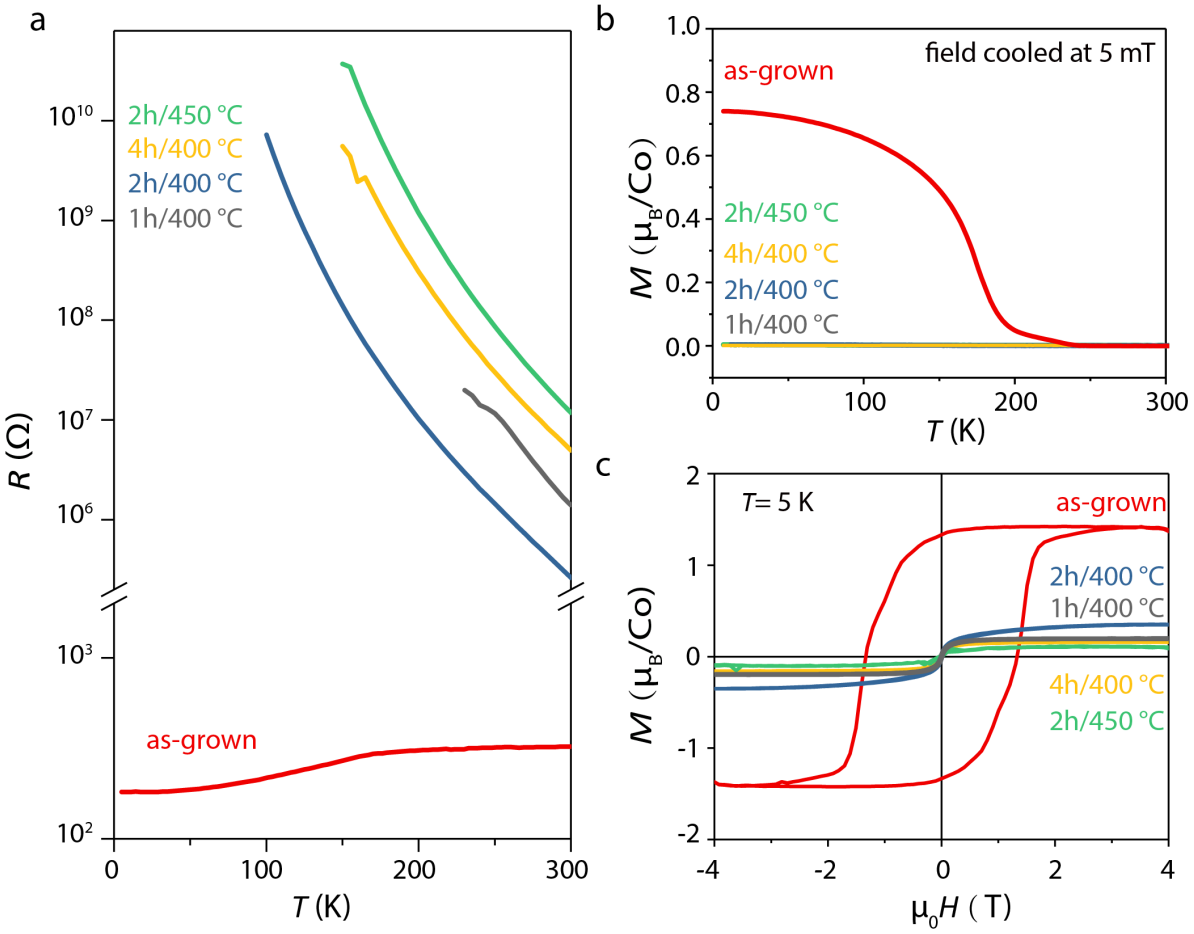


**Figure 4.17.:** Magnetic and transport properties of the as-grown samples, after 1 h annealing at 400°C, 2 h annealing at 400°C, after 4 h annealing at 400°C and after 2 h annealing at 450°C. a) Sheet resistance of as-grown and annealed LSCO in various states as a function of temperature (note that resistance above $\approx 10^{10}$ Ω is outside the measurable range of the PPMS). b) Temperature dependence of magnetization $M$ (T) curves under field cooling, measured by applying an in-plane magnetic field $\mu_0$H = 5 mT. c) Magnetic hysteresis loops measured at 5 K for LSCO films in different states.

### 4.4.3. Cation stoichiometry during the phase transition

To study the stoichiometry change of the LSCO thin film during phase transition, it is crucial to check the cation stoichiometry throughout the experiment. Hence, RBS analysis is used as a non-destructive method to track changes in cation stoichiometry. Fig. 4.18 displays the RBS spectra of the as-grown and BM phases. The heaviest ion (La) scatters at the highest energy, while the Sr thin film appears as a shoulder in the presence of the Sr substrate step. Co is observed as a peak atop the Ti substrate step. By fitting the spectrum, we can roughly estimate the stoichiometry of the sample. By comparing the RBS signal of the LSCO thin film in the as-grown and BM state, we found that the RBS signal of the BM state overlaps with the as-grown state, suggesting that the composition of La, Sr, and Co has not changed during the phase transition. This is consistent with the expectation that the cation mobility is typically limited

in low temperatures of the annealing experiment, leading to a constant cation stoichiometry throughout the experiment. In addition, Fig. 4.18 shows simulated RBS spectra, obtained using the software XRUMP to extract the stoichiometry, thickness, and mass density of the sample, indicating that the measured RBS signals are consistent with the expected nominal cation stoichiometry in both the as-grown and the fully transformed LSCO thin films.

Furthermore, one should note that RBS measurements are not sensitive to the oxygen stoichiometry. The oxygen content of the LSCO thin film (20 nm thick) makes up only 1% oxygen content in the probing volume of RBS (around 2000 nm), resulting in a significantly large error in determining the oxygen content of the thin films. Thus, the oxygen stoichiometry has to be determined by an alternative technique.

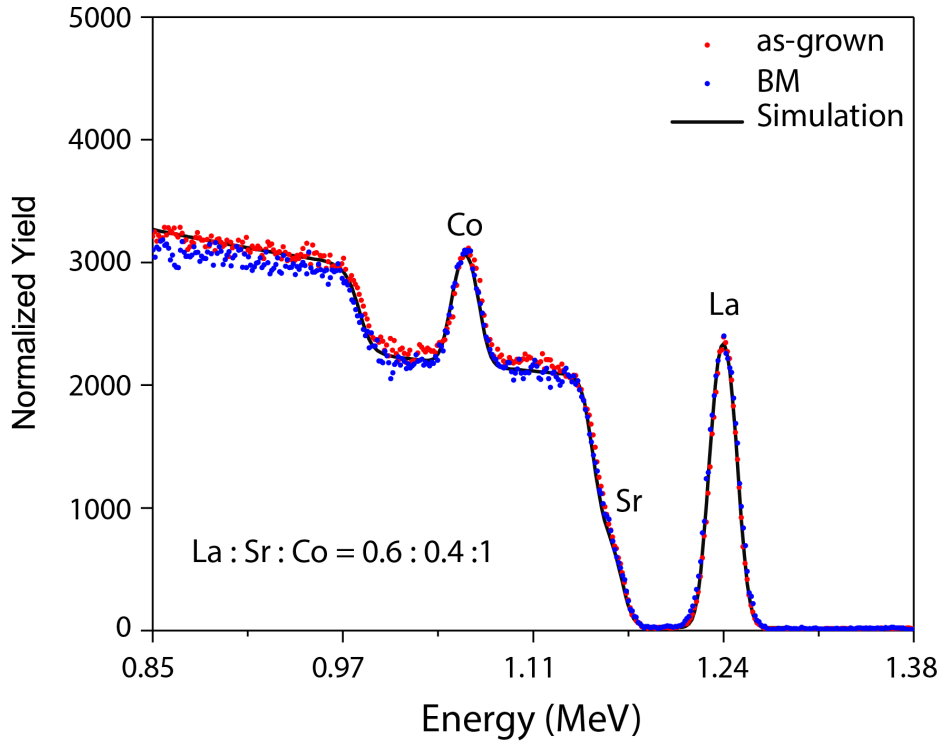


**Figure 4.18.:** RBS analysis of stoichiometry change of the 20 nm as-grown and BM LSCO thin film grown on a $SrTiO_3$ (001) substrate. The red and blue dots correspond to the RBS signal obtained from the as-grown state and the BM state samples (annealed at 450°C for 2 h), respectively. The data is simulated by the software XRUMP to extract the stoichiometry, thickness, and density of the sample. The simulation result is denoted with the black line.

### 4.4.4. Oxygen stoichiometry during the phase transition

To further correlate the magnetic, chemical, and structural properties of the LSCO thin film during the phase transition, PNR measurements were performed with *in-situ* annealing at the MAGREF beamline at Oak Ridge National Laboratory. As discussed in Section 4.2.3, the saturation magnetization of the 40 nm sample is the same as that of the 20 nm sample, showing no influence from the crack formation. Therefore, the 40 nm LSCO sample was utilized for the PNR measurement to achieve a high signal-to-noise ratio. PNR allows us to extract

magnetic information from the polarization dependence in neutron reflectivity (via the magnetic scattering length density, $m_{SLD}$) as well as information on the layer thickness, roughness, and chemical composition (via the nuclear scattering length density, $n_{SLD}$) based on a detailed fitting of the depth profile of underlying $n_{SLD}$ and $m_{SLD}$, respectively [141]. The PNR measurement was conducted for two similar samples with the same growth parameters and thicknesses. Both samples were measured by PNR at 300 K and 120 K in the as-grown state to ensure these samples had comparable material properties. The first sample was annealed *in-situ* at 400°C for 2 h at a pressure of $10^{-6}$ mbar, similar to how it was done in ex situ experiments (shown in Fig. 4.15). Then the sample was continuously annealed *in-situ* at 400°C for two more hours (4 h in total) before being cooled to 300 K and 120 K for a consecutive PNR experiment. The second sample was annealed *in-situ* at 450°C for 2 h to obtain the final BM structure before cooling down to measure PNR at 300 K and 120 K. Fig. 4.19 shows the PNR data for these four different states of LSCO thin film measured at 120 K in a 1 T saturation field. The splitting between the spin-up and spin-down channels observed for the as-grown film confirms the magnetization of 1 $\mu_B$/Co at 120 K (temperature below $T_c$), which is consistent with the *M-H* curve at 120 K (see Fig. 4.21). However, no splitting is observed after annealing for 2 h at 400°C, 4h at 400°C and 2 h at 450°C, respectively, which indicates that the magnetization for these states is close to zero. The evolution of the magnetization of the LSCO films in four different states is shown in Fig. 4.20 (a). This corroborates that the magnetic transition occurs at an early stage as the thin film is gradually reduced.

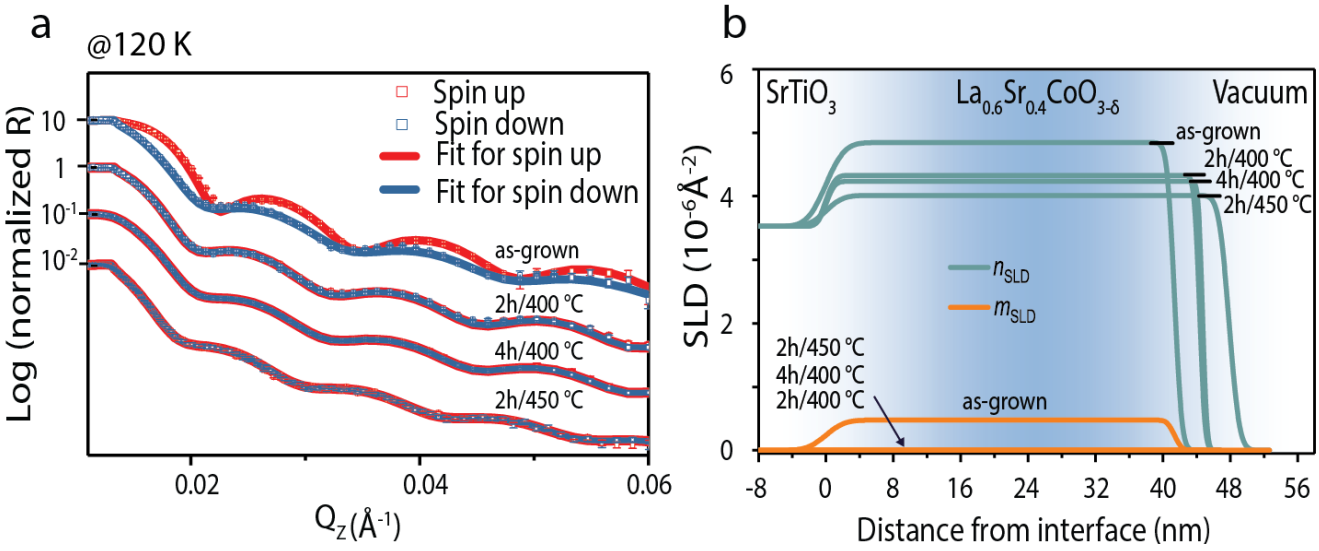


**Figure 4.19.:** PNR measurements of LSCO films at various oxygen deficient states at 120 K. a) Measured (open symbols) and fitted (blue and red solid lines) reflectivity curves for spin-up and spin-down polarized neutron beams are shown as a function of scattering vector component $Q_z$. b) The $n_{SLD}$ and $m_{SLD}$ depth profiles obtained from the fit to the data are shown as a function of distance from the interface.

Interestingly, PNR thickness fringes remain visible in all reflectivity data after annealing at different temperatures and times, showing that the smooth surface morphology of the as-grown thin film is preserved, which is consistent with the previous evaluation of XRD and AFM data

(Fig. 4.15 (b) and Fig. 4.16). Upon vacuum-annealing, the periodicity of the thickness fringes decreased indicating an expansion of the thin film during reduction. By comparing the relative thickness variation with the as-grown film, determined as $((t\text{-}t_{pv})/t_{pv})\%$ in Fig. 4.20 (b), we found a 10% increase in the thickness of the final BM structure compared to the as-grown PV state (with $t_{pv}$). Note that the average lattice parameter between each BO plane (Co-O plane) increased from 3.76 Å (PV) to 4.02 Å (BM) after the phase transition, as shown in Fig. 4.15 (c). This increase in out-of-plane lattice parameters is consistent with the 10% increase in total thickness observed by PNR (Fig. 4.20 (b)).

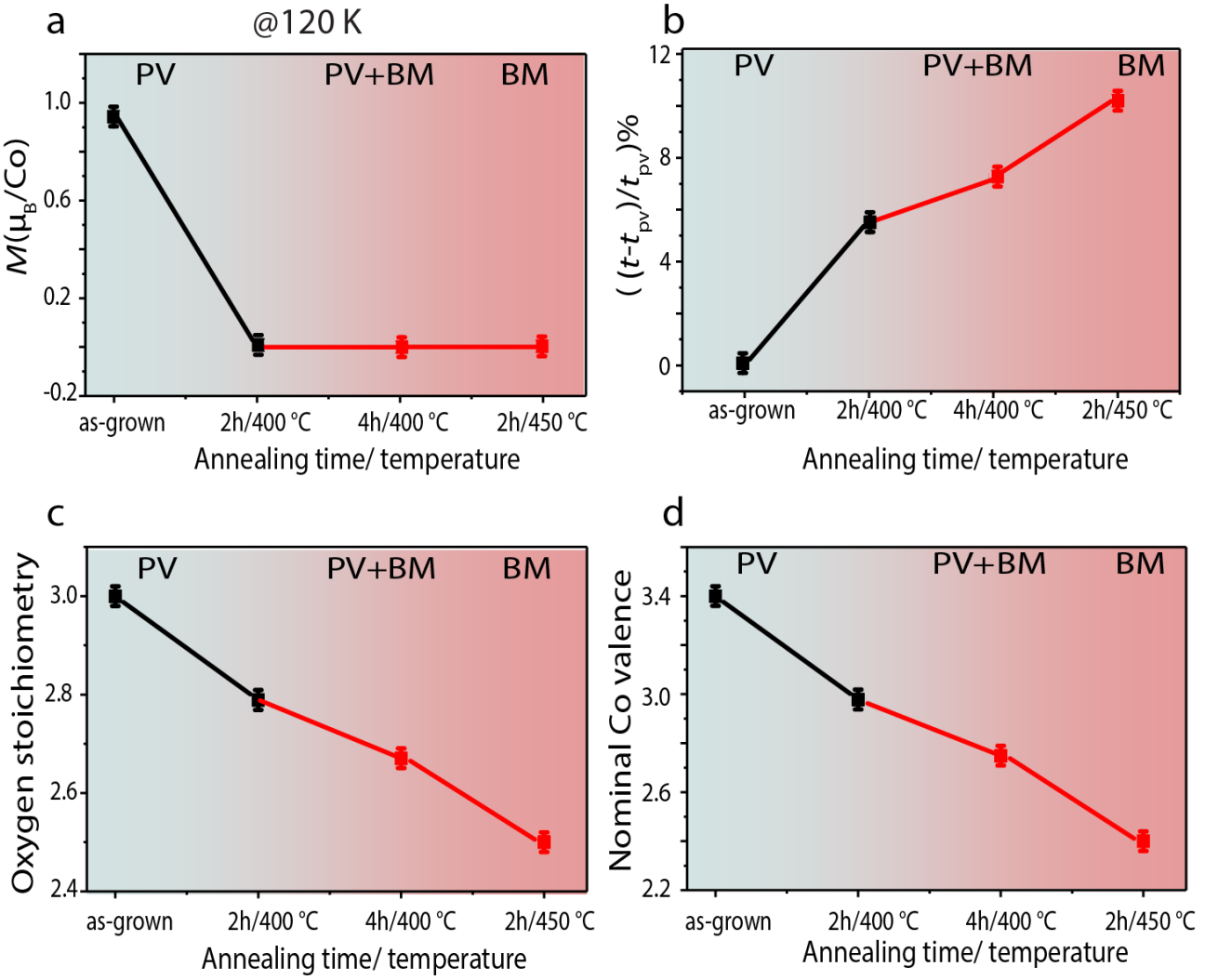


**Figure 4.20.:** a) and b) The evolution of magnetization and thickness variation as a function of annealing time and temperature. c) and d) Evolution of oxygen stoichiometry and nominal cobalt valence as a function of annealing time and temperature. Connecting lines in the plots are for better visibility.

To model the PNR data, we employed a single-layer model (interface+LSCO+surface). This simple model perfectly reproduced the experimental PNR data, allowing us to extract several parameters such as $n_{SLD}$, $m_{SLD}$ (1 emu/cc = $2.9 \times 10^{-9}$ Å$^{-2}$), oxygen content, magnetization, and thickness of the layer. Here, the oxygen stoichiometry is obtained from $n_{SLD}$, which is

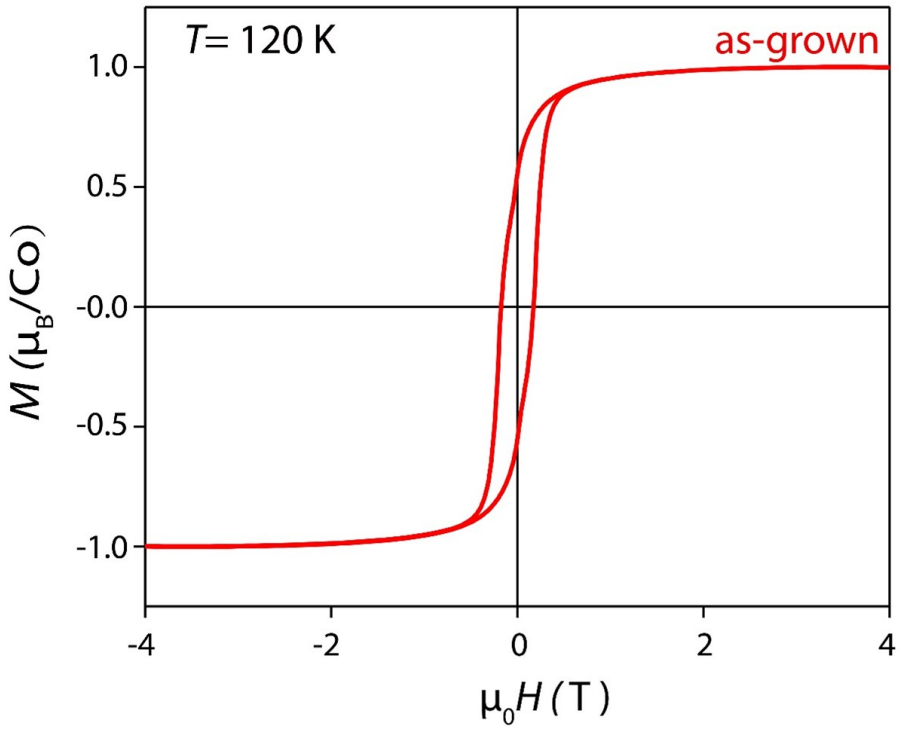


**Figure 4.21.:** Magnetic hysteresis loops measured at 120 K for the as-grown LSCO films. A saturation magnetization of approximately 1 $\mu_B$/Co is observed.

determined by the sum of the scattering length density of each element of the LSCO unit cell, weighted with its stoichiometry coefficient. Due to the relatively low temperature during annealing, cation mobility is typically limited, leading to a constant cation stoichiometry throughout the experiment, which has also been experimentally confirmed by RBS (see Fig. 4.18). Hence, the change of $n_{SLD}$ upon annealing must be attributed to a change in oxygen stoichiometry.

Most intuitively, this change in oxygen stoichiometry manifests itself in a shift of the critical edge for total reflection, which shifted to smaller $Q$-values for continuous reduction, indicating a reduction of $n_{SLD}$. Further details on the determination of $\delta$ are given in the experimental chapter of this thesis.

The fitting results of the depth profile of $n_{SLD}$ and $m_{SLD}$ are illustrated in Fig. 4.19 (b), showing the changes in both $n_{SLD}$ and $m_{SLD}$ during the annealing process. The corresponding fittings are displayed as red and blue solid lines in Fig. 4.19 (a). Consistent with previous SQUID experiments, $m_{SLD}$ is non-zero only for the as-grown film. Assuming uniform depth profiles for $n_{SLD}$ yields a sufficient representation of the experimental data, indicating that a uniform average oxygen deficiency is established throughout the thin films. The obtained $n_{SLD}$ values varied from $4.844 \times 10^{-6}$Å$^{-2}$ for the as-grown film to $4.330 \times 10^{-6}$Å$^{-2}$ after 2 h of annealing at 400°C, to $4.235 \times 10^{-6}$Å$^{-2}$ after 4 h of annealing at 400°C and finally to $4.012 \times 10^{-6}$Å$^{-2}$ after 2 h of annealing at 450°C film, corresponding to an oxygen stoichiometry of $La_{0.6}Sr_{0.4}CoO_{2.97\pm0.02}$, $La_{0.6}Sr_{0.4}CoO_{2.77\pm0.02}$, $La_{0.6}Sr_{0.4}CoO_{2.67\pm0.02}$, and $La_{0.6}Sr_{0.4}CoO_{2.50\pm0.02}$ (see Fig. 4.20 (c)). Note that $La_{0.6}Sr_{0.4}CoO_{2.97\pm0.02}$ is consistent with the stoichiometric PV ($ABO_3$), while $La_{0.6}Sr_{0.4}CoO_{2.50\pm0.02}$ is consistent with the fully transformed BM. Assuming lo-

cal charge neutrality, the nominal valence state of cobalt can be estimated, yielding about +3.34 for the as-grown sample, which continuously reduces to about +2.4 in the final BM structure, as shown in Fig. 4.20 (d). Note that the numerical error propagated from the fitting was below physical reasoning, given the limitations and assumptions made to describe the experimental data. Therefore, an error estimation of ±0.02 for $\delta$ was determined by manually adjusting the parameters until there is a significant deviation between the fit and the experimental data.

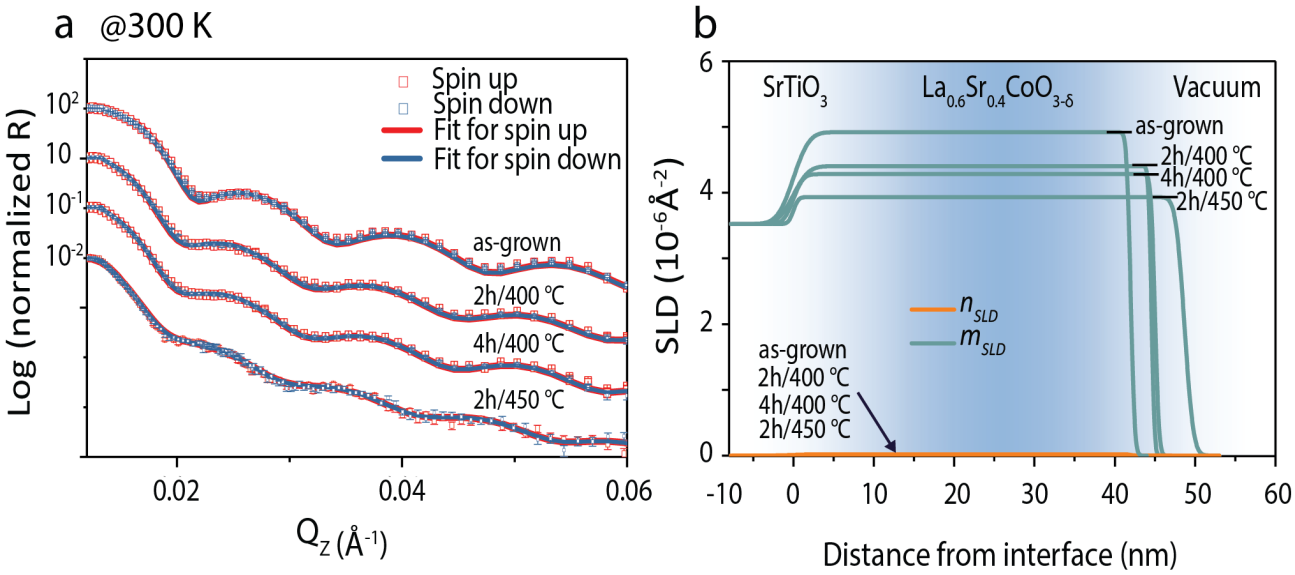


**Figure 4.22.:** PNR measurements of LSCO films at various oxygen deficient states at 300 K. a) Measured (open symbols) and fitted (red and blue solid lines) reflectivity curves for spin-up and spin-down polarized neutron beams are shown as a function of scattering vector component $Q_z$. b) The $n_{\mathrm{SLD}}$ and $m_{\mathrm{SLD}}$ depth profiles obtained from the fit to the data are shown as a function of distance from the interface.

PNR measurements were performed both at 120 K and 300 K. To ensure fit accuracy, PNR data collected at 300 K and 120 K were fitted with the GenX software using the same model to ensure that the chemical scattering length density remains the same. For the PNR data at 300 K, in Fig. 4.22, we did not observe a splitting between the spin-up and spin-down channels of the as-grown film, which is consistent with a vanishing magnetization at 300 K (also shown in Fig. 4.23 (a)). This is because the measurement temperature is higher than $T_c$ (180 K, see Fig. 4.17 (b)) of the as-grown film. Fig. 4.20 (b) shows a similar thickness variation result as the measurement at 120 K, indicating a 10% variation in the thickness of the BM film compared to the as-grown film. Note that the thickness of the thin film increases as it is heated from 120 K to 300 K. Fig. 4.20 (b) shows a slight increase in thickness compared to the data at 120 K due to thermal expansion. As for the oxygen stoichiometry (see Fig. 4.20 (c)) and the corresponding nominal cobalt valence (see Fig. 4.20 (d)), it shows the same results as the PNR data at 120 K, since the change in temperature does not affect the oxygen content.

In summary, the results show that the chemical response to the low oxygen pressure under annealing conditions continues even further after the FM state has already disappeared in the

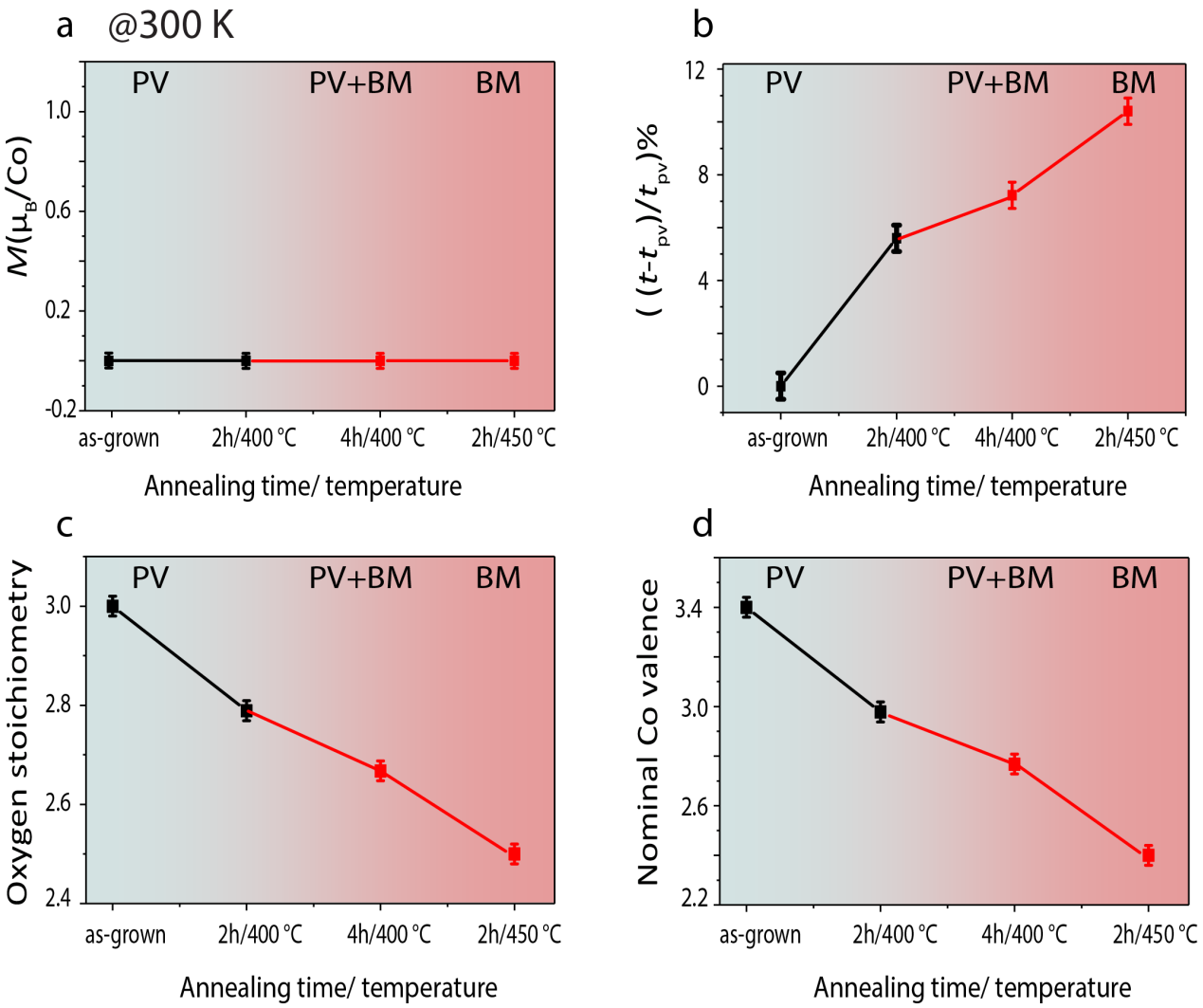


**Figure 4.23.:** a) and b) The evolution of magnetization and thickness variation as a function of annealing time and temperature is plotted. c) and d) The evolution of oxygen stoichiometry and nominal Cobalt valence as a function of annealing time and temperature is plotted.

initial phase of reduction. At the same time, a quantitative estimation of the oxygen content at different stages of the reduction process allows us to associate the appearance of MIT, the transition of FM-to-non-FM, and the transition of PV to BM with a specific oxygen content observed in these samples. In particular, after 2 hours of annealing, an insulating and non-FM state is achieved while maintaining the PV structure at an oxygen content of about 2.77 (±0.02). In contrast, the first appearance of the BM phase is observed only after a 4-hour annealing at 400°C, which reflects the lower oxygen content of about 2.67 (±0.02).

### 4.4.5. Structural transition is apart from the electronic and magnetic transition

Summarizing all the experimental data, the process of the topotactic phase transition occurs in three stages:

1. The concentration of oxygen vacancies increases during the initial reduction process, while the thin film remains in the PV structure. In this stage, the concentration of vacancies is below the critical ordering threshold. The statistical distribution of vacancies leads to a local breakdown in the double exchange paths between Co ions and, simultaneously, to a gradual change in the nominal oxidation state of the Co ions towards lower values. Since both ferromagnetism and metallic conductivity originate from the double exchange of high-spin $Co^{3+}$ and high-spin $Co^{4+}$ [131, 132], the system quickly becomes non-ferromagnetic (non-FM) and insulating, while the film remains in the PV structure. As shown in above, this transition already occurs in the initial phase of the reduction process, with an oxygen stoichiometry around 2.77 (2 h of annealing at 400 °C), reflecting a lower limit for the electronic and magnetic transition. The nominal oxidation number of cobalt varies from +3.34 for the as-grown film to +2.94 for this initially reduced PV film. Therefore, different mechanisms may contribute to the electronic and magnetic phase transitions, including the absence of $Co^{4+}$ after initial reduction and a potential percolation threshold reached in the oxygen sublattice after the release of significant amounts of oxygen.

2. Upon further annealing, the film transitions into a mixed state of the PV and BM phases. At this stage, oxygen vacancies reach a critical value and become partially ordered, leading to the local formation of the BM structure. The corresponding oxygen stoichiometry for this initial ordering lies between 2.77 and 2.67 (obtained after 4 h of annealing at 400 °C), where the first indications of vacancy-ordering were observed. In this intermediate stage, the nominal cobalt oxidation state corresponds to +2.74. This is consistent with the reported value in the literature Ref. [90].

3. Finally, oxygen vacancies are completely and coherently ordered throughout the entire film, resulting in a uniform BM structure. At this stage, we observe an oxygen stoichiometry of 2.50, which is consistent with the theoretical oxygen content in the BM structure. The nominal oxidation number of cobalt changes to +2.4. Similar to the reduced films in stages 1 and 2, the film exhibits non-FM and insulating behavior due to the breakdown of the double exchange paths, marking the final stage of the transition process.

In summary, the electronic and magnetic transitions begin during the early PV structure stages as oxygen vacancy concentration and distribution change. However, these transitions do not align with the structural phase transition, which requires further vacancy ordering and completes only when the film fully transforms to the BM structure. This suggests that electronic and magnetic properties respond more to local oxygen vacancy configurations and cobalt oxidation state changes than to the final structural rearrangement.

# 4.5. Reversibility of the topotactic phase transition in LSCO thin films

As demonstrated in Section 4.4, it is evident that changes in oxygen concentration can induce a topotactic phase transition from PV to BM. However the question of reversibility versus irreversibility of this phase transition is a further important aspect. It is essential for understanding the mechanisms of the topotactic phase transition and for providing insights for prospective applications. Therefore, this chapter will mainly focus on investigating the structural, chemical, electronic, and magnetic reversibility during the topotactic phase transition of LSCO thin films under repeated cycling between reducing and oxidizing atmospheres.

## 4.5.1. Structural reversibility during the topotactic phase transition

To investigate the structural reversibility of the phase transition, I utilized a 20 nm LSCO thin film fabricated via PLD to induce the topotactic phase transition between PV and BM (see Fig. 4.24 (a)). Fig. 4.24 (b) depicts the experimental setup, where the sample was located in the middle of a tube furnace and was heated by the thermal radiation and conduction emitted from the heating coils. By adjusting the gas flow, we can vary the oxygen partial pressure to initiate the phase transition from PV to BM and vice versa. Specifically, the LSCO film underwent annealing in a Ar+4%$H_2$ reducing environment to initiate the phase transition from PV to BM. Conversely, the gas was switched to pure $O_2$ to trigger the phase transition from BM to PV. This approach allowed us to repeatedly induce the phase transition between PV and BM.

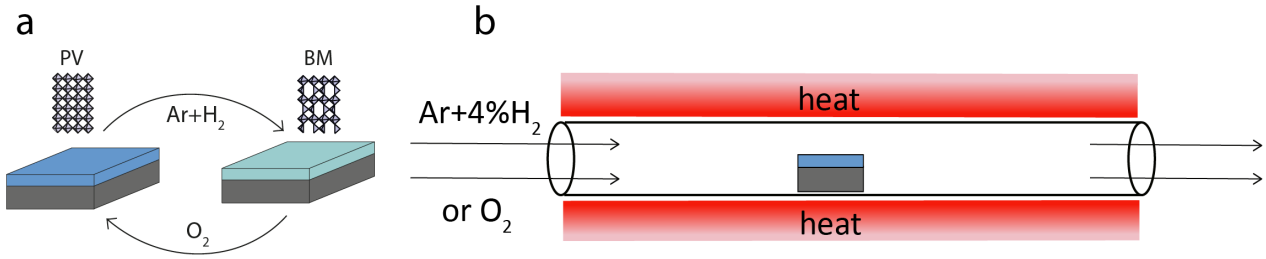


**Figure 4.24.:** a) Illustration of the topotactic phase transition between PV and BM achieved by altering the annealing atmosphere. b) The illustration depicts the tube furnace used in the annealing experiments. The sample was heated by the thermal radiation emitted from the heating coils, and the annealing environment could be switched from high oxygen partial pressure ($O_2$) to low oxygen partial pressure (Ar+4%$H_2$) by adjusting the gas flow.

The results of this process are illustrated in Fig. 4.25 (a) and (b), which present the structural analysis using XRD undergoing the phase transition between PV and BM for up to 20 cycles. As depicted, the as-grown LSCO exhibits a typical perovskite structure, characterized by PV peaks denoted as $(001)_{PV}$ and $(002)_{PV}$, consistent with the relatively oxidizing growth conditions. These peaks, accompanied by distinct Kiessig fringes (visible in the enlarged view

in Fig.4.25 (b)), attest to the films' coherent crystal structure with well-defined interfaces and surface morphology. Upon annealing the sample at 300°C in a Ar+4%$H_2$ atmosphere for two hours (depicted by the XRD data as the blue curve labeled as $1_{BM}$), the $(001)_{PV}$ and $(002)_{PV}$ peaks vanish. Simultaneously, additional peaks emerge, denoted as $(002)_{BM}$, $(004)_{BM}$, $(006)_{BM}$, $(008)_{BM}$, and $(00\underline{1}0)_{BM}$, indicating the initial formation of the BM long-range ordered structure of LSCO. Note that in this case, the structural phase transition occurs at a lower temperature compared to annealing in vacuum, as discussed in Section 4.4, where it takes place after 2 hours of annealing at 450°C. This discrepancy can be attributed to the presence of the Ar+4%$H_2$ atmosphere. In this environment, hydrogen reacts with any residual oxygen present, converting it into water vapor and effectively removing all sources of residual oxygen from the gas mixture. Consequently, the oxygen partial pressure is significantly reduced, leading to faster transition dynamics.

Following this step, we reoxidized the LSCO film to its original PV structure by annealing it in a pure $O_2$ environment in the same tube furnace. After two hours of annealing at 300°C, the structure of the sample is depicted as a red curve labeled as $1_{PV}$ in Fig. 4.25 (a) and (b), showcasing the sample's structure resembling the as-grown LSCO film, featuring typical $(001)_{PV}$ and $(002)_{PV}$ structural peaks. Remarkably, the Kiessig fringes remained intact, signifying the preservation of lattice coherence and smooth surface morphology.

By alternating the gas between Ar+4%$H_2$ and $O_2$ during the two-hour annealing cycles, we induced the topotactic phase transition in LSCO 20 times. Specifically, the XRD data for structural analysis of the 1st, 5th, 10th, 15th, and 20th cycle is presented in Fig. 4.25 (a) and (b). Here, we denote the 1st, 5th, 10th, 15th, and 20th transition of the as-grown LSCO film to the BM structure as $1_{BM}$, $5_{BM}$, $10_{BM}$, $15_{BM}$, and $20_{BM}$, respectively. Conversely, we represent the 1st, 5th, 10th, 15th, and 20th instances of reoxidizing the LSCO film back to the PV structure as $1_{PV}$, $5_{PV}$, $10_{PV}$, $15_{PV}$, and $20_{PV}$. As depicted in the figure, the LSCO film undergoes transitions between the PV and BM phases for up to 20 cycles. In each cycle, either the PV or BM phase maintains its original structural integrity without the emergence of additional peaks. Notably, the film preserves the Kiessig fringes throughout the recorded cycles, suggesting that the majority of the thin film maintains lattice coherence for all 20 cycles.

To continue further into the analysis, we plot the changes in peak intensity and position of the $(002)_{PV}$ peak (denoted as red arrows in Fig. 4.25 (b)) and the $(008)_{BM}$ peak (denoted as blue arrows in Fig. 4.25 (b)) in Fig. 4.25 (c) and (d). From Fig. 4.25 (c), it is evident that the peak intensity of the PV phase remains at 85% after the 1st cycle compared to the as-grown film. However, after the 20th cycle, the intensity of the $(002)_{PV}$ peak drops to 50% compared to the origin. This trend is consistent with the $(008)_{BM}$ peak, which retains only 50% intensity after the 20th cycle, indicating a loss of lattice coherence or possible degradation in certain regions of the film. Furthermore, as depicted in Fig. 4.25 (d), the peak position of the $(002)_{PV}$ remains relatively stable, indicating that the out-of-plane lattice constant of the PV phase remains largely unchanged. In contrast, the peak position of the $(008)_{BM}$ begins to shift

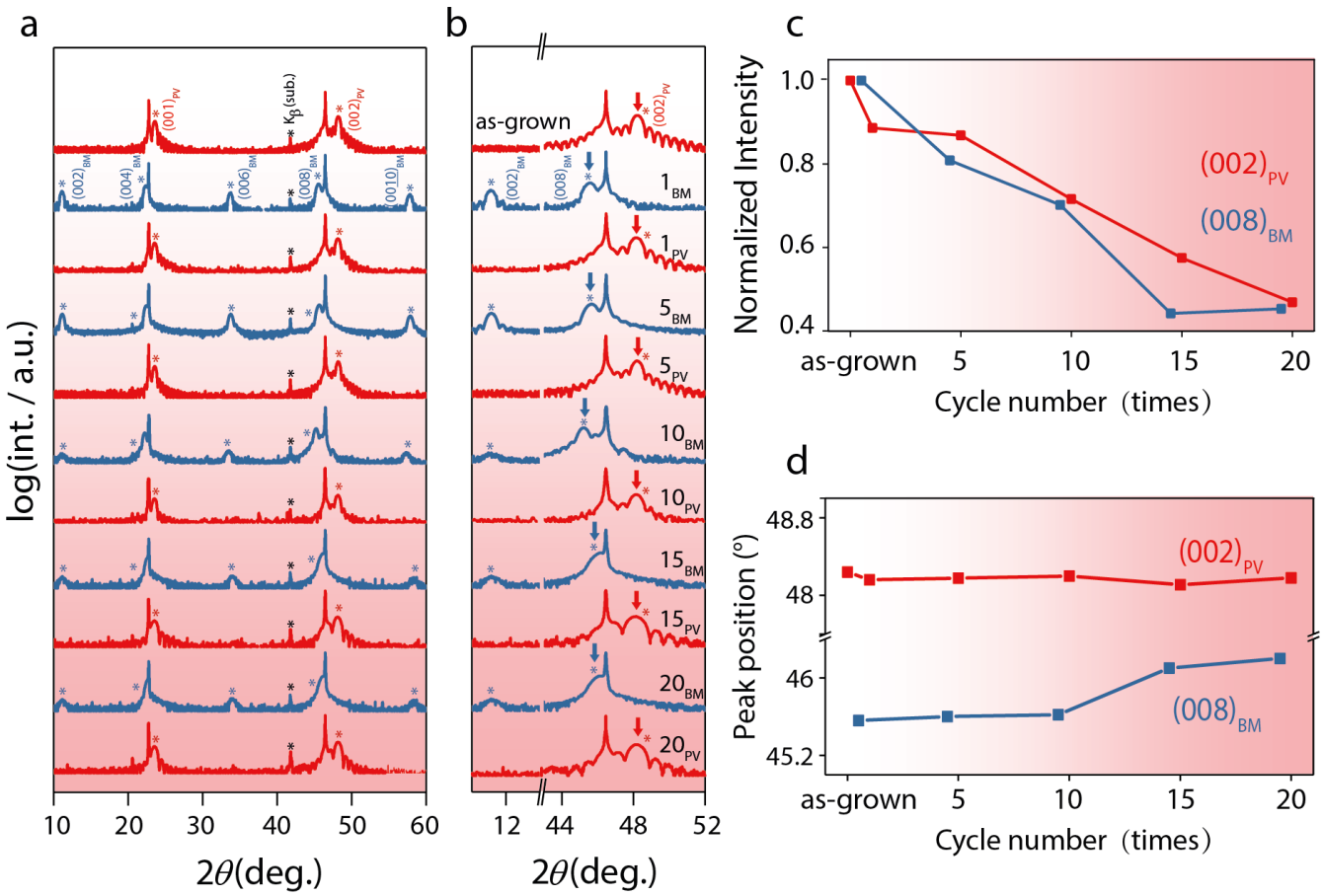


**Figure 4.25.:** Structural evolution of the LSCO film under a 20-cycle phase transition is depicted. Panel a) shows the XRD diffractogram for $2\theta$ in the range 10–60° during the 20-cycle phase transition. Panel b) provides an enlarged view of the corresponding XRD diffractograms from Fig. 4.25 (b). Panel c) illustrates the evolution of the intensity of the (002)PV and (008)BM peaks, while panel d) depicts the evolution of the (002)PV and (008)BM peak positions during the 20-cycle phase transition.

to higher angles after the 15th cycle, suggesting a reduction in the out-of-plane lattice constant of the BM phase, possibly attributed to the expansion of the in-plane lattice constant of the BM phase by lattice relaxation. As the cycles increase, the width of the PV or BM peaks also widens, indicating increasing lattice incoherence in the sample.

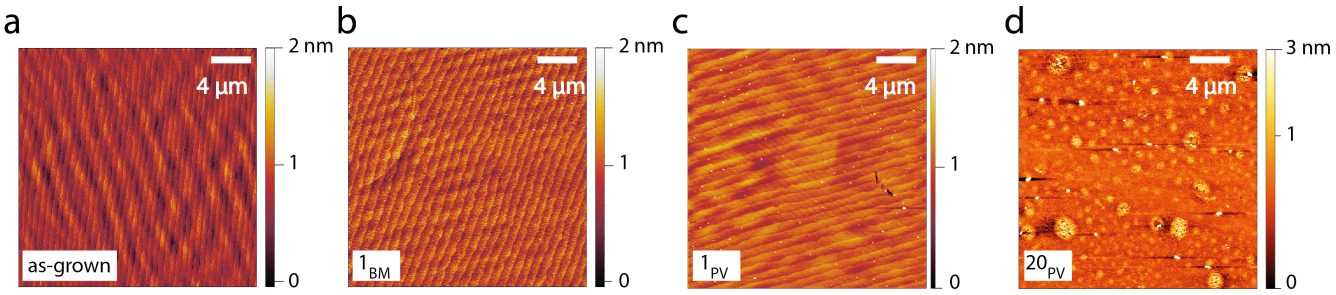


**Figure 4.26.:** Evolution of surface morphology of the LSCO film under a 20-cycle phase transition is depicted. Panels a), b), c), and d) show the surface morphology of the as-grown, $1_{BM}$, $1_{PV}$, and $20_{PV}$ LSCO thin films, respectively. The size of the AFM images are $20 \times 20$ $\mu m^2$.

To further explore the structural evolution of the LSCO film during the 20-cycle phase transition, AFM was utilized to examine the surface morphology. The 20 × 20 $\mu m^2$ AFM images of the as-grown, $1_{BM}$, $1_{PV}$, and $20_{PV}$ LSCO films are displayed in Fig. 4.26. It is apparent that the as-grown, $1_{BM}$, and $1_{PV}$ films maintain a clear step-terrace structure, indicating the preservation of the surface morphology after the 1st cycle of phase transition. However, following the 20th cycle of phase transition, the surface of the LSCO film undergoes a noticeable morphology change, becoming significantly rougher. This roughening is marked by the emergence of numerous island-shaped clusters on the surface, which can reach heights of up to 3 nm. As a result, the overall surface roughness is considerably increased.

In summary, during the initial cycle of the topotactic phase transition, the LSCO thin film maintained a good surface morphology, with approximately 85% of the structural coherence preserved. However, as the transition progressed, significant changes occurred. After 15 cycles, the position of the BM phase shifted to a higher angle, indicating a reduction in the out-of-plane lattice constant. Subsequently, after 20 cycles, the surface morphology became rougher, with the emergence of island-shaped clusters up to 3 nm in height. Concurrently, the preservation of structural coherence diminished, with only 50% remaining compared to the original state. These observations suggest substantial structural alterations within specific regions of the LSCO thin films during the topotactic phase transition.

### 4.5.2. Electronic and magnetic reversibility during the topotactic phase transition

To elucidate the relationship between the structural properties of the phase transitions and their magnetic and electronic characteristics, a series of magnetic and electronic experiments were conducted. Fig. 4.27 (a) illustrates the electrical sheet resistance determined in van der Pauw geometry across the cycles of repeated PV-to-BM-to-PV transitions. The color spectrum, ranging from red to dark red, depicted the sheet resistance of the PV structure at different stages: as-grown, 1st ($1_{PV}$), 5th ($5_{PV}$), 10th ($10_{PV}$), 15th ($15_{PV}$), and 20th ($20_{PV}$) cycles of the transition. Notably, the sheet resistance of these states remained below 400 Ω within the temperature range of 5 K to 300 K. Furthermore, a discernible decrease in sheet resistance was observed upon cooling the as-grown film, indicative of its inherent metallic behaviour. This metallic behaviour persisted until the 15th cycle. However, there was a subsequent rise in sheet resistance observed during the cooling phase of the 15th and 20th cycles, indicating a transition from metallic behavior to insulating behavior following the cycles. The color spectrum, ranging from light blue to dark blue, represents the sheet resistance of the BM structure at different stages: 1st ($1_{BM}$), 5th ($5_{BM}$), 10th ($10_{BM}$), 15th ($15_{BM}$), and 20th ($20_{BM}$) cycles of the transition. Notably, all these BM states exhibit sheet resistances exceeding 2 MΩ. As cooling down the sample, the sheet resistance consistently increased, being typical of insulating behaviour. At temperatures below 250 K, the resistance surpasses the measurable range of the PPMS device, thus no further data points could be recorded.

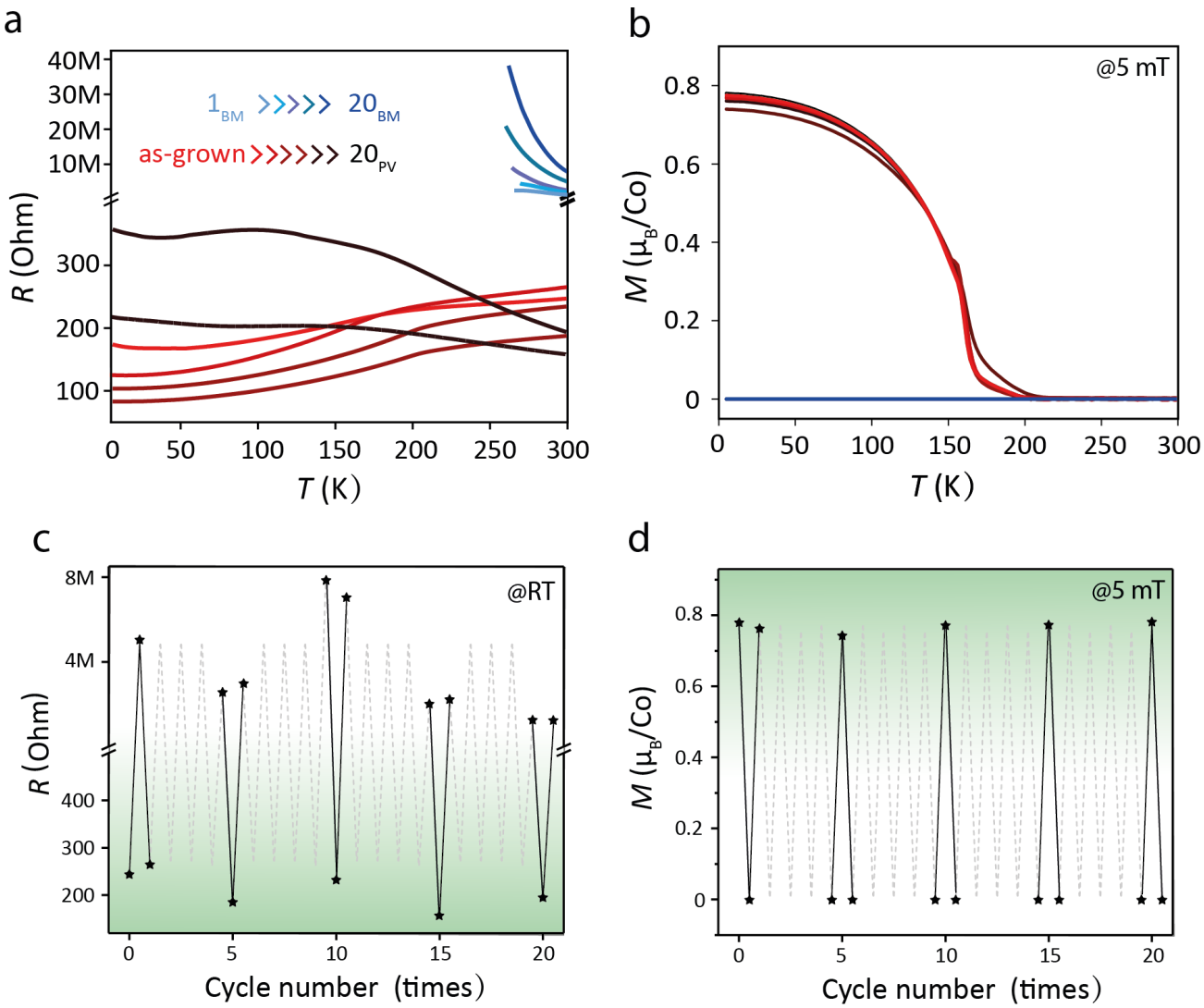


**Figure 4.27.:** a) Temperature-dependent sheet resistance of LSCO thin films during the 20-cycle PV-BM-PV transition. Light blue to dark blue arrows show BM phase resistance at the 1st, 5th, 10th, 15th, and 20th cycles. Red to dark red arrows indicate PV phase resistance at the same cycles. b) Temperature versus magnetization curve at 5 mT during the 20-cycle PV-BM-PV transition. c) Summary depicting the variation in room temperature resistance throughout the 20-cycle PV-BM-PV transition. The solid dots represent the measured resistance values for the 1st, 5th, 10th, 15th, and 20th cycles of the PV or BM phase (with upper dots indicating the BM phase and lower dots indicating the PV phase). Meanwhile, the dashed line and dots correspond to the unmeasured cycles. d) Summary illustrating the variation in saturation magnetization during the 20-cycle PV-BM-PV transition. Similar to Figure c, the solid dots represent the measured saturation magnetization values for the 1st, 5th, 10th, 15th, and 20th cycles of the PV or BM phase. The upper dots indicate the PV phase, while the lower dots indicate the BM phase. Meanwhile, the dashed line and dots correspond to the unmeasured cycles.

Regarding the magnetic properties, Fig. 4.27 (b) depicts the determined magnetic moment per Co ion versus temperature under a 5 mT magnetic field. The $M$ vs. $T$ curve of the as-grown and restored PV states highly overlap and exhibit clear ferromagnetic behaviour with a Curie temperature $T_c \approx 180\,\mathrm{K}$. In contrast, all BM states display non-magnetic behaviour with magnetization close to 0. This observation aligns with our previous study in Section 4.4, where

the PV phase demonstrates typical ferromagnetic characteristics with a Curie temperature $T_c \approx 180\,\mathrm{K}$, while the BM phase does not exhibit ferromagnetic properties.

To comprehensively understand the electronic and magnetic phase transitions occurring during the cycling process, room-temperature sheet resistance and saturation magnetization are shown for various cycles in Fig. 4.27 (c) and (d). In this representation, the PV states are depicted in green, while the BM states appear in white. Specifically, integer cycle numbers (0, 1, 5, 10, 15, and 20) correspond to the 1st, 5th, 10th, 15th, and 20th cycles of the PV phase, respectively. Additionally, decimal numbers (0.5, 4.5, 5.5, 9.5, 10.5, 14.5, 15.5, 19.5, and 20.5) represent the intermediate BM state during the 1st, 4th, 5th, 9th, 10th, 14th, 15th, 19th, and 20th cycles. Fig. 4.27 (c) reveals that all the as-grown and restored PV phases exhibit sheet resistance below 300 Ω, while all the BM states display insulating behaviour with sheet resistance above 2 MΩ. Moreover, as demonstrated in Fig. 4.27 (d), the saturation magnetization of the as-grown and restored PV states ranges approximately from 0.76 to 0.79 $\mu_\mathrm{B}$/Co, whereas the saturation magnetization for all the BM states is close to 0 $\mu_\mathrm{B}$/Co. This observation suggests the reversible control of the ferromagnetic-to-non-ferromagnetic transition and room temperature metal-insulator transition can be achieved up to 20 cycles.

Combining these findings with the discussed results from Fig. 4.27 (a) and (b), it becomes evident that the magnetic behaviour is likely to be fully restored, as demonstrated by the large overlap in the shape of the $M$ vs. $T$ curves and the saturation magnetization values in both PV and BM states. However, while the room temperature conductivity can be restored over 20 cycles, as discussed in Fig. 4.27 (a), the metallic behaviour upon cooling is not fully restored, as indicated by the lack of significant overlap in the measured curves. Moreover, after the 15th cycle, the PV phase transitions to an semiconducting state, as evidenced by the semiconductor-/insulator-type temperature dependence of the sheet resistance. These findings suggest that while the magnetic properties are likely to be fully restored, the electronic behaviour cannot be fully recovered as the number of cycles increases.

## 4.5.3. Probing the electronic and chemical dynamics in the cycling of LSCO thin film

### 4.5.3.1. Electronic and chemical alterations in the first redox cycle

To gain a comprehensive understanding of the structural and electronic changes during the cycling process, it is crucial to examine the electronic and chemical properties throughout the topotactic phase transition. Hard X-ray photoelectron spectroscopy (HAXPES) was employed to investigate these changes in LSCO upon redox cycling. This work was supported by Dr. Christoph Schlüter (DESY, Hamburg) with data analysis conducted by Dr. Moritz L. Weber (Forschungszentrum Jülich). For this investigation, we analyzed the valence band as well as the core-level spectra of Co 2$p$, Sr 3$d$, La 3$d$, and O 1$s$. Comparisons were made between the as-grown (PV), the 1st reduced BM phase ($1_\mathrm{BM}$), and the 1st reoxidized PV state ($1_\mathrm{PV}$) of

LSCO, as shown in Fig. 4.28. A photon energy of $E_{\mathrm{hv}} = 3400$ eV was utilized, which provided mean escape depths ranging from 3.7 nm to 4.6 nm for the various XPS spectra [142]. These measurements were taken at a photoemission angle of $\alpha = 5°$ [143], enabling a detailed analysis of the chemical and electronic transitions occurring during the phase transition.

Fig. 4.28 (a) presents the valence band spectra for the as-grown, $1_{\mathrm{PV}}$, and $1_{\mathrm{BM}}$ states. Upon thermal reduction, the $1_{\mathrm{BM}}$ sample shows a Fermi edge shift of approximately $\Delta$BE ~ 1.1 eV towards higher binding energies compared to the as-grown state, as determined by a linear fit to the leading edge of the valence band spectra. This observation aligns with previous studies on the topotactic phase transition of $SrCoO_{3-\delta}$ [144], which reported a smaller shift ($\Delta$BE ~ 0.3–0.4 eV). The decreased density of states at the Fermi edge suggests the formation of an insulating state in the LSCO thin film upon the formation of the BM phase under reducing conditions. Notably, this shift is reversible, and the metallic behavior of the sample is restored after reoxidation. Note that a binding energy (B.E.) correction was applied to the reduced $1_{\mathrm{BM}}$ sample to account for energy calibration shifts. This adjustment allows for accurate comparison of the Fermi edge positions across different states, as shown in Fig. 4.28(a).

These results are in agreement with the observed changes in the Co $2p$ signature across the various redox states, which are largely reversible (Fig. 4.28 (b)). Satellite peaks, indicated by arrows, are visible at higher binding energies relative to the main Co $2p_{3/2}$ and Co $2p_{1/2}$ peaks. After reduction, the satellite peaks shift towards lower binding energies, leading to a less pronounced intensity valley between the main and satellite peaks, while an intensity shoulder emerges. This shift in the binding energy of the satellite peaks relative to the main peaks likely reflects the change in the average oxidation state of the cobalt cations. Specifically, a shift towards the main peaks after thermal reduction suggests a decrease in the average oxidation state of the cobalt cations [145, 146], while reoxidation is associated with an increase in the average oxidation state, as evidenced by a shift towards higher binding energies. This is consistent with Section 4.4.4, where the PNR results indicate a gradual decrease in the nominal cobalt valence as the oxygen content decreases.

In contrast, significant irreversible chemical changes are evident from the shifts in binding energy and altered peak shapes in the Sr $3d$, La $3d$, and O $1s$ core-level spectra across the various redox states, suggesting the formation of a mixed surface phase during the redox cycling of the sample (Fig. 4.28 (c)-(e)). For the as-grown state, the Sr $3d$ core-level spectra are predominantly characterized by a single doublet corresponding to the PV lattice (BE ~1131.5 eV), with only minor secondary compounds present (Fig. 4.28 (c)). Upon reduction, the core-level spectrum shifts to higher binding energies, and the intensity valley between the Sr $3d_{5/2}$ and Sr $3d_{3/2}$ peaks become less pronounced. This indicates the formation of a secondary component and changes in the chemical environment of the Sr cations at the LSCO surface. Although the initial position of the Sr $3d$ spectrum associated with the PV lattice is partially recovered after reoxidation, a notable secondary component emerges at higher binding energy (135.5 eV) compared to the PV oxide lattice [147–149]. These observations indicate the formation of a

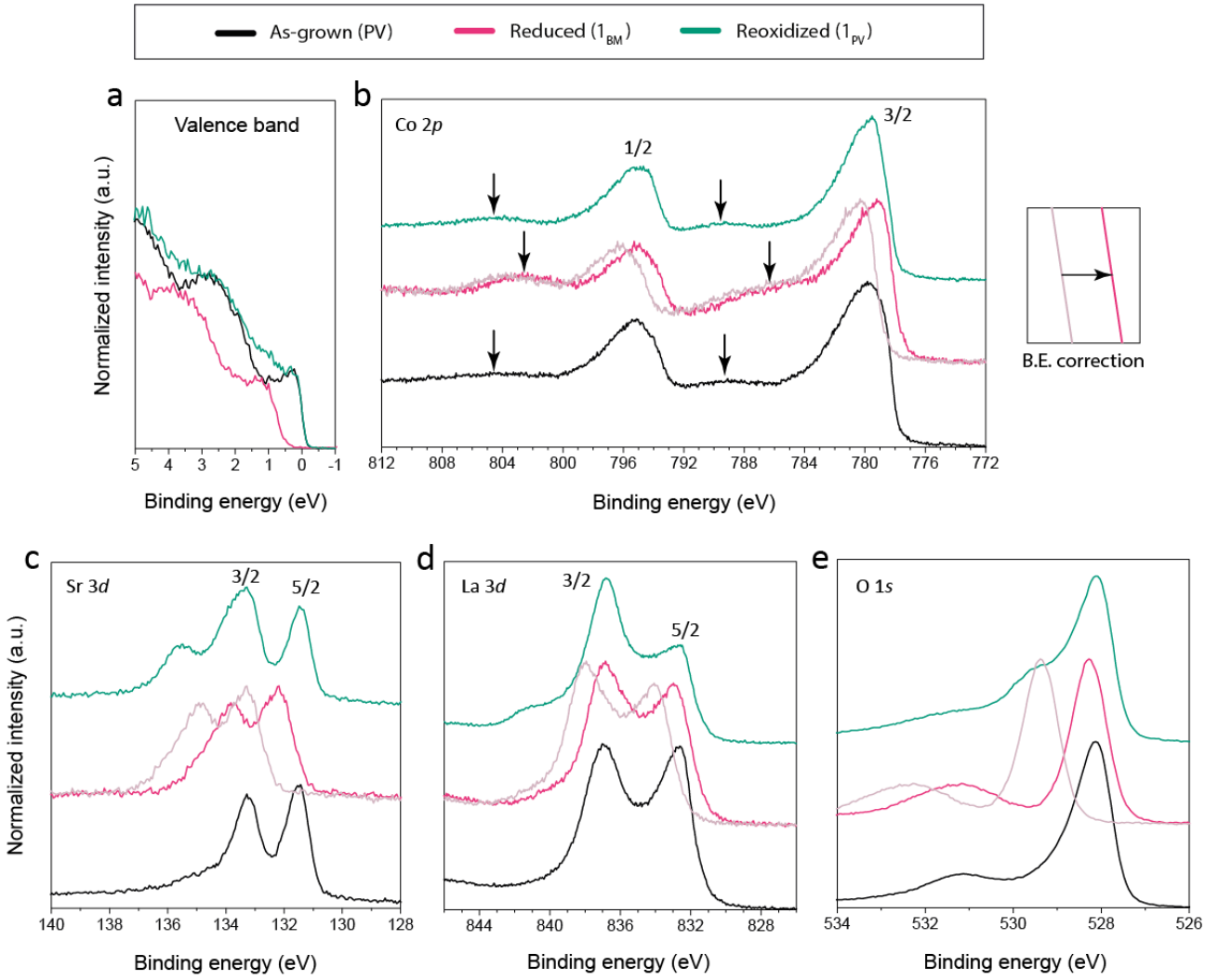


**Figure 4.28.:** Ex-situ HAXPES analysis of LSCO in the as-grown state (PV), reduced state ($1_{BM}$, annealing conditions: $p(Ar+4\%H_2)$ = 1 bar, T = 300°C, t = 120 min) and the 1st reoxidized state ($1_{PV}$, annealing conditions: $p(O_2)$ = 1 bar, T = 300°C, t = 120 min). (a) Valence band spectra. (b) Co 2*p* core level spectra. Arrows highlight satellite peaks. (c) Sr 3*d* core level spectra; (d) La 3*d* core level spectra and (e) O 1*s* core level spectra. Spectra in (a) are normalized to the background region; spectra in (b-c) are normalized to the maximum intensity and are shown with an offset along the y-axis for improved clarity. The binding energy was aligned with respect to the Fermi edge of LSCO in the metallic as-prepared state. The mean escape depth is calculated as an indicator for information depth to be d = 3.7 nm - 4.6 nm across the different core-level spectra.

surface phase influenced by consecutive thermal reduction and oxidation.

Similarly, changes are visible in the La 3*d* core-level after thermal reduction, where the relative weight of the intensity of the La $3d_{5/2}$ multiplet is considerably altered relative to the as-grown state. Consistent with our observations regarding the Sr signature, even stronger changes are observed after thermal reoxidation (Fig. 4.28 (d)). Here, a pronounced high binding energy intensity shoulder emerges resulting in strong changes of the peak shape. These observations point towards surface chemical changes in the form of the formation of a A-site cation rich surface phase that may consist of hydroxides, carbonates, or non-PV oxides [150, 151], already

during a single redox cycle (PV→$1_{BM}$→$1_{PV}$). This is further confirmed by the evolution of a new component in the O 1*s* core level spectrum at approximately BE ~ 529.5 eV, in between the PV lattice peak at lower binding energies and the mixed hydroxide peak at lower binding energies (Fig. 4.28 (e)).

In summary, the observed Fermi level shift (~1.1 eV) in valence band spectra from the PV phase to the BM phase and its subsequent reversal after redox cycling indicate a metal-insulator-metal transition during the redox process. This finding is consistent with electronic and magnetic measurements, confirming the metal-insulator transition induced by reduction processes. The core-level spectra of Co 2*p* exhibit pronounced features post-redox, suggesting the potential for full recovery of magnetization. Meanwhile, the Sr 3*d*, La 3*d*, and O 1*s* spectra show subtle peak shapes and energy shifts across redox cycles, indicative of secondary phase formation and changes in chemical environments, which might relate to the surface degradation.

#### 4.5.3.2. Comparison between HAXPES and AP-XPS data

To investigate how the non-PV surface phase that forms upon redox cycling of LSCO reacts under a thermal reduction treatment, *in-situ* ambient-pressure X-ray photoelectron spectroscopy (AP-XPS) is employed. This experiment was conducted and analyzed by Dr. Moritz L. Weber at Advanced Light Source (ALS), Berkeley, USA. To ensure comparability between HAXPES and AP-XPS results, we first compared the core-level features and valence band spetra observed in both experiments.

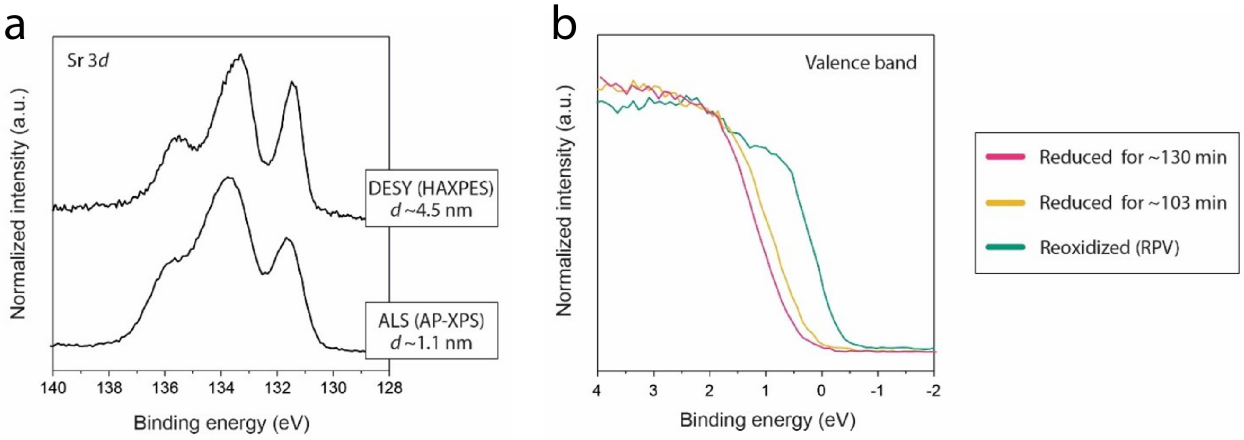


**Figure 4.29.:** a) Ex-situ HAXPES analysis and XPS (in AP-XPS chamber) analysis of LSCO in the reoxidized state ($1_{PV}$, (annealing conditions: (1) $p(Ar + 4\%\ H_2) = 1$ bar, $T = 300°C$, $t = 120$ min (2) $p(O_2) = 1$ bar, $T = 300°C$, $t = 120$ min). The spectra were normalized to the maximum intensity and are shown with an offset along the y-axis for clarity. The binding energy was aligned with respect to the respective Fermi edge. The mean escape depth for the Sr 3*d* core-level is calculated as an indicator for information depth. b) AP-XPS analysis of the valence band of $1_{PV}$-LSCO during a thermal reduction treatment (annealing conditions: $p(H_2) = 0.1$ mbar, $T = 350°C$). The valence band is normalized to BE = 2 eV.

As can be seen in Fig. 4.29, a similar signature with a dominant surface phase contribution

is detected for the $1_{PV}$-LSCO thin films after reoxidation using different beamlines yielding a different mean escape depth $d$. Note that only the Sr $3d$ signature is used for the comparison of the surface chemical information obtained at the HAXPES (Deutsches Elektronen-Synchrotron, DESY) and AP-XPS (Advanced Light Source, ALS) beamlines, since different core-levels were recorded for the analysis, e.g. lanthanum (La $3d$ versus La $4d_{5/2}$) and cobalt (Co $2p$ versus Co $3p$). The reason is a different accessibility of the core-levels depending on the applied photon energy.

The Fermi edge shifts over the course of the reducing thermal treatment indicating a metal-to-insulator transition, where a shift of ΔBE ~1.1 eV is determined at the end of the annealing. The value is equal to the value measured by HAXPES analysis (Fig. 4.28 (a)), indicating that the two experiments are comparable.

#### 4.5.3.3. Surface phase formation during BM-LSCO reoxidation

Since the AP-XPS experiment aligns comparably with the aforementioned HAXPES experiment, we have structured a series of AP-XPS experiments to investigate the surface chemistry of LSCO during the phase transition from the PV to the BM phase. The measurements were conducted with enhanced surface sensitivity using a photon energy of $E_{hv}$ = 680 eV, resulting in a mean escape depth ranging from $d$ = 0.5 to 1.3 nm for various core-level spectra and the valence band. This setup enabled the investigation of surface chemical and electronic changes during a reducing annealing treatment at elevated temperatures. An LSCO sample underwent reduction and subsequent reoxidation through ex-situ annealing in a furnace under conditions identical to those used for the HAXPES samples (annealing conditions: (1) $p(\mathrm{Ar} + 4\%\mathrm{H_2})$ = 1 bar, $T$ = 300°C, $t$ = 120 min, (2) $p(\mathrm{O_2})$ = 1 bar, $T$ = 300°C, $t$ = 120 min) before transfer into the AP-XPS chamber. Comparison of Sr $3d$ spectra obtained from the as-transferred samples (cf. Fig. 4.29 (a)) with those from the $1_{PV}$-LSCO sample investigated by HAXPES and AP-XPS indicates comparable surface chemistry. Thus, we confirm that the starting point of the AP-XPS analysis aligns with the final redox state investigated by HAXPES (cf. Fig. 4.28).

Following mild thermal oxidation of the as-transferred, air-exposed sample to remove adventitious carbon from the surface ($p(\mathrm{O_2})$ = 0.1 mbar, $T$ = 350°C, $t$ = 15 min), Sr $3d$, La $4d$, Co $3p$, and O $1s$ core-level spectra were recorded during a thermal reduction treatment ($p(\mathrm{H_2})$ = 0.1 mbar, $T$ = 350°C, $t$ = 130 min), allowing for *time-resolved* monitoring of spectral changes under conditions comparable to those applied in the ex-situ experiments discussed above. A systematic shift in binding energy (BE) was observed for all core-level spectra throughout the thermal reduction treatment relative to the BE recorded after mild oxidation (Fig. 4.30 (a) and (b)). The arrows in Fig. 4.30 (a) indicate the peak position changes from the initial state (bottom) to the final annealing state (top). The magnitude of this total shift ΔBE varied among the different core-levels, with the Co $3d$~0.2 eV core-level showing a smaller shift, suggesting a complex interplay of chemical and electrostatic factors influencing the shifts.

The evolution of the relative peak area ratio of A-site to B-site cations is depicted in Fig. 4.30 (c)

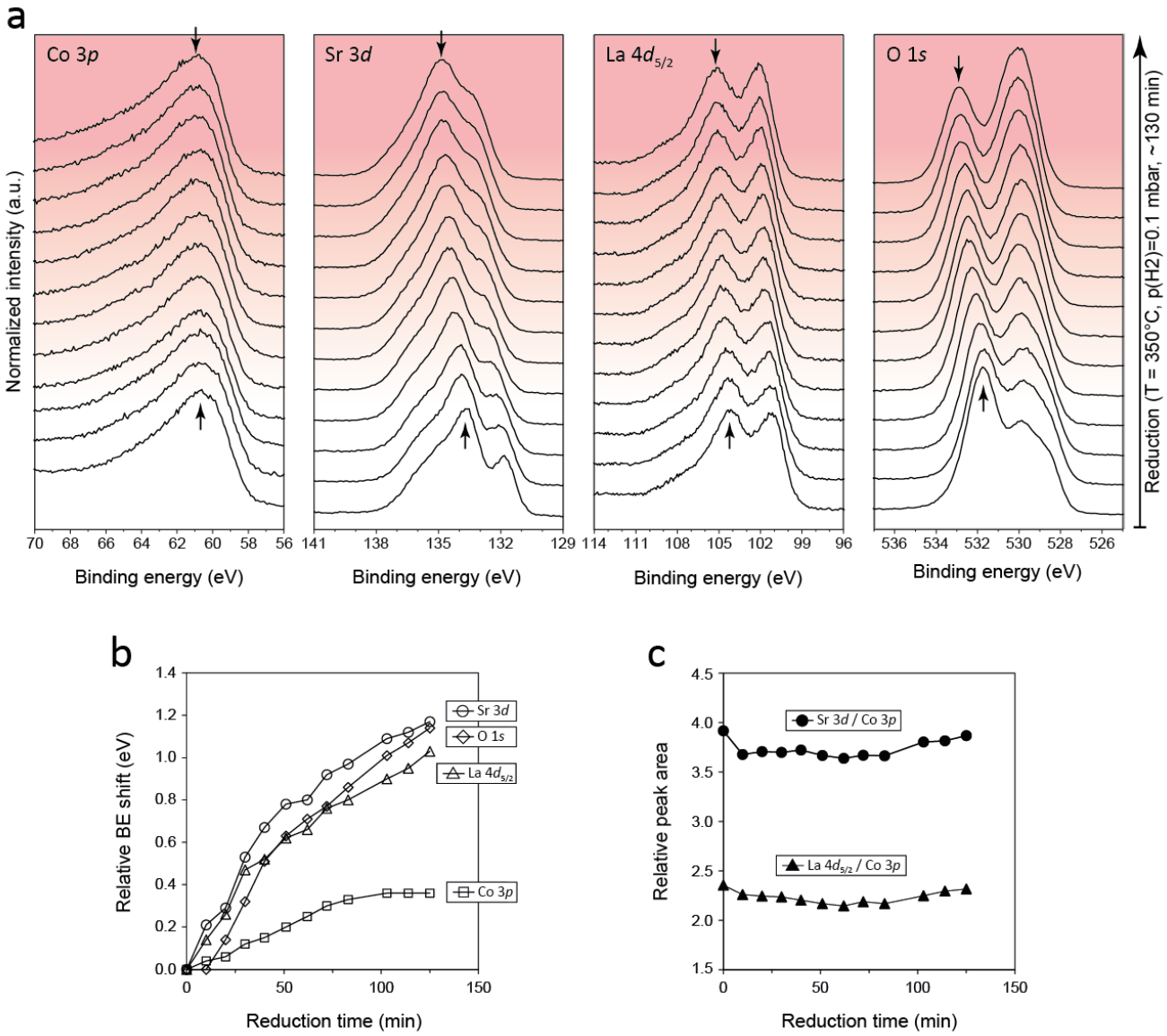


**Figure 4.30.:** *in-situ* AP-XPS analysis of $1_{PV}$-LSCO during thermal reduction (BM, annealing conditions: $p(H_2) = 0.1$ mbar, $T = 350°C$). (a) Core-level spectra obtained from the sample over reduction time. The initial state at the bottom shows $1_{PV}$-LSCO after mild oxidation to remove adventitious carbon. The spectra were normalized to the prepeak region, respectively and an offset is applied along the y-axis to improve clarity. The binding energy was alignment to the Fermi-edge obtained from the sample after mild oxidation (fixed vale) while no individual alignment was applied in order to observe the monotonous BE shift as a result of the thermal reduction. (b) Plot of the BE shift relative to the initial state. The shift was read out at the initial intensity maximum of each spectrum. Arrows in (a) denote the initial and final position of the intensity maxima. (c) Relative peak area ratios as indicator for the A-site to B-site cation stoichiometry over reduction time indicating no considerable stoichiometric changes.

as an indicator of surface stoichiometry. Notably, during the thermal reduction step, no significant changes in surface stoichiometry are observed. This suggests that the surface phase formed during the initial reoxidation of the BM-LSCO phase remains predominantly inert under subsequent thermal reduction cycles. However, analysis of the Sr 3*d* and O 1*s* spectra reveals detectable changes in surface chemistry, with subtle alterations also apparent in the La

$4d$ core-level spectrum. These observations indicate a partial response of the surface to the reducing thermal treatment.

### 4.5.4. Discussion of reversibility and degradation of the PV-BM phase transition upon repeated cycling

The topotactic phase transition between the PV and BM phases in LSCO thin films exhibits remarkable reversibility over multiple cycles, with the saturation magnetization and room-temperature metallic state exhibiting up to 20 cycles of reversibility. However, while magnetic properties fully restore between phases, electronic and structural properties only show partial recovery. This full recovery in magnetic properties can be attributed to reversible changes in cobalt oxidation states, as depicted in Fig. 4.28 (b), where cobalt transitions from a higher to a lower oxidation state and reverts to its original high oxidation state during the PV-to-BM transition and its subsequent reoxidation back to PV (PV-BM-PV phase transition). Given that the ferromagnetism of LSCO arises from double exchange involving $Co^{3+}$ and $Co^{4+}$, the recovery of the Co oxidation state plays a crucial role in preserving ferromagnetism after reoxidation. Consequently, even after 20 cycles, the PV to BM transition of LSCO thin films maintains its ferromagnetic-to-non-ferromagnetic transition.

However, the reoxidation process from BM-LSCO to PV-LSCO introduces changes in surface chemistry, as observed in the HAXPES and *in-situ* AP-XPS analyses, affecting both the structural and electrical properties of LSCO. On one hand, the formation of an A-site rich surface state leads to decreased structural coherence in LSCO, as illustrated in Fig. 4.25, resulting in intensity changes of both BM and PV peaks compared to their original states. On the other hand, the formation of such a surface state also influences the electronic properties. The emergence of new chemical components, such as A-site rich phases typically associated with insulating behavior, can lead to additional scattering of charge carriers, potentially affecting the transport properties along the field. Thus, while the thin film retains its metal-insulator transition from PV to BM structure, the $R$ vs. $T$ curves do not entirely overlap, and room temperature resistance varies across different cycles.

In summary, the reversible phase transition behavior and the influence of surface chemistry on the electronic and structural properties of LSCO thin films highlight the complexity of their behavior under cycling conditions. While the bulk of the film shows remarkable reversibility and stability, as evidenced by XRD and SQUID data, XPS analysis reveals a different scenario at the surface. The surface appears to undergo not a reversible transition but a chemical instability, manifesting as changes already in the first redox cycle. This distinction provides a comprehensive view of the material's behavior under cycling conditions, emphasizing the need for further investigation into the underlying mechanisms. Such insights are crucial for optimizing the performance and stability of LSCO-based devices and complex oxides in diverse applications.

## 4.6. Exploring the phase transition dynamics in LSCO thin films

In the previous chapter, we explored the reversibility of the topotactic phase transition within LSCO thin films. However, understanding the intricate interplay of ionic responses and the associated oxygen diffusion and surface exchange processes during this transition is crucial to characterize the intrinsic nature of the topotactic phase transition. Hence, this chapter aims to investigate deeper the dynamics of this transition, focusing particularly on the oxygen ion diffusion and surface exchange mechanisms.

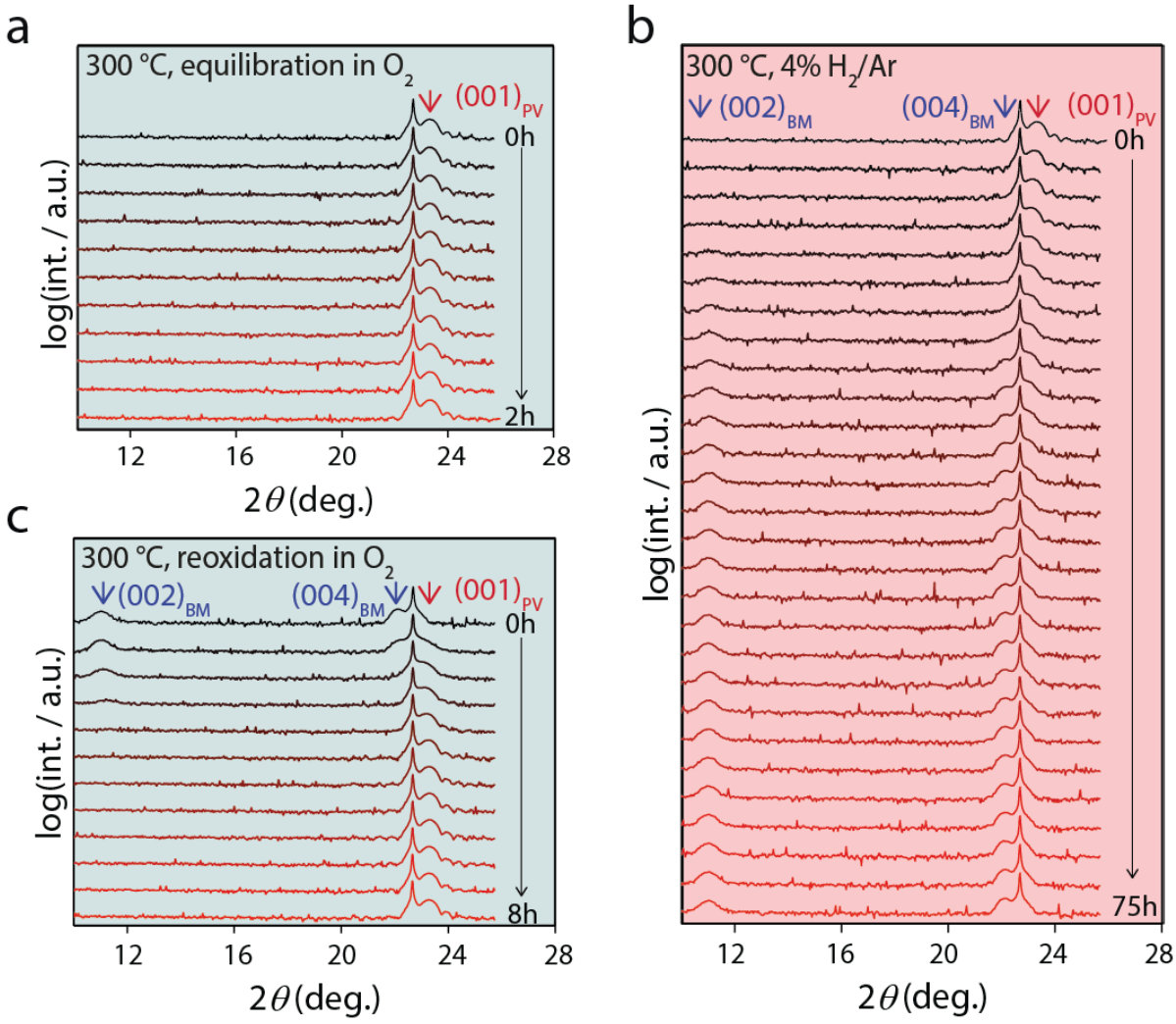


**Figure 4.31.:** *in-situ* XRD was used to monitor the topotactic phase transition. The experiment consisted of three steps: a) Stabilizing the sample in an oxygen atmosphere for two hours. b) Annealing the sample in Ar+4%$H_2$ for 75 hours to trigger the PV to BM phase transition. c) Reoxidizing the sample back to the PV structure by annealing the sample for 8 hours in an oxygen environment.

For this, we utilized *in-situ* XRD to monitor the topotactic phase transition PV-BM-PV across various temperature settings. The details of the experimental setup can be found in the experimental section. Fig. 4.31 illustrates the *in-situ* XRD experiment conducted within a scan range of 10° to 28° at a temperature of 300°C. Initially, the sample was placed in an $O_2$ atmo-

sphere for 2 hours to equilibrate in oxidizing conditions at a given temperature, as depicted in Fig. 4.31 (a), showing an unchanged position of the PV $(001)_{PV}$ peak at 23.3°. Subsequently, the gas flow was switched to Ar+4%$H_2$ to induce the reducing atmosphere necessary for triggering the phase transition into the BM phase, as described in the previous chapters. As shown in Fig. 4.31 (b), during annealing in an Ar+4%$H_2$ atmosphere, the PV structural peak, denoted as $(001)_{PV}$, gradually shifted to lower angles until it disappeared entirely. Simultaneously, the characteristic BM structural peaks, $(002)_{BM}$ and $(004)_{BM}$, emerged gradually until their intensities stabilized, requiring approximately 48 hours in total at 300°C. This observation aligns with previous studies indicating the gradual disappearance of PV structural peaks and the concurrent growth of BM structural peaks until the BM structure stabilizes.

Subsequently, we initiated the reoxidation experiment by reverting the gas flow to an $O_2$ environment, triggering the phase transition from BM back to PV. During this transition, we observed a gradual disappearance of the BM peaks, specifically the (002)BM and (004)BM, as the structure reverted. Concurrently, the (001)PV peak re-emerged, regaining both its position and intensity characteristic of the perovskite phase. By conducting such PV-BM-PV transitions at various temperatures, we collected characteristic times for the stabilization of $(001)_{PV}$, $(002)_{BM}$, and $(004)_{BM}$ peaks, which are associated with their respective positions and intensities. To comprehensively investigate the topotactic phase transition of PV-BM-PV, we utilized *in-situ* XRD techniques on the same sample across a temperature range from 270°C to 400°C, following identical measurement steps (initial heating to the target temperature, oxidation in $O_2$ atmosphere for 2 hours, subsequent reduction in Ar+4%$H_2$ for 75 hours, and reoxidation in an $O_2$ environment for 8 hours). This enabled us to correlate the characteristic time scale of the phase transition with the intensity and lattice constant of $(002)_{BM}$ and $(001)_{PV}$ peaks, as presented in Fig. 4.32 (a) and (b).

Fig. 4.32 (a) summarizes the relative intensity changes with respect to the oxidized state of the $(002)_{BM}$ and $(001)_{PV}$ peaks over time when switching the atmosphere from $O_2$ to Ar+4%$H_2$ and back to $O_2$. Initially, in the first 2 hours of the oxidation process, the $(002)_{BM}$ peak exhibits zero intensity, while the $(001)_{PV}$ peak reaches its normalized maximum intensity, indicating the presence of the pure PV structure in the as-oxidized sample. Upon switching to Ar+4%$H_2$, the intensity of the BM peaks gradually increases, and meanwhile, the intensity of the PV peak decreases simultaneously. At higher temperatures, the BM peak intensity grows more rapidly and the PV peak intensity decreases more quickly until it reaches zero. This behavior is attributed to the higher temperatures, which increase the attempt frequency of oxygen ions to overcome energy barriers. This enhanced attempt frequency facilitates the surface exchange process necessary for the phase transition, as oxygen ions more readily acquire the activation energy required to transition through the barrier. Over the course of 75 hours, both the BM and PV phases reach stable values, indicating equilibrium. The gas flow is then switched back to $O_2$ to initiate reoxidation. We observe a significant asymmetry in the phase transition rates between oxidation and reduction conditions. Specifically, at 300°C under reducing conditions, the PV to BM phase transition required 45.5 hours, whereas the reverse BM to PV transition

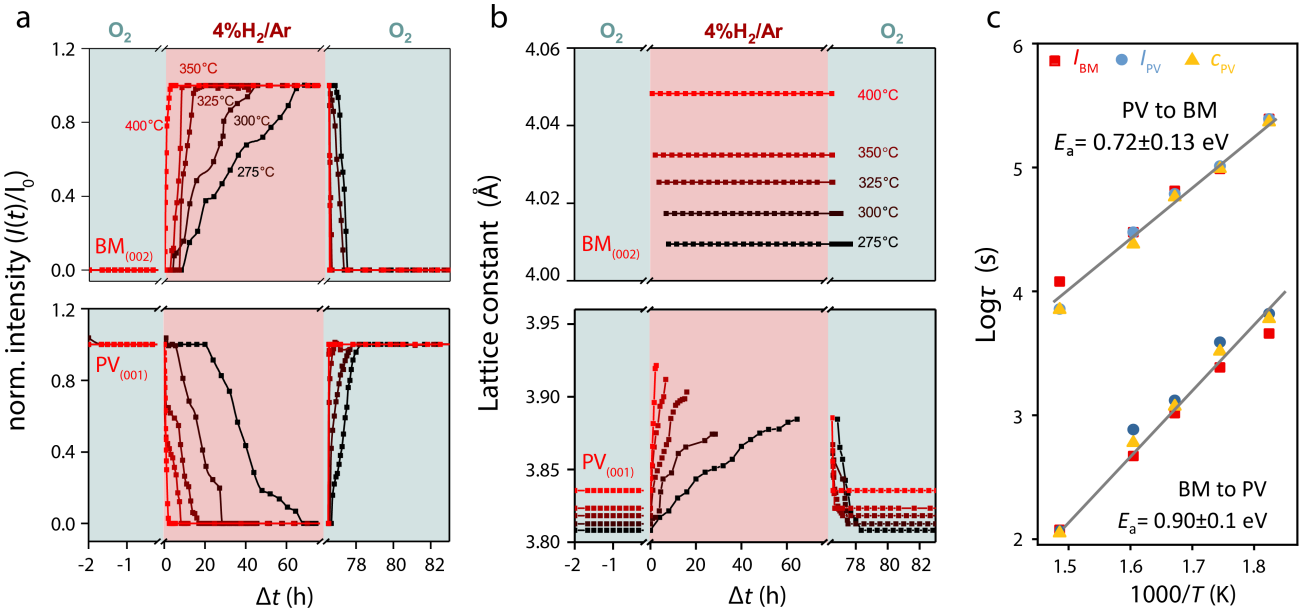


**Figure 4.32.:** a) The normalized intensity of $(002)_{BM}$ and $(001)_{PV}$ peaks under different annealing conditions and times. b) The lattice constants based on the $(002)_{BM}$ and $(001)_{PV}$ peaks under different annealing conditions and times. c) Utilizing the Arrhenius plot to calculate the activation energy of the PV to BM and BM to PV phase transitions.

occurred much faster, completing in only 0.83 hours. Quantitatively, the BM to PV transition is approximately 55 times faster than the PV to BM transition under these conditions. This marked difference underscores the asymmetric kinetics of the phase transition process.

The lattice constant related to the PV and BM peak positions is shown in Fig. 4.32 (b). It is evident that during the initial 2 hours of oxidation, the lattice constant of the PV structure remains unchanged. However, as the temperature increases, there is a noticeable increase in the out-of-plane lattice constant, attributed to thermal expansion. Upon switching the atmosphere to Ar+4%$H_2$, the lattice constant of the PV phase progressively increases until the peak position becomes indistinguishable. In contrast, the behaviour of the BM peaks is different. They initially emerge with a fixed lattice constant, which remains constant throughout the annealing process. However, at higher annealing temperatures, the lattice constant of the BM phase increases consistently with the thermal expansion of the lattice. Upon reverting to an $O_2$ environment, a reverse phenomenon occurs: the intensity of the BM phase gradually diminishes, with higher temperatures leading to a faster decrease. The lattice constant of the PV phase initially starts with a larger value but then stabilizes back to its original value, indicating that the phase transition appears to be fully reversible in the XRD experiment. As the temperature increases, this stabilization becomes more thermally activated. The characteristic relaxation time of the phase transition is determined by (1) the disappearance of the PV phase lattice constant, (2) the disappearance of the BM peak intensity, or (3) the point at which the lattice constant curve of the PV phase becomes flat, reaching its stable value.

It is evident that higher temperatures accelerate the structural phase transition, whereas lower temperatures necessitate longer annealing times for completion of this process. The rate of the phase transition is therefore correlated with a characteristic relaxation time ($\tau$), which is inversely proportional to the reaction rate. The characteristic relaxation time is determined as the point where the intensity change curve becomes flat and hence reaches equilibrium, reaching its normalized maximum or minimum for the normalized intensity (Fig. 4.32 (a)). Alternatively, it is determined when the PV phase lattice constant disappears or when the lattice constant curve becomes flat, indicating it has reached a stable value (Fig. 4.32 (b)). By establishing relaxation times at various temperatures, an Arrhenius plot can be constructed. The Arrhenius equation, provided below (Equation 4.1), describes the temperature-dependent behaviour of the reaction rate $k$. As the characteristic time is inversely proportional to $k$, we have:

$$\frac{1}{\tau} \sim k = A \cdot e^{-\frac{E_A}{k_B \cdot T}} \tag{4.1}$$

where $k$ represents the reaction rate, $A$ is the pre-exponential factor, $E_\mathrm{A}$ denotes the activation energy, $k_\mathrm{B}$ is the Boltzmann constant, and $T$ the temperature. Fig. 4.32 (c) shows the Arrhenius plot in its logarithmic form as given by Equation 4.2:

$$\log(\tau) \sim -\log(k) = -\log(A) + \frac{E_\mathrm{A}}{2.303 \cdot k_\mathrm{B} \cdot T} + N \tag{4.2}$$

where $N$ is a constant. we use the characteristic relaxation time of the BM peak intensity ($I_\mathrm{BM}$), the PV peak intensity ($I_\mathrm{PV}$), and the lattice constant change of the PV phase ($C_\mathrm{PV}$) to analyze the activation energy from PV to BM and vice versa. The observed linear relationship suggests that a temperature-activated process governs the structural changes in the lattice. Consequently, the activation energy can be determined by analyzing the slope of the Arrhenius plot using experimentally obtained data. We perform a linear fit of all three sets of data ($I_\mathrm{BM}$, $I_\mathrm{PV}$, and $c_\mathrm{PV}$) together on a single plot. This unified approach shows that all three parameters independently fall on a single straight line, as illustrated in Fig. 4.32 (a), indicating the reliability of the analysis. From the simultaneous fit of the three data sets, we obtain an activation energy of $0.72 \pm 0.13$ eV for the PV to BM phase transition and $0.90 \pm 0.1$ eV for the BM to PV transition, with the error bars reflecting the fitting error of the experimental data.

To assign the physical processes underlying this activation energy, we analyze the intermediate reaction steps involved in the phase transition. As illustrated in Fig. 4.33 (a), the phase transition comprises three distinct processes:

1. **Ionic diffusion:** In this process, oxygen ions migrate from the interior of the thin film toward the surface.

2. **Oxygen surface exchange:** Here, oxygen ions at the material's surface undergo a redox exchange, where pairs of oxygen ions combine to form oxygen molecules, involving the

transfer of charge from the oxygen ions to the surrounding environment.

3. **Nucleation of the BM phase:** This step involves the formation of nuclei or clusters of the BM phase within the PV phase matrix. This occurs once a critical concentration of oxygen vacancies has been generated through steps 1 and 2, facilitating the transition to the BM phase. [90]

All three processes generally exhibit Arrhenius-type thermal activation, which complicates the overall reaction kinetics. Due to their exponential nature, each process typically has its own characteristic time constant, which can vary significantly. As a result, the experimentally determined activation energy corresponds to the slowest (rate-limiting) timescale.

Based on literature in solid-state ionics, independent studies have determined the activation energies for oxygen diffusion and surface exchange processes. The reference activation energies for these processes in LSCO are as follows: Oxygen diffusion ($D^*$) is approximately 2 eV, while oxygen surface exchange ($K^*$) ranges from 0.7 eV to 1 eV [152–155]. The activation energies of surface exchange and nucleation are reported to be similar. Specifically, the nucleation of new phases requires specific activation energies: approximately 0.65 eV for the BM phase and 1.11 eV for the PV phase in comparable Co-based perovskite oxides, observed at temperatures above 573 K [90].

By comparing with the calculated activation energy for LSCO, we find it closely matches that of oxygen surface exchange or possibly BM/PV phase nucleation. Thus, either oxygen surface exchange or nucleation of the new phase likely governs the rate-limiting process.

To further investigate the rate-limited process, we conducted a study to accelerate the oxygen surface exchange using the noble metal platinum (Pt). As documented in the literature [156, 157], Pt acts as a catalyst, facilitating the transformation of oxygen ions into oxygen molecules through the following chemical reaction:

$$\mathrm{O_O^x} \rightarrow \frac{1}{2}\mathrm{O_2(g)} + \mathrm{V_O^{\bullet\bullet}} + 2\mathrm{e'} \tag{4.3}$$

where $\mathrm{O_O^x}$ represents oxygen ions in the lattice of the thin film, $2\mathrm{e'}$ represents the two electrons filled to the Pt, and $\mathrm{V_O^{\bullet\bullet}}$ denotes oxygen vacancies formed in the oxide. This acceleration enhances the dynamics of the surface exchange without affecting oxygen diffusion and nucleation in the PV/BM phase. We utilized this method to observe if the phase transition is significantly accelerated when Pt is present on the film. For this purpose, we sputtered a 50 nm thick Pt layer onto the four corners of the as-grown LSCO thin film. Subsequently, the sample underwent annealing in an Ar+4%$H_2$ atmosphere at 200°C for 30 minutes to visually monitor the phase transition. As depicted in Fig. 4.33 (b), the four corners of the sample were coated with Pt, while the remaining areas remained uncoated. After the annealing process, we observed partial transparency within the yellow delineation, whereas the rest of the sample retained its metallic dark color. This gradient arises from the localized catalytic effect of Pt, which accelerates the

oxygen surface exchange and leads to an increase in oxygen vacancy concentration close to the Pt electrodes. Consequently, a metal-insulator transition occurs, resulting in the transparent appearance of the sample. Conversely, the regions far away from the catalytic Pt-coated areas maintain their original metallic properties and retain their metallic dark color.

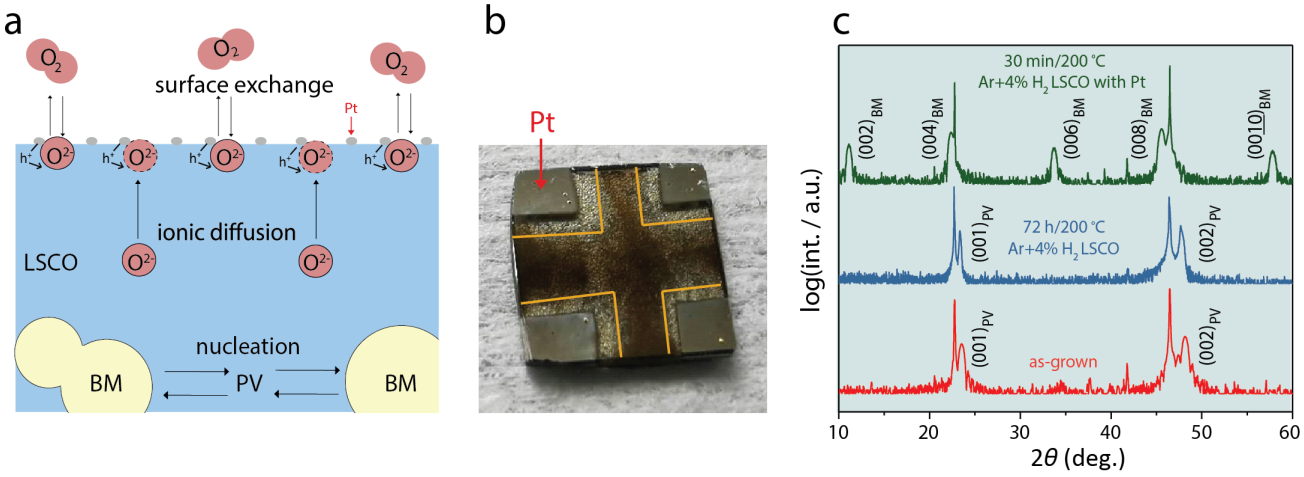


**Figure 4.33.:** a) The three distinct processes involved in the topotactic phase transition, along with the Pt catalysis phenomenon. b) A visual illustration of the phase transition achieved by sputtering Pt on the four corners of the sample. c) A comparison of the time scales of the phase transition with and without accelerating the surface exchange (with Pt and without Pt).

Furthermore, to extend this phenomenon to the entire film, we sputtered a nominal 2 nm Pt layer onto the surface of the as-grown film. Initially, we use an as-grown LSCO film without Pt as a reference. After annealing the film without Pt in an Ar+4%$H_2$ atmosphere at 200°C for 72 hours, we observe only a slight shift of the $(001)_{PV}$ and $(002)_{PV}$ peaks to lower angles. However, the sample retained its perovskite structure, as depicted by the blue curve in Fig. 4.33 (c). This suggests that the phase transition is not achieved after 72 hours of annealing at 200°C, and this process requires an extremely long time under these conditions.

The same treatment was applied to the sample with a 2 nm Pt layer. Surprisingly, after annealing at 200°C for half an hour, the sample completely transitioned to the BM phase, indicating a significant acceleration of the phase transition. This acceleration occurred at the triple-phase boundary where the Pt, the LSCO, and the $H_2$ gas meet. At this boundary, the Pt donates two holes or takes up two electrons to the oxygen ions within the film (see Fig. 4.33 (a)), facilitating the formation of oxygen molecules. Thus, the surface exchange process is greatly accelerated. Accelerating this surface exchange process can hence significantly assist the topotactic phase transition from PV to BM. This catalytic effect of Pt suggests that similar catalysts or surface activation methods could potentially accelerate the phase transition in LSCO or similar oxide materials [156, 157].

Moreover, the acceleration of the surface exchange process implies that it could represent the rate-limiting step of the topotactic phase transition from PV to BM. This finding is consistent with previous studies on the activation energy of the phase transition, which suggested that

overcoming the energy barrier associated with surface oxygen exchange is critical for the phase transition.

From the perspective of oxygen vacancy distribution during the transition, if the process is predominantly limited by surface exchange, it implies a more homogeneous distribution of oxygen vacancies across the thin film. This uniformity supports the validity of XRD analysis, which is sensitive to bulk properties. The consistency in XRD results further suggests that the phase transition observed reflects the true bulk transformation rather than being influenced solely by surface effects.

In conclusion, the ability to manipulate the phase transition kinetics through surface catalysis highlights a pathway for controlling the properties of LSCO thin films and potentially other complex oxides. Exploring alternative catalysts such as Ag, Pd, and Rh, or employing surface activation strategies, could further enhance our ability to tailor these materials for specific applications.

## 4.7. Towards topotactic phase transitions in LSCO free-standing membranes

In the previous chapters, it has been described that LSCO thin films show a large structural flexibility between PV and BM phase and how it can be controlled. This property holds potential for applications. However, the presence of a substrate can introduce several detrimental effects, negatively impacting the performance and functionality of the thin films [158, 159]. Additionally, oxide epitaxy is generally not compatible with CMOS (semiconductor) processes. Therefore, delamination and transfer techniques could potentially enable the integration of functional oxides such as LSCO with semiconductor chips in the future [160]. To avoid substrate-related effects the fabrication of free-standing LSCO membranes might be a possible route. This chapter presents a preliminary exploration of the properties of the free-standing LSCO membranes. Further studies are currently in progress and are outside the scope of this thesis.

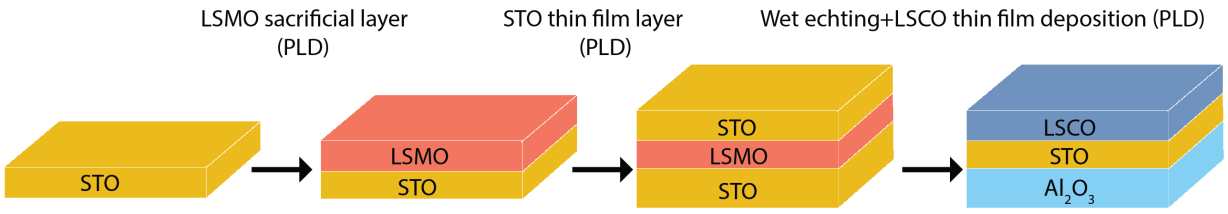


**Figure 4.34.:** Illustration of the wet-etching process used to fabricate the free-standing STO+LSCO membrane. The free-standing LSCO membrane was fabricated by Marcus Wohlgemuth and Anton Kaus from PGI-7, Forschungszentrum Jülich GmbH.

The free-standing LSCO membranes were fabricated by Marcus Wohlgemuth and Anton Kaus from PGI-7, Forschungszentrum Jülich GmbH, using a wet etching method. Specifically, Marcus Wohlgemuth developed the necessary processes at PGI-7 to enable the synthesis of a quasi-free-standing double layer. This method will be elaborated in detail in Marcus Wohlgemuth's PhD thesis (in preparation). As illustrated in Fig. 4.34, the fabrication process involved the following steps:

1. Initially, a 10 nm thick $La_{0.7}Sr_{0.3}MnO_3$ (LSMO) sacrificial layer was grown on the STO substrate using PLD.
2. Subsequently, a 20 nm thick STO layer was deposited on top of the LSMO layer.
3. The wet-etching method was then employed to selectively dissolve the LSMO sacrificial layer, detaching the STO thin film from the substrate.
4. The free-standing STO layer was transferred onto a sapphire substrate, where it is weakly bonded.

5. Finally, a 20 nm thick LSCO thin film was deposited on the free-standing STO layer.

This process successfully fabricated a coherent, single-crystalline double-layer STO/LSCO on an arbitrary substrate, which has no structural relationship to the thin film.

Fig. 4.35 (b) shows the XRR of the STO membrane before and after LSCO growth. Initially, the XRR pattern of the STO membrane displays a single type of oscillation. After the LSCO layer is added, a second type of oscillation appears in the STO/LSCO bilayer. This outcome is consistent with the expected physical properties of the membrane and indicates a high-quality surface structure, as demonstrated by XRR, which requires a good crystallinity and surface morphology. The surface morphology of the STO membrane, both before and after LSCO growth, is depicted in Fig. 4.35 (b). It shows that the surface remains flat with visible step terraces throughout the process. Remarkably, the free-standing LSCO/STO bilayer maintains a smooth surface with clear step terraces, demonstrating structural coherence at the microscopic level. This uniformity suggests that the epitaxial relationship and lattice matching between the LSCO layer and the substrate are well preserved. Furthermore, the RSM image of the STO/LSCO membrane is presented in Fig. 4.35 (c). The LSCO layer exhibits a similar in-plane lattice constant as the STO layer due to the interface strain and has an out-of-plane lattice constant of approximately 3.76 Å, consistent with the LSCO thin film discussed in Section 4.4.1. These data suggest that the fabrication process effectively minimizes stress and deformation, which are critical for maintaining the functional properties of the membrane in potential applications.

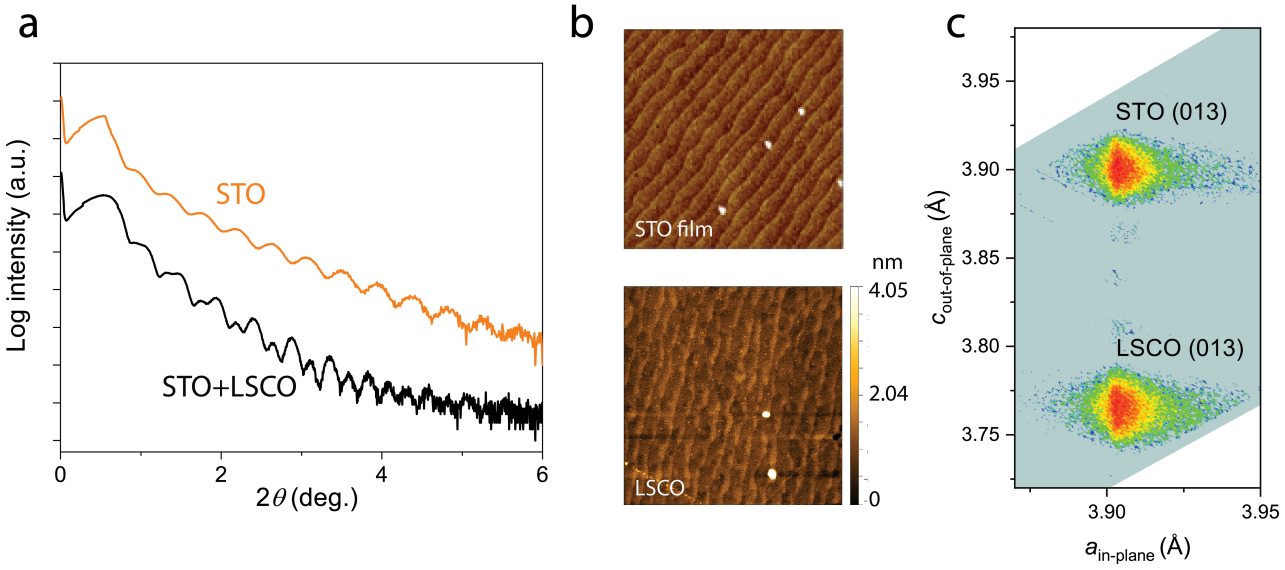


**Figure 4.35.:** a) XRR data of the STO and STO+LSCO membranes. b) AFM scans of the STO and LSCO membrane. c) RSM scan of the STO+LSCO membrane. Data is provided by Marcus Wohlgemuth and Anton Kaus.

The successful fabrication of the high-quality STO/LSCO membrane is particularly interesting concerning its functionality associated with the PV to BM phase transition. To induce this

phase transition, we applied the same conditions as described in Section 4.4: annealing at $10^{-6}$ mbar and 450°C for 2 hours in the JCNS-2 vacuum chamber. As illustrated in Fig. 4.36, the black curve depicts the XRD data of the as-grown STO/LSCO membrane. The stars denote the corresponding STO (001) to (004) peaks, while $S_{(1-102)}$, $S_{(2-204)}$, and $S_{(3-306)}$ represent the related sapphire substrate peaks. $(001)_{PV}$ to $(004)_{PV}$ signify the LSCO peaks. Peaks indicated by solid dots are still under discussion. From the XRD data, it is evident that the as-grown membrane exhibits coherent crystallinity, as indicated by consistent peaks over a broad range of angles and thickness oscillations shown in the zoomed-in graph (Fig. 4.36(b)). The LSCO peaks are observed to the right of the STO peaks, consistent with the LSCO thin film lattice parameter discussed in Section 4.4. Subsequent to 2 hours of annealing at $10^{-6}$ mbar and 450°C, the sample undergoes a transition to the BM structure, as evidenced by additional peaks, $(002)_{BM}$ to $(00\underline{16})_{BM}$, depicted in the red curve. The $(002)_{BM}$ peak is observed at 11.1°, aligning with the corresponding $(002)_{BM}$ peak position in the BM phase LSCO thin film, indicating similarity in lattice constant and structure between the BM phase membrane and the thin film. For a clearer observation of possible changes of peak positions and shapes Fig. 4.36(b) provides an enlarged view from 20° to 28°. In this view, the STO peak remains nearly unchanged in angle, demonstrating the structural stability of the STO layer at the annealing temperature. Meanwhile, the LSCO perovskite $(001)_{PV}$ peak vanishes after annealing, and the $(004)_{BM}$ peak emerges at the same position as the STO (001) peak, consequently broadening the STO (001) peak. Based on this XRD data, it is evident that the STO/LSCO membrane can undergo a structural phase transition from PV to BM, affirming its functionality in this regard.

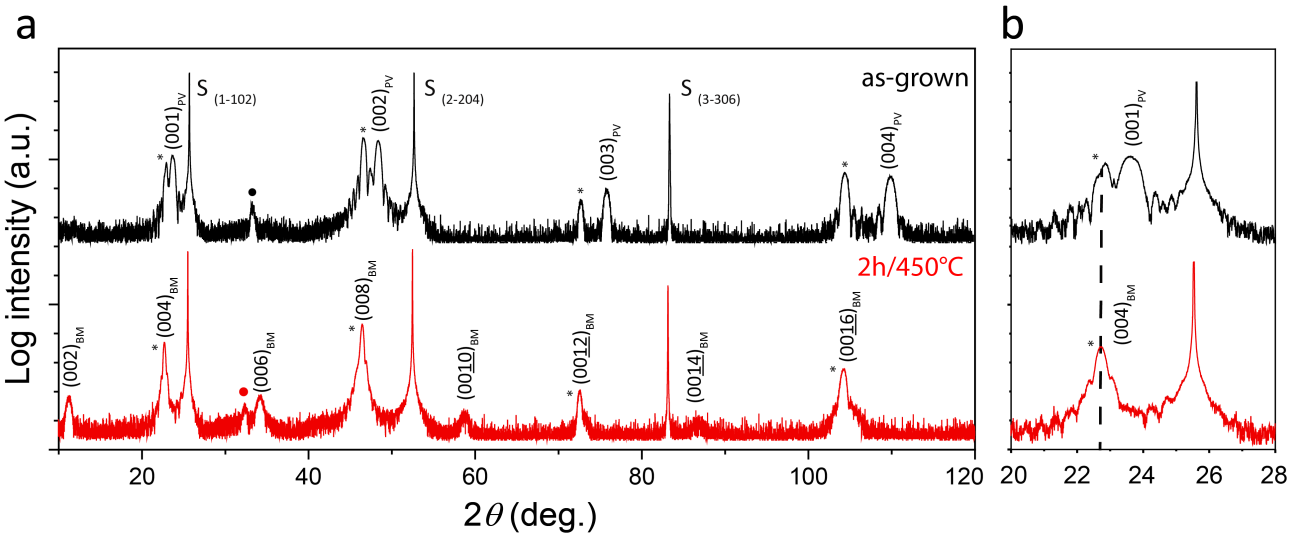


**Figure 4.36.:** a) XRD data of the full scan for the as-grown and 2h/450°C annealed films. b) Zoom-in view of the XRD data from (a) in the range of 20°to 28°.

To investigate the correlation between magnetic properties and the structural phase transition for this transferred double-layer sample, we employed SQUID-magnetometry to examine the magnetic characteristics of the STO/LSCO membrane before and after the phase transition. As depicted in Fig. 4.37, the as-grown STO/LSCO membrane demonstrates ferromagnetic

behaviour, with a critical temperature close to 175 K—similar to the value observed in the thin film, which is at ca. 180 K. At 300 K, no hysteresis can be observed in the field sweep. However, at 120 K and 5 K, an open hysteresis is evident, with saturation magnetization values of 1 $\mu_B$/Co and 1.5 $\mu_B$/Co, respectively. Remarkably, these values correspond to those obtained from the thin film measurements. Following a 2-hour annealing process at 450°C, as indicated by the red curve in Fig. 4.37 (a), the membrane no longer exhibits ferromagnetism. The saturation magnetization of the membrane decreases to approximately 0.25 $\mu_B$/Co at 300 K, 120 K, and 5 K, as observed by the field sweep in Fig. 4.37 (b) to (d). At room temperature, the saturation magnetization becomes non negligible. This non-zero magnetization persists even at the a low temperature of 5 K. This may be attributed to the complex Co valence states in LSCO. It is possible that there are still sufficient $Co^{3+}$ and $Co^{4+}$ ions to facilitate double exchange, supporting weak ferromagnetism. Alternatively, $Co^{3+}$ ions may engage in a special case of superexchange that contributes to weak ferromagnetism but results in insulating behavior. The underlying mechanisms responsible for this behavior remain an open question.

To further correlate the magnetic and structural properties of the STO/LSCO membrane during the phase transition, we conducted PNR measurements with *in-situ* annealing. Initially, the as-grown membrane was cooled down to 120 K under vacuum conditions ($10^{-6}$ mbar) for PNR measurements with both the neutron beam spin-up and spin-down channels. Subsequently, we applied the same annealing conditions depicted in Fig. 4.36 (450°C for 2 hours) to increase the oxygen vacancy concentration. The results of these measurements are shown in Fig. 4.38 (a). Notably, clear thickness oscillations are observed in both the as-grown and annealed membranes, indicating the sample's sufficiently smooth surface morphology. This demonstrates that the layer quality is sufficient for performing PNR measurements, as it is the first oxide membrane reported to produce a strong signal in PNR measurements. The splitting between the spin-up and spin-down channels observed in the as-grown membrane confirms its ferromagnetic behaviour, consistent with the $M$-$T$ curve in Fig. 4.37 (a). This observation is also consistent with the PNR data of the thin film discussed in Section 4.4. However, interestingly, for the annealed membrane, no splitting is observed between the spin-up and spin-down channels, indicating nearly zero magnetization after annealing.

A preliminary fitting was applied to these PNR data using the simplest model, i.e. Sapphire substrate + STO + LSCO + Vacuum (Vac)). This straightforward model preliminary reproduced the experimental PNR data, allowing us to extract several parameters such as $n_{SLD}$, $m_{SLD}$, and the layer thickness. From the fitting results (depicted in Fig. 4.38 (b)), we identified three distinct layers within the sample, each characterized by different $n_{SLD}$ values: notably, the sapphire substrate exhibited the largest value, while the STO layer demonstrated the lowest. Here, the critical edge is determined by the $n_{SLD}$ of the sapphire substrate, which has the highest $n_{SLD}$ among all layers. Minor changes in the $n_{SLD}$ of LSCO between the PV and BM phases resulted in only a 0.0003Å$^{-1}$ difference in the critical edge, as shown in Section 4.4.5. This corresponds to a mere 1.8% change in the critical edge value (0.0155Å$^{-1}$) of the sample. Thus, the stoichiometric changes in LSCO from PV to BM phases had little effect on the crit-

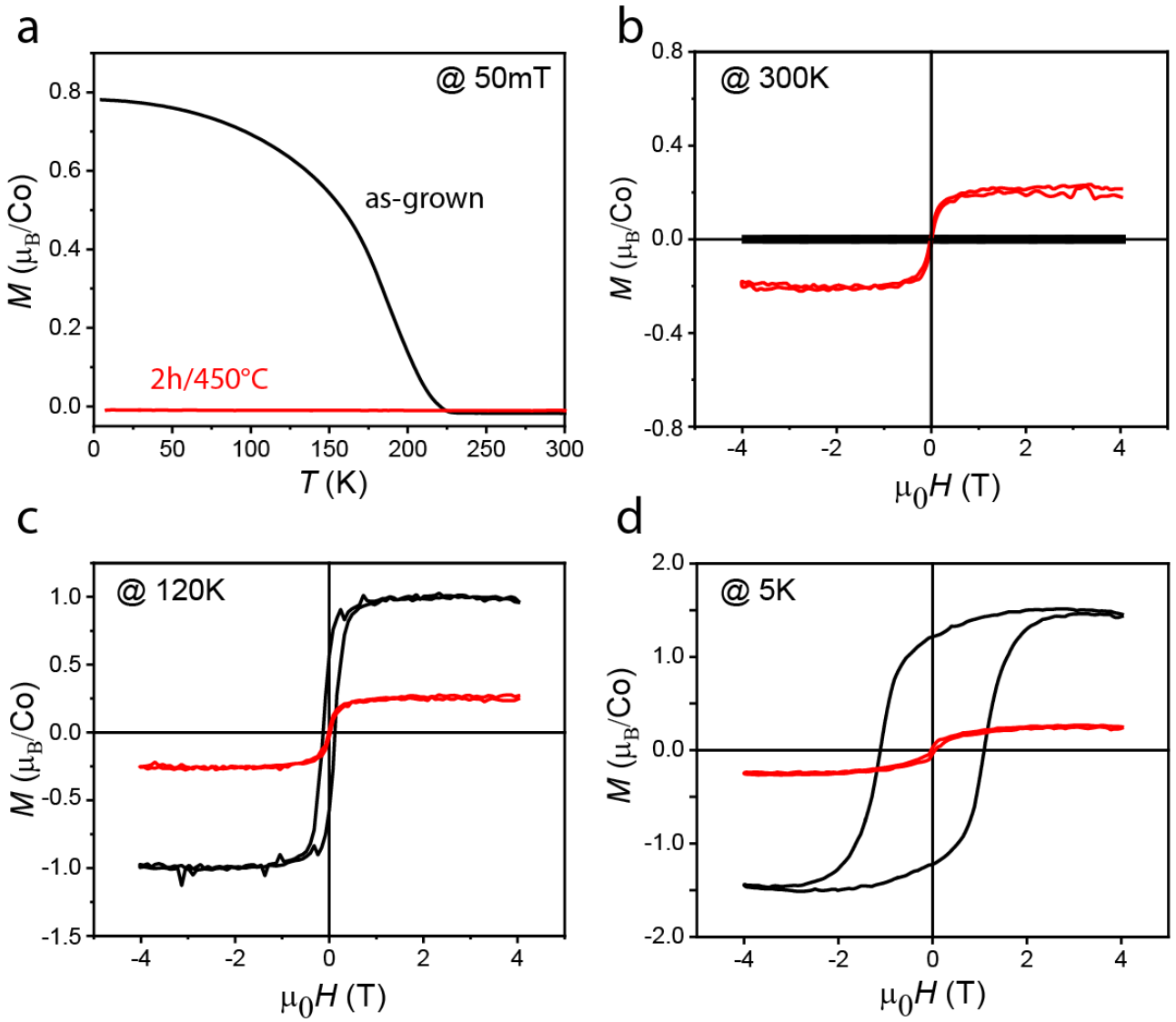


**Figure 4.37.:** a) Field-cooled curve of the as-grown and 2h/450°C annealed STO/LSCO membrane. b) Hysteresis curves of the as-grown and annealed membrane at 300 K. c) Hysteresis curves of the as-grown and annealed membrane at 120 K. d) Hysteresis curves of the as-grown and annealed membrane at 5 K.

ical edge, which is predominantly influenced by the sapphire substrate. Following annealing, the $n_{\mathrm{SLD}}$ values increased across the entire sample, a departure from the behavior observed in the LSCO thin film, where $n_{\mathrm{SLD}}$ remained unchanged for STO and decreased for LSCO. This increase may be attributed to enhanced $n_{\mathrm{SLD}}$ in the sapphire substrate after annealing, or to increased interface scattering between the membrane and substrate due to flattening of the interface post-annealing.

The thickness of the STO layer is approximately 20 nm, while the LSCO layer is approximately 17 nm, which roughly coincides with the estimated values from RHEED results. Additionally, the periodicity of the oscillation decreases after annealing, indicating that the thickness of the LSCO layer increased due to lattice expansion. This behaviour mirrors that observed in the thin film after undergoing the same annealing conditions. Regarding $m_{\mathrm{SLD}}$, the fitting results

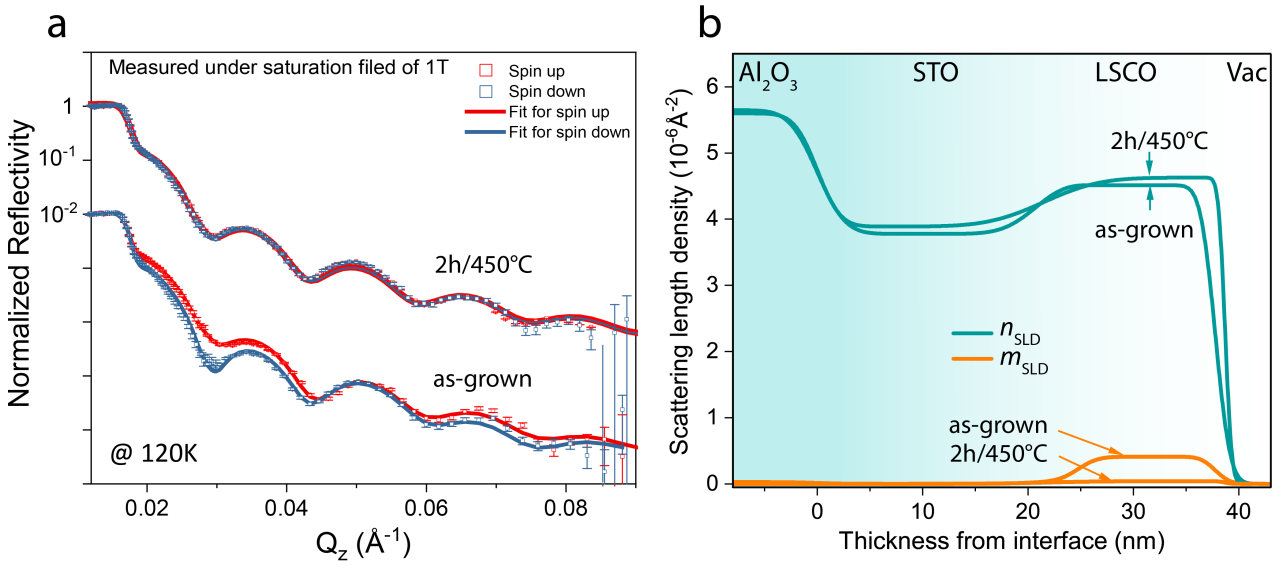


**Figure 4.38.:** a) Raw PNR data of the as-grown and annealed membrane measured at 120 K. b) Preliminary fit of the raw PNR data.

matched the raw data: the as-grown sample exhibited non-zero magnetization, specifically 1 $\mu_B$ per Co atom at 120 K (below $T_c$), consistent with the $M$-$H$ curve at 120 K (see Fig. 4.37 (c)). This value also aligns with that of the thin film discussed in Section 4.4. However, the annealed membrane showed nearly zero magnetization. The magnetization originated solely from the LSCO layer, with no magnetic signal observed from either the sapphire substrate or the STO layer. One should note that this analysis is presently only a preliminary fit of the PNR data. Several open questions remain, such as the increase of $n_{\mathrm{SLD}}$ in the annealed film and the oxygen content of the annealed film. These issues require further study in future.

The as-grown LSCO free-standing membrane exhibits a flat surface morphology with minimal defects and maintains the typical perovskite structure with ferromagnetic properties. The membrane demonstrated similar behavior to the thin film, achieving both the structural phase transition from PV to BM and the magnetic transition from ferromagnetic to non-ferromagnetic. While this research provides a promising foundation, it is preliminary, and several questions remain to be explored in future studies. For instance, the increase in $n_{\mathrm{SLD}}$ of the entire sample might be due to the sapphire substrate or the flattening of the interface structure, which requires further investigation through techniques like HR-TEM or XPS. Additionally, the extra peaks marked as solid dots in the XRD diffractogram need further study to determine their possible origins. One possibility for these additional peaks is that the LSCO might have grown directly on the sapphire substrate due to membrane imperfections or possible silver paste residue during sample growth. To investigate this, comparisons with LSCO on a sapphire thin film or detailed analysis using HR-TEM would be beneficial. Moreover, a more detailed analysis of the PNR is necessary to study additional physical parameters such as sample density, oxygen content, and the thickness of each layer.

In conclusion, while the current study has laid a solid groundwork in understanding the structural, electronic, and magnetic properties of LSCO free-standing membranes, further research is essential to fully elucidate the underlying mechanisms and to optimize the synthesis processes. Future work should focus on detailed structural analysis, improvements in fabrication techniques, and comprehensive studies of the electronic and magnetic behaviors under various conditions. This will not only enhance our fundamental understanding but also pave the way for potential applications in advanced electronic and magnetic devices.

# 5. Summary and Discussion

The aim of this thesis was to investigate the topotactic phase transition of $La_{0.6}Sr_{0.4}CoO_{3-\delta}$ (LSCO) thin films from the perovskite (PV) to the brownmillerite (BM) phase. This study specifically focuses (1) on the interplay between the structure, the electronic, and magnetic properties during the topotactic phase transition, (2) the dynamics of the transition and the rate-limiting processes involved, and (3) the reversibility of the transition along with changes in chemical composition during the topotactic phase transition. Moreover, the study was extended to free-standing LSCO membranes.

As a fundamental prerequisite in the study of ion-triggered phase transitions, the synthesis routes and resulting properties of epitaxial perovskite LSCO thin films were investigated in detail. During the synthesis of the as-grown LSCO thin film, we observed thickness-dependent variations in its structural, electronic, and magnetic properties. For thicknesses below 20 nm, the film remains crack-free and exhibits metallic behaviour, following Ohm's law: i.e. the resistance decreases with increasing thickness. Additionally, the thin film displays ferromagnetic properties, characterized by a single magnetic system. However, when the film thickness exceeds 20 nm, cracks begin to emerge. As thickness increases further, more cracks become apparent. Consequently, the sample's resistance rises due to the increased presence of cracks, which reduces the likelihood of a continuous conducting path. Beyond 40 nm, the films lack any possible conducting path, leading to insulating behavior on the macroscopic scale. Furthermore, the presence of cracks correlates with the emergence of several magnetic subsystems. For instance, a 30 nm film exhibits two magnetic subsystems, while films thicker than 30 nm reveal three subsystems. These subsystems are closely tied to the presence of cracks, existing only within cracked regions of the sample. One potential scenario is subject to Co spin-state transitions due to strain induced by lattice distortion [128, 129]. With various spin types of Co, spin transitions may occur in cracks as the strain field changes within them. This leads to the formation of new magnetic domains within these structural imperfections.

Hence, 20 nm LSCO films were primarily used to investigate the interplay among structural, electronic, and magnetic transitions. For polarized neutron reflectivity (PNR) measurements, however, 40 nm thick samples were utilized to fit the experimental requirements, particularly the ideal periodicity of the PNR signal. This approach is justified by the fact that potential magnetic subsystems do not affect the total (averaged) magnetic moment measured by PNR.

The BM phase was successfully achieved through high-temperature vacuum annealing and hydrogen-environment reduction. Both the PV and BM phases exhibit atomically flat surfaces

and distinct phase signatures in X-ray diffraction. The transition from the PV to BM phase is accompanied by a metal-to-insulator transition and a ferromagnetic-to-non-ferromagnetic transition. Further investigation revealed two novel intermediate states during continuous high-temperature annealing of the PV sample under vacuum: one corresponding to a pure PV phase with reduced oxygen content and another representing a mixed PV and BM state, each exhibiting continuous changes in oxygen stoichiometry. Through the use of PNR, the oxygen content could be tracked *in-situ*, which is critical for correlating structural evolution with oxygen content. Electronic and magnetic measurements show that the transitions occur while the sample is in the PV structure with a higher concentration of oxygen vacancies, before the BM phase appears. This indicates that the electronic and magnetic transitions take place prior to the structural phase transition, with BM formation observed at an oxygen content of approximately 2.67, while electronic and magnetic transitions occur at higher oxygen levels (2.77 and above) without any BM phase formation. These findings furthermore reveal that the electronic MIT, FM-to-non-FM transition, and structural PV-to-BM phase transition are distinct processes. The observed separation is attributed to the reduction of Co oxidation states during the initial decrease in oxygen content, which causes a dramatic change in the nominal $Co^{4+}$ to $Co^{3+}$ ratio. This, combined with the reduction in oxygen concentration, breaks down the double exchange mechanism of $Co^{3+}$-O-$Co^{4+}$. As a result, the electronic and magnetic transitions occur already before the structural phase transition. This result highlights the significant influence of oxygen defects on complex oxide properties, showing that even small changes in oxygen vacancy concentration can alter magnetic and electronic properties.

Building on these findings, we further investigated the topotactic phase transition by examining the corresponding structural, electronic, magnetic, and chemical reversibility through repeated cycling of the sample between the PV and BM phases. Interestingly, the LSCO thin film can undergo this transition up to 20 times. However, the intensity of both the PV and BM peaks drops to 50% after 20 cycles in XRD, indicating increasing structural incoherence with repeated cycling. This phenomenon can be explained by the chemical changes occurring during reoxidation. XPS analysis reveals that the surface chemistry changes significantly after the first cycle. It is likely that an A-site-rich component forms on the sample surface during the BM to PV reoxidation process, which strongly influences the ratio of the PV/BM phases in the sample and reduces the lattice coherence. As a result, the intensities of the PV/BM-related peaks decrease in the XRD diffractogram. These chemical changes also affect the electronic properties of the LSCO films. With repeated cycling, the resistance values do not overlap in each cycle, although the sample exhibits overall metallic properties. Notably, as the cycles increase to the 15th iteration, the resistance of the sample increases upon cooling (insulating behaviour) rather than decreasing as observed during the first 15 cycles. Unlike the electronic properties, the magnetic properties remain relatively stable throughout the cycles. All the PV phases in different cycles exhibit ferromagnetic behaviour with a saturation magnetization around 0.8 $\mu_B$/Co under a 5 mT magnetic field, while all the BM phases show nearly zero magnetization. This stability is attributed to the reversibility of the Co electronic state, as

evidenced by the X-ray Photoelectron Spectroscopy (XPS) data showing that the Co $2p$ core level spectrum is reversible after reoxidation. The results suggest that LSCO can undergo cycling up to 20 times while maintaining its PV structure. However, the surface chemistry undergoes changes during this process, impacting structural coherence and electronic properties. Interestingly, the magnetic properties are relatively unaffected, as the electronic states of cobalt demonstrate high reversibility during the phase transition.

The reversibility of structural phase transitions in LSCO films enables the same sample to undergo the PV to BM phase transition and return to the PV phase at different temperatures. Building on this, we conducted a comprehensive study of oxygen diffusion and surface exchange processes by annealing the sample under various temperatures and atmospheric conditions. By monitoring changes in intensity and lattice constants during the PV-BM-PV phase transition, the characteristic times of these processes can be determined. Using the Arrhenius equation, the activation energies for the transitions from PV to BM and from BM to PV are calculated to be $0.72 \pm 0.13$ eV and $0.90 \pm 0.1$ eV, respectively. These values align closely with the activation energies for oxygen surface exchange in LSCO (approximately 0.7 to 1 eV) and the nucleation of the new phase (estimated at 0.65 eV for the BM phase and 1.11 eV for the PV phase in similar Co-based perovskite oxides). Accelerating the surface exchange process with Pt can significantly speed up the reduction phase transition without affecting oxygen ion diffusion or the nucleation of the new phase. Therefore, combining these activation energy calculations suggests that the surface exchange is likely the rate-limiting step of the phase transition. However, it is important to note that changes in surface chemistry during the phase transition can modify the surface exchange kinetics. These changes affect the oxygen incorporation and release processes, thereby influencing the overall dynamics of the phase transition.

Finally, in the course of this thesis, the development of delamination techniques within the oxide community has made it possible to study the PV-to-BM phase transition in LSCO in a free-standing form. In such form, the structural flexibility of LSCO during topotactic phase transitions presents significant potential for a variety of applications. To minimize the influence of the substrate (e.g., strain) on the LSCO film in potential applications, this thesis extended the study to free-standing LSCO membranes. These membranes were successfully fabricated using wet-etching methods by Marcus Wohlgemuth and Anton Kaus at PGI-7. The as-grown samples exhibit flat surfaces and a PV structure for both the STO and LSCO free-standing layers, demonstrating a good lattice coherence. After annealing the sample for 2 hours at 450°C in a $10^{-6}$ mbar vacuum environment, the sample completely transitioned to the BM phase, with the typical BM peaks appearing at similar angles to those in LSCO thin films. Furthermore, during the PV to BM structural phase transition, the electronic and magnetic properties of the membrane undergo significant changes, specifically the metal-insulator and the ferromagnetic to non-ferromagnetic transition. These changes are consistent with those observed in the thin films, indicating that the LSCO membrane maintains a similar structural, electronic, and magnetic phase transition behavior as the thin film. This consistency suggests that free-standing LSCO membranes retain the advantageous properties of LSCO thin films,

enabling the study of phase transitions as a function of external strain, and increasing their potential for future applications.

# 6. Outlook

Further investigation is essential to deepen the understanding of the magnetic subsystems observed in LSCO. The origins of these subsystems, particularly in relation to the cracks within the thin film, remain unclear. High-resolution transmission electron microscopy (HR-TEM) could be utilized to analyze the strain fields in the cracked regions of the sample. This would provide insights into how the cracks influence the spin states of cobalt and lead to the formation of magnetic subsystems. Understanding these subsystems is crucial for applications that rely on stable ferromagnetic properties, such as spintronic devices. In this context, a clearer understanding of the role of cracks could allow for better design strategies in thin-film fabrication, helping to minimize redundant magnetic subsystems.

The theoretical exploration of the breakdown of the double-exchange mechanism in LSCO also needs further attention. This process may be closely related to the percolation threshold of the double-exchange mechanism, which is influenced by both oxygen content and the $Co^{3+}/Co^{4+}$ ion ratio. Using percolation theory, one could simulate which of these factors primarily leads to the breakdown of the double exchange and determine the critical oxygen content associated with this phenomenon. A deeper understanding of these factors is crucial for optimizing the electronic and magnetic properties of LSCO thin films, particularly for devices requiring fine-tuned electronic states. The ability to predict and control this breakdown could lead to more efficient oxide-based devices, such as memory and switching devices, where precise control of electronic states is crucial.

The dynamics of the topotactic phase transition in platinum-assisted LSCO samples should also be studied further. The rate of color change near the platinum region could provide valuable information on the speed of oxygen diffusion or the nucleation rate of the BM phase. Accelerating the phase transition process, especially in devices where fast switching between the PV and BM phases is critical, could have significant implications for the development of high-performance oxide-based devices. Platinum catalysis, for example, could be used to enhance the phase transition kinetics, making LSCO more viable for real-world applications where switching speed is essential, such as in-memory devices and catalysis.

Finally, more research is needed on the free-standing LSCO membranes, particularly to investigate the origin of the increased nuclear scattering density in the BM phase. Techniques like HR-TEM or alternative characterization methods could help uncover the underlying causes of these changes. This research is interesting because the free-standing membrane approach could enable the use of LSCO phase transitions on a silicon framework. Such integration would open

up new possibilities for combining the unique properties of LSCO with the widely used silicon substrate, potentially leading to flexible electronics or advanced sensor technologies. This would provide a new path for applying oxide thin films in a broad range of innovative devices.

# 7. Conclusions

This thesis has revealed deep insights into the atomistic and ionic processes involved in the topotactic phase transition of $La_{0.6}Sr_{0.4}CoO_{3-\delta}$ (LSCO) thin films and membranes, revealing their structural, electronic and magnetic properties. In particular, the study emphasizes the critical role of oxygen vacancies in driving the phase transition between the perovskite and brownmillerite structures, as well as their influence on the associated electronic and magnetic transitions. The results show the importance of oxygen defects in driving the phase transitions, with small changes in the oxygen vacancy concentration having a significant effect on the material properties. This study advances the understanding of complex oxides and their behaviour under different conditions in the field of oxide electronics.

The ability to induce reversible phase transitions in LSCO films and membranes presents possibilities for practical applications in electronics. Specifically, the control over metal-insulator transitions and tunable magnetic properties opens ways for the development of advanced electronic devices, such as non-volatile memory cells, sensors, and spintronic devices. Moreover, the successful fabrication of free-standing LSCO membranes, which maintain similar properties to thin films while eliminating substrate effects, could have applications in flexible electronics. Such a study is an important step in reducing the influence of substrates on the material's performance.

Furthermore, this work contributes to the control of ionic and ionotronic phenomena in oxide materials. By exploring the dynamics and reversibility behind the oxygen vacancy-driven phase transitions, this study provides important insights for future research aimed at manipulating ionic transport and charge carrier dynamics in oxide-based systems. The findings could lead to developments in energy storage, catalysis, and environmental sensing technologies, where precise control over ionic movement and electronic states is essential.

While the research focuses on LSCO, the principles discussed could be extended to other complex oxide materials, leading to further advancements in the field of oxide electronics. Building on the insights from this study, future research could investigate how these materials can be used in new devices and technologies that take advantage of their unique ionic and electronic properties.

# A. Error Bar Summary

**Table A.1.:** Summary of experimental parameters and their statistical and systematic errors.

| **Parameter** | **Statistical Error** | **Systematic Error** |
|---|---|---|
| Film thickness (nm) | ±0.3 | ±1.0 |
| Lattice constant (Å) | ±0.002 | ±0.005 |
| Curie temperature (K) | ±2 | ±5 |
| Resistance (Ω) | ±3 | ±5 |
| Magnetization ($\mu_B$/Co) | ±0.02 | ±0.06 |
| Oxygen content | ±0.02 | ±0.03 |
| Nuclear scattering length density ($10^{-6}$ Å$^{-2}$) | ±0.08 | ±0.12 |
| Magnetic scattering length density ($10^{-6}$ Å$^{-2}$) | ±0.02 | ±0.03 |

# B. List of Abbreviations

| Abbreviation | Full term and explanation |
|---|---|
| 2D | Two-Dimensional |
| AFM | Atomic Force Microscopy |
| ALS | Advanced Light Source |
| AP-XPS | Ambient Pressure X-ray Photoelectron Spectroscopy |
| BM | Brownmillerite (crystal structure) |
| DC | Direct Current |
| FC | Field-Cooled |
| HAPEX | Hard X-ray Photoelectron Spectroscopy |
| HAADF-STEM | High-Angle Annular Dark Field Scanning Transmission Electron Microscopy |
| HT-XRD | High-Temperature X-ray Diffraction |
| LSCO | $La_{0.6}Sr_{0.4}CoO_{3-\delta}$ |
| MIT | Metal-Insulator Transition |
| MPMS | Magnetic Property Measurement System |
| MSLD | Magnetic Scattering Length Density |
| NSLD | Nuclear Scattering Length Density |
| PNR | Polarized Neutron Reflectometry |
| PLD | Pulsed Laser Deposition |
| PPMS | Physical Property Measurement System |
| PV | Perovskite (crystal structure) |
| RBS | Rutherford Backscattering Spectrometry |
| RHEED | Reflection High-Energy Electron Diffraction |
| RSO | Reciprocating Sample Option |
| RSM | Reciprocal Space Mapping |
| SQUID | Superconducting Quantum Interference Device |
| rf-SQUID | Radio-Frequency Superconducting Quantum Interference Device |
| STEM | Scanning Transmission Electron Microscopy |
| STO | $SrTiO_3$ (Strontium Titanate) |
| TMOs | Transition Metal Oxides |
| VSM | Vibrating-Sample Magnetometer |
| XPS | X-ray Photoelectron Spectroscopy |
| XRD | X-ray Diffraction |
| SNS | Spallation Neutron Source |

# Bibliography


[1] R. Waser, R. Dittmann, G. Staikov, and K. Szot. "Redox-based resistive switching memories". In: *Adv. Mater.* 21 (2009), p. 2632.

[2] A. Sawa. "Resistive switching in transition metal oxides". In: *Mater. Today* 11 (2008), p. 28.

[3] S. K. Acharya, R. V. Nallagatla, O. Togibasa, B. W. Lee, C. Liu, C. U. Jung, B. H. Park, J.-Y. Park, Y. Cho, D.-W. Kim, J. Jo, D.-H. Kwon, M. Kim, C. S. Hwang, and S. C. Chae. "Oxygen vacancy-induced magnetism in oxide heterostructures". In: *ACS Appl. Mater. Interfaces* 8 (2016), p. 7902.

[4] A. Molinari, H. Hahn, and R. Kruk. "Electrochemical tuning of functional materials". In: *Adv. Mater.* 30 (2018), p. 1703908.

[5] P. Yu, Y.-H. Chu, and R. Ramesh. "Oxide interfaces: pathways to novel phenomena". In: *Materials Today* 15.7-8 (2012), pp. 320–327.

[6] F. Telesio, L. Pellegrino, I. Pallecchi, D. Marré, E. Esposito, E. di Gennaro, A. Khare, and F. M. Granozio. "Interface physics of oxide heterostructures". In: *J. Vac. Sci. Technol. B* 34 (2016).

[7] M. Wilhelm, M. Giesen, T. Duchoň, M. Moors, D. N. Mueller, J. Hackl, C. Baeumer, M. H. Hamed, L. Cao, H. Zhang, O. Petracic, M. Glöß, S. Cramm, S. Nemšák, C. Wiemann, R. Dittmann, C. M. Schneider, and M. Müller. "Electronic structure at complex oxide interfaces". In: *APL Mater.* 8 (2020).

[8] D. Sando et al. "Electrically controllable magnetism at the atomic scale". In: *Nat. Mater.* 12 (2013), p. 641.

[9] F. Trier, P. Noël, J.-V. Kim, J.-P. Attané, L. Vila, and M. Bibes. "Two-dimensional oxide interfaces for quantum technologies". In: *Nat. Rev. Mater.* 7 (2022), p. 258.

[10] D. Stornaiuolo, C. Cantoni, G. D. Luca, R. D. Capua, E. D. Gennaro, G. Ghiringhelli, B. Jouault, D. Marré, D. Massarotti, F. M. Granozio, I. Pallecchi, C. Piamonteze, S. Rusponi, F. Tafuri, and M. Salluzzo. "Tuning spin-orbit coupling in oxide heterostructures". In: *Nat. Mater.* 15 (2016), p. 278.

[11] S. B. Adler. "Factors governing oxygen reduction in solid oxide fuel cell cathodes". In: *Chem. Rev.* 104 (2004), p. 4791.

[12] E. J. Crumlin, E. Mutoro, S.-J. Ahn, G. J. la O', D. N. Leonard, A. Borisevich, M. D. Biegalski, H. M. Christen, and Y. Shao-Horn. "Surface-electronic structure of epitaxial La0.8Sr0.2MnO3 thin films under oxygen". In: *J. Phys. Chem. Lett.* 1 (2010), p. 3149.

[13] Y. A. Mastrikov, M. M. Kuklja, E. A. Kotomin, and J. Maier. "Pulsed laser deposition of La0.8Sr0.2MnO3 thin films on SrTiO3 substrates". In: *Energy Environ. Sci.* 3 (2010), p. 1544.

[14] V. Kharton, E. Naumovich, and A. Nikolaev. "Oxygen permeability of solid electrolytes". In: *J. Membr. Sci.* 111 (1996), p. 149.

[15] J. Biener, A. Wittstock, L. Zepeda-Ruiz, M. Biener, V. Zielasek, D. Kramer, R. Viswanath, J. Weissmüller, M. Bäumer, and A. Hamza. "Nanoporous metals: A new class of materials with tunable properties". In: *Nat. Mater.* 8 (2009), p. 47.

[16] L. Heymann, M. L. Weber, M. Wohlgemuth, M. Risch, R. Dittmann, C. Baeumer, and F. Gunkel. "Interface engineering of SrTiO3/LaAlO3 for improved performance in oxide electronics". In: *ACS Appl. Mater. Interfaces* 14 (2022), p. 14129.

[17] Z. Feng, E. J. Crumlin, W. T. Hong, D. Lee, E. Mutoro, M. D. Biegalski, H. Zhou, H. Bluhm, H. M. Christen, and Y. Shao-Horn. "In situ studies of the temperature-dependent surface structure and chemistry of single-crystalline (001)-oriented La0.8Sr0.2CoO3-$\delta$ perovskite thin films". In: *The Journal of Physical Chemistry Letters* 4.9 (2013), pp. 1512–1518.

[18] B. Tong, Z. Deng, B. Xu, G. Meng, J. Shao, H. Liu, T. Dai, X. Shan, W. Dong, S. Wang, S. Zhou, R. Tao, and X. Fang. "Efficient electron transport in novel oxide interfaces for advanced material applications". In: *ACS Appl. Mater. Interfaces* 10 (2018), p. 34727.

[19] W. Ding, D. Liu, J. Liu, and J. Zhang. "Recent developments in catalytic performance of complex oxide materials". In: *Chin. J. Chem.* 38 (2020), p. 1832.

[20] J. Young and J. M. Rondinelli. "Strain-induced enhancement of the electronic structure of complex oxides". In: *Phys. Rev. B* 92 (2015), p. 174111.

[21] J. H. Jang, Y.-M. Kim, Q. He, R. Mishra, L. Qiao, M. D. Biegalski, A. R. Lupini, S. T. Pantelides, S. J. Pennycook, S. V. Kalinin, and A. Y. Borisevich. "Atomic-scale imaging of domain walls and defects in complex oxide thin films". In: *ACS Nano* 11 (2017), p. 6942.

[22] H. Jeen, W. S. Choi, J. W. Freeland, H. Ohta, C. U. Jung, and H. N. Lee. "Strain-engineering of oxide interfaces for electronic applications". In: *Adv. Mater.* 25 (2013), p. 3651.

[23] Y. M. Kim, J. He, M. D. Biegalski, H. Ambaye, V. Lauter, H. M. Christen, S. T. Pantelides, S. J. Pennycook, S. V. Kalinin, and A. Y. Borisevich. "Atomic-scale observation of metal-insulator transition in LaVO3 thin films". In: *Nat. Mater.* 11 (2012), p. 888.

[24] H. Han, H. Deniz, and S. S. Parkin. "Nanoscale magnetism and its applications". In: *Proc. Natl. Acad. Sci. USA* 120 (2023), e2221651120.

[25] F. Gunkel, L. Jin, D. N. Mueller, C. Hausner, D. S. Bick, C.-L. Jia, T. Schneller, I. Valov, R. Waser, and R. Dittmann. "Surface and Bulk Properties of the La0.5Sr0.5CoO3-Electrodes and Their Influence on the Oxygen Electrochemical Reaction". In: *ACS Catal.* 7 (2017), p. 7029.

[26] Q. Zhang, G. Hu, V. Starchenko, G. Wan, E. M. Dufresne, Y. Dong, H. Liu, H. Zhou, H. Jeen, K. Saritas, J. T. Krogel, F. A. Reboredo, H. N. Lee, A. R. Sandy, I. C. Almazan, P. Ganesh, and D. D. Fong. "Controlling Magnetic and Structural Phase Transitions in Rare-Earth Nickelates". In: *Phys. Rev. Lett.* 129 (2022), p. 235701.

[27] H. Jeen and H. N. Lee. "Tuning the Electronic Structure of Perovskite Oxides via Strain and Electrostatic Modulation". In: *AIP Advances* 5 (2015), p. 127123.

[28] V. Chaturvedi, W. M. Postiglione, R. D. Chakraborty, B. Yu, W. Tabis, S. Hameed, N. Biniskos, A. Jacobson, Z. Zhang, H. Zhou, T. Birol, M. Greven, and C. Leighton. "Perovskite Intercalation and Ion Migration in Oxide Films: Insights from Scanning Probe Microscopy and Transport Studies". In: *ACS Appl. Mater. Interfaces* 13 (2021), p. 51205.

[29] Q. Lu and B. Yildiz. "Anionic Defects and Their Role in Ion Conduction in Oxide Thin Films". In: *Nano Lett.* 16 (2016), p. 1186.

[30] J. Walter, G. Yu, B. Yu, A. Grutter, B. Kirby, J. Borchers, Z. Zhang, H. Zhou, T. Birol, M. Greven, and C. Leighton. "Magnetic Properties of LaCoO3 Thin Films and Their Correlation with Defect Chemistry". In: *Phys. Rev. Mater.* 1 (2017), p. 071403.

[31] J. Gazquez, W. Luo, M. P. Oxley, M. Prange, M. A. Torija, M. Sharma, C. Leighton, S. T. Pantelides, S. J. Pennycook, and M. Varela. "The Role of Oxygen Vacancies and Defects in the Electronic and Magnetic Properties of LaCoO3". In: *Nano Lett.* 11 (2011), p. 973.

[32] L. Cao. "Influence of oxygen content onto magnetic and electrical properties in epitaxial La0.7Sr0.3MnO3-$\delta thinfilms$". PhD thesis. Forschungszentrum Jülich GmbH, 2019.

[33] L. Cao, O. Petracic, X. K. Wei, H. Zhang, T. Duchoň, F. Gunkel, A. Koutsioubas, K. Zhernenkov, K. Z. Rushchanskii, H. Hartmann, M. Wilhelm, Z. Li, Y. Xie, S. He, M. L. Weber, K. Veltruská, A. Stellhorn, J. Mayer, S. Zhou, and T. Brückel. "Magnetic Phase Transitions in Multiferroic La0.7Sr0.3MnO3 Thin Films Probed by Neutron Diffraction and X-ray Scattering". In: *Small* 17 (2021), p. 2104356.

[34] D. Schumacher, A. Steffen, J. Voigt, J. Schubert, T. Brückel, H. Ambaye, and V. Lauter. "Interplay Between Lattice Strain and Magnetism in La0.7Sr0.3MnO3 Thin Films". In: *Phys. Rev. B* 88 (2013), p. 144427.

[35] L. Yao, S. Inkinen, and S. V. Dijken. "Magnetization Dynamics of CoFeB Thin Films: From Growth to Spintronic Applications". In: *Nat. Commun.* 8 (2017), p. 14544.

[36] V. R. Nallagatla, T. Heisig, C. Baeumer, V. Feyer, M. Jugovac, G. Zamborlini, C. M. Schneider, R. Waser, M. Kim, and C. U. Jung. "Oxygen Vacancy Behavior in Oxide Thin Films: Understanding the Mechanisms in Proton Conductors". In: *Adv. Mater.* 31 (2019), p. 1903391.

[37] A. Khare, D. Shin, T. S. Yoo, M. Kim, T. D. Kang, J. Lee, S. Roh, I. H. Jung, J. Hwang, S. W. Kim, T. W. Noh, H. Ohta, and W. S. Choi. "Mechanism of Oxygen Vacancy Ordering in Complex Oxide Thin Films". In: *Adv. Mater.* 29 (2017), p. 1606566.

[38] H. T. D. Nguyen, Y. Wang, P. Schoenherr, P. Sharma, and J. Seidel. "Electric-Field-Controlled Oxygen Vacancies in Oxide Memristors". In: *ACS Appl. Electr. Mater.* 4 (2022), p. 6382.

[39] H. Huang, J. Zhang, H. Zhang, F. Han, X. Chen, J. Song, J. Zhang, S. Qi, Y. Chen, J. Cai, F. Hu, B. Shen, and J. Sun. "Magnetic properties and structural phase transitions in LaCoO3 thin films". In: *J. Phys. D: Appl. Phys.* 53 (2020), p. 155003.

[40] N. Lu et al. "Oxygen vacancy and charge density wave coupling in La1-xSrxCoO3". In: *Nature* 546 (2017), p. 124.

[41] S. R. Spurgeon, P. V. Balachandran, D. M. Kepaptsoglou, A. R. Damodaran, J. Karthik, S. Nejati, L. Jones, H. Ambaye, V. Lauter, and Q. M. Ramasse. "The interplay between structure and electronic properties in complex oxide thin films". In: *Nat. Commun.* 6 (2015), p. 6735.

[42] J. Walter, S. Bose, M. Cabero, G. Yu, M. Greven, M. Varela, and C. Leighton. "Interfacial charge transfer in oxide heterostructures and its impact on device performance". In: *Phys. Rev. Mater.* 2 (2018), p. 111404.

[43] J. Walter, S. Bose, M. Cabero, M. Varela, and C. Leighton. "Tuning magnetism and electronic structure in oxide interfaces". In: *Phys. Rev. Mater.* 4 (2020), p. 091401.

[44] Z. Yin, J. Wang, J. Wang, J. Li, H. Zhou, C. Zhang, H. Zhang, J. Zhang, F. Shen, J. Hao, et al. "Compressive-Strain-Facilitated Fast Oxygen Migration with Reversible Topotactic Transformation in La0.5Sr0.5CoOx via All-Solid-State Electrolyte Gating". In: *ACS nano* 16.9 (2022), pp. 14632–14643.

[45] J. Zhang and R. D. Averitt. "Dynamics and control in complex transition metal oxides". In: *Annual Review of Materials Research* 44.1 (2014), pp. 19–43.

[46] M. Hepting and M. Hepting. "Introduction: Transition metal oxides and their heterostructures". In: *Ordering Phenomena in Rare-Earth Nickelate Heterostructures* (2017), pp. 1–12.

[47] P. Ahuja, S. K. Ujjain, R. Kanojia, and P. Attri. "Transition metal oxides and their composites for photocatalytic dye degradation". In: *Journal of Composites Science* 5.3 (2021), p. 82.

[48] P. A. Cox. *Transition metal oxides: an introduction to their electronic structure and properties*. Oxford university press, 2010.

[49] S. Blundell. *Magnetism in condensed matter*. OUP Oxford, 2001.

[50] W. Research. *Maclaurin Series*. Accessed: 2024-12-01. n.d. URL: https://mathworld.wolfram.com/MaclaurinSeries.html.

[51] D. Jiles. *Introduction to magnetism and magnetic materials*. CRC press, 2015.

[52] T. Miyazaki and H. Jin. *The physics of ferromagnetism*. Vol. 158. Springer Science & Business Media, 2012.

[53] J. B. KH and E. Wohlfarth. *Ferromagnetic materials: A handbook on the properties of magnetically ordered substances*. North Holland, 1980.

[54] S. Chikazumi and C. D. Graham. *Physics of ferromagnetism*. 94. Oxford university press, 1997.

[55] W. Marshall. "Antiferromagnetism". In: *Proceedings of the Royal Society of London. Series A. Mathematical and Physical Sciences* 232.1188 (1955), pp. 48–68.

[56] S. J. Blundell. *Magnetism: a very short introduction*. OUP Oxford, 2012.

[57] C. Zener. "Interaction between the d-shells in the transition metals. II. Ferromagnetic compounds of manganese with perovskite structure". In: *Physical Review* 82.3 (1951), p. 403.

[58] P. W. Anderson. "Antiferromagnetism. Theory of superexchange interaction". In: *Physical Review* 79.2 (1950), p. 350.

[59] J. B. Goodenough. "An interpretation of the magnetic properties of the perovskite-type mixed crystals La1-xSrxCoO3-$\lambda$". In: *Journal of Physics and chemistry of Solids* 6.2-3 (1958), pp. 287–297.

[60] J. Kanamori. "Superexchange interaction and symmetry properties of electron orbitals". In: *Journal of Physics and Chemistry of Solids* 10.2-3 (1959), pp. 87–98.

[61] J. B. Goodenough. "Theory of the role of covalence in the perovskite-type manganites [La, M (II)]MnO3". In: *Physical Review* 100.2 (1955), p. 564.

[62] J. Zhang, D. Meng, H. Huang, H. Cai, Q. Huang, J. Wang, Y. Yang, X. Zhai, Z. Fu, and Y. Lu. "Phase competition in the growth of SrCoOx/LaAlO3 thin films". In: *AIP Advances* 8.2 (2018).

[63] J. Zhao, K. Chen, S.-E. Li, Q. Zhang, J.-O. Wang, E.-J. Guo, H. Qian, L. Gu, T. Qian, K. Ibrahim, et al. "Electronic-structure evolution of SrFeO3-x during topotactic phase transformation". In: *Journal of Physics: Condensed Matter* 34.6 (2021), p. 064001.

[64] R. A. Fillhouer. "Topotactic Phase Transformations in Manganite Thin Films and Cobaltite Bilayers". PhD thesis. UC Davis, 2023.

[65] L. Yao, S. Majumdar, L. Äkäslompolo, S. Inkinen, Q. H. Qin, and S. van Dijken. "Electron-Beam-Induced Perovskite–Brownmillerite–Perovskite Structural Phase Transitions in Epitaxial La2/3Sr1/3MnO3 Films". In: *Advanced Materials* 26.18 (2014), pp. 2789–2793.

[66] Y. Wu, V. Rosendal, M. Vasiljevic, I. Asghar, and V. Esposito. “Strain-oxygen vacancies coupling in topotactic (La,Sr)Co3-$\delta$ thin films”. In: *Applied Surface Science Advances* 24 (2024), p. 100644.

[67] J. Mastin, M.-A. Einarsrud, and T. Grande. “Structural and Thermal Properties of La1-xSrxCoO3-$\delta$”. In: *Chemistry of materials* 18.25 (2006), pp. 6047–6053.

[68] J. Wu and C. Leighton. “Glassy ferromagnetism and magnetic phase separation in La 1-xSrxCoO3”. In: *Physical Review B* 67.17 (2003), p. 174408.

[69] R. Smith, M. Hoch, W. Moulton, P. Kuhns, A. Reyes, G. Boebinger, H Zheng, and J. Mitchell. “Evolution of the spin-state transition with doping in La1-xSrxCoO3”. In: *Physical Review B—Condensed Matter and Materials Physics* 86.5 (2012), p. 054428.

[70] K. Momma and F. Izumi. “VESTA 3 for three-dimensional visualization of crystal, volumetric and morphology data”. In: *Journal of applied crystallography* 44.6 (2011), pp. 1272–1276.

[71] K. Momma and F. Izumi. “VESTA: a three-dimensional visualization system for electronic and structural analysis”. In: *Journal of Applied crystallography* 41.3 (2008), pp. 653–658.

[72] M. A. Peña and J. L. Fierro. “Chemical structures and performance of perovskite oxides”. In: *Chemical reviews* 101.7 (2001), pp. 1981–2018.

[73] M. T. Anderson, J. T. Vaughey, and K. R. Poeppelmeier. “Structural similarities among oxygen-deficient perovskites”. In: *Chemistry of materials* 5.2 (1993), pp. 151–165.

[74] S. Bose. “Complexity at Cobaltite Interfaces: The Interplay between Strain, Stoichiometry, Magnetism and Transport”. PhD thesis. University of Minnesota, 2014.

[75] O. H. Hansteen, H. Fjellvåg, and B. C. Hauback. “Crystal structure and magnetic properties of La2Co2O5”. In: *Journal of Solid State Chemistry* 141.2 (1998), pp. 411–417.

[76] L. Cao, O. Petracic, P. Zakalek, A. Weber, U. Rücker, J. Schubert, A. Koutsioubas, S. Mattauch, and T. Brückel. “Reversible Control of Physical Properties via an Oxygen-Vacancy-Driven Topotactic Transition in Epitaxial La0.7Sr0.3MnO3-$\delta$ Thin Films”. In: *Advanced materials* 31.7 (2019), p. 1806183.

[77] H. Wang, J. Song, W. Wang, Y. Chen, X. Shen, Y. Yao, J. Li, J. Sun, and R. Yu. “SrCoO3-$\delta$ microstructures in Perovskite-Brownmillerite heterostructure”. In: *Journal of Crystal Growth* 572 (2021), p. 126278.

[78] K. Li, Y. Wang, J. Lin, and Z. Li. “Phase relations of BaCoO3-$\delta$–BaInO2.5 and size variation effect of B-site cations on the phase transitions”. In: *Solid State Ionics* 183.1 (2011), pp. 7–15.

[79] S. Roh, S. Lee, M. Lee, Y.-S. Seo, A. Khare, T. Yoo, S. Woo, W. S. Choi, J. Hwang, A Glamazda, et al. “Oxygen vacancy induced structural evolution of SrFeO 3- x epitaxial thin film from brownmillerite to perovskite”. In: *Physical Review B* 97.7 (2018), p. 075104.

[80] J. E. Sunstrom IV, K. Ramanujachary, M. Greenblatt, and M. Croft. "The synthesis and properties of the chemically oxidized perovskite, La1-xSrxCoO3-$\delta$ (0.5<x<0.9)". In: *Journal of Solid State Chemistry* 139.2 (1998), pp. 388–397.

[81] J. Walter, S. Bose, M. Cabero, G. Yu, M. Greven, M. Varela, and C. Leighton. "Perpendicular magnetic anisotropy via strain-engineered oxygen vacancy ordering in epitaxial La1-xSrxCoO3-$\delta$". In: *Physical Review Materials* 2.11 (2018), p. 111404.

[82] V. Chaturvedi, W. M. Postiglione, R. D. Chakraborty, B. Yu, W. Tabis, S. Hameed, N. Biniskos, A. Jacobson, Z. Zhang, H. Zhou, et al. "Doping-and Strain-Dependent Electrolyte-Gate-Induced Perovskite to Brownmillerite Transformation in Epitaxial La1-xSrxCoO3-$\delta$ Films". In: *ACS applied materials & interfaces* 13.43 (2021), pp. 51205–51217.

[83] S. Inkinen, L. Yao, and S. van Dijken. "Reversible thermal strain control of oxygen vacancy ordering in an epitaxial La0.5Sr0.5CoO3-$\delta$ film". In: *Physical Review Materials* 4.4 (2020), p. 046002.

[84] W. M. Postiglione, J. Liang, N. Nandakumaran, L. Figari, A. A. Aczel, and C. Leighton. "Direct neutron-diffraction-based measurement of magnetic order in brownmillerite SrCoO2.5 and La0.5Sr0.5CoO2.5 thin films". In: *APL Materials* 12.4 (2024).

[85] C. Monty. "Diffusion in oxides". In: *Defects in Solids: Modern Techniques*. Springer, 1986, pp. 377–394.

[86] M. Martin. "Diffusion in oxides". In: *Diffusion in Condensed Matter: Methods, Materials, Models*. Springer, 2005, pp. 209–247.

[87] J. Song, Y. Chen, H. Zhang, F. Han, J. Zhang, X. Chen, H. Huang, J. Zhang, H. Zhang, X. Yan, et al. "Strong anisotropy and its electric tuning for brownmillerite SrCoO2.5 films with different crystal orientations". In: *Physical Review Materials* 3.4 (2019), p. 045801.

[88] S. B. Adler, X. Y. Chen, and J. R. Wilson. "Mechanisms and rate laws for oxygen exchange on mixed-conducting oxide surfaces". In: *Journal of Catalysis* 245.1 (2007), pp. 91–109.

[89] R. Merkle and J. Maier. "Oxygen incorporation into Fe-doped SrTiO3: Mechanistic interpretation of the surface reaction". In: *Physical Chemistry Chemical Physics* 4.17 (2002), pp. 4140–4148.

[90] Q. Zhang, G. Hu, V. Starchenko, G. Wan, E. M. Dufresne, Y. Dong, H. Liu, H. Zhou, H. Jeen, K. Saritas, et al. "Phase transition dynamics in a complex oxide heterostructure". In: *Physical Review Letters* 129.23 (2022), p. 235701.

[91] K. J. Skaja. "Redox processes and ionic transport in resistive switching binary metal oxides". PhD thesis. Dissertation, RWTH Aachen University, 2016.

[92] M. T. Andrä. "Chemical Control of the Electrical Surface Properties of n-Doped Transition Metal Oxides". PhD thesis. RWTH Aachen University, 2019.

[93] G. F. Harrington and J. Santiso. “Back-to-Basics tutorial: X-ray diffraction of thin films”. In: *Journal of Electroceramics* 47.4 (2021), pp. 141–163.

[94] H. G. J. Moseley. “XCIII. The high-frequency spectra of the elements”. In: *The London, Edinburgh, and Dublin Philosophical Magazine and Journal of Science* 26.156 (1913), pp. 1024–1034.

[95] T. Brückel, G. Heger, D. Richter, R. Zorn, and G. Roth. *Laboratory Course Neutron Scattering: Lectures*. PreJuSER-16299. Streumethoden, 2011.

[96] T. B.V. *Pulsed Laser Deposition (PLD) Systems*. Accessed: 2024-10-08. 2024. URL: `https://tsst.demcon.com/product/pld/`.

[97] R. Dittmann. *"Stoichiometry in epitaxial oxide thin films," in Epitaxial growth of complex metal oxides, ,Koster, Gertjan and Huijben, Mark and Rijnders, Guus*. Elsevier, 2015.

[98] P. Willmott. “Deposition of complex multielemental thin films”. In: *Progress in Surface Science* 76.6-8 (2004), pp. 163–217.

[99] G. Koster, G. J. Rijnders, D. H. Blank, and H. Rogalla. “Imposed layer-by-layer growth by pulsed laser interval deposition”. In: *Applied physics letters* 74.24 (1999), pp. 3729–3731.

[100] A. J. Rijnders. “The initial growth of complex oxides: study and manipulation”. In: *research.utwente.nl* (2001).

[101] M. Naito, H. Yamamoto, and H. Sato. “Reflection high-energy electron diffraction and atomic force microscopy studies on homoepitaxial growth of SrTiO3 (001)”. In: *Physica C: Superconductivity* 305.3-4 (1998), pp. 233–250.

[102] G. Rijnders and D. H. Blank. “Real-time Growth monitoring by High-pressure RHEED during pulsed laser deposition”. In: *Thin Films and Heterostructures for Oxide Electronics* (2005), pp. 355–384.

[103] D. H. Blank, G. J. Rijnders, G. Koster, and H. Rogalla. “A new approach in layer-by-layer growth of oxide materials by pulsed laser deposition”. In: *Journal of electroceramics* 4 (2000), pp. 311–318.

[104] P. Eaton and P. West. *Atomic force microscopy*. Oxford university press, 2010.

[105] B. Voigtländer. *Atomic force microscopy*. Springer, 2019.

[106] National Institute of Standards and Technology (NIST). *Scanning Probe Microscopy for Advanced Materials and Processes*. Accessed: September 6, 2024. 2020.

[107] V. Lauter, H. Ambaye, R. Goyette, W.-T. H. Lee, and A. Parizzi. “Highlights from the magnetism reflectometer at the SNS”. In: *Physica B: Condensed Matter* 404.17 (2009), pp. 2543–2546.

[108] T Brückel, J Voigt, G Heger, G Roth, H Frielinghaus, J Stellbrink, R. Hermann, E Kentzinger, U Rücker, R Zorn, et al. “Laboratory Course Neutron Scattering”. In: *Forschungszentrum Jülich GmbH* (2007).

[109] O. R. N. Laboratory. *Magnetism Reflectometer (MAGREF)*. Accessed: 2024-09-18. 2024. URL: https://neutrons.ornl.gov/mr.

[110] M. Björck and G. Andersson. "GenX: an extensible X-ray reflectivity refinement program utilizing differential evolution". In: *Journal of Applied Crystallography* 40.6 (2007), pp. 1174–1178.

[111] L. Lewis and K. M. Bussmann. "A sample holder design and calibration technique for the quantum design magnetic properties measurement system superconducting quantum interference device magnetometer". In: *Review of scientific instruments* 67.10 (1996), pp. 3537–3542.

[112] Quantum Design. *SQUID MPMS XL-5*. URL: \url{https://www.ism.cnr.it/en/tempism/analysis/magnetism-and-transport/squid-magnetometry/squid-mpms-xl-5.html}.

[113] I. Quantum Design. *Physical Property Measurement System: User's Manual*. Quantum Design, Inc. San Diego, CA, 2002.

[114] EAG Laboratories. *Rutherford Backscattering Spectrometry (RBS) Tutorial*. Accessed: 2024-09-19. n.d. URL: https://www.eag.com/app-note/rutherford-backscattering-spectrometry-rbs-tutorial/.

[115] L. R. Doolittle. "Algorithms for the rapid simulation of Rutherford backscattering spectra". In: *Nuclear Instruments and Methods in Physics Research Section B: Beam Interactions with Materials and Atoms* 9.3 (1985), pp. 344–351.

[116] L. R. Doolittle. "A semiautomatic algorithm for Rutherford backscattering analysis". In: *Nuclear Instruments and Methods in Physics Research Section B: Beam Interactions with Materials and Atoms* 15.1-6 (1986), pp. 227–231.

[117] J. Deng, K. Dong, P. Yang, Y. Peng, G. Ju, J. Hu, G. M. Chow, and J. Chen. "Large lattice mismatch effects on the epitaxial growth and magnetic properties of FePt films". In: *Journal of Magnetism and Magnetic Materials* 446 (2018), pp. 125–134.

[118] C. Adamo, L. Méchin, T Heeg, M Katz, S. Mercone, B. Guillet, S. Wu, J.-M. Routoure, J Schubert, W Zander, et al. "Enhanced electrical and magnetic properties in La0.7Sr0.3MnO3 thin films deposited on CaTiO3-buffered silicon substrates". In: *APL materials* 3.6 (2015).

[119] MSE Supplies. *SrTiO3 - Strontium Titanate Crystal*. https://www.msesupplies.com/en-de/products/srtio3-strontium-titanate-crystal. Accessed: 14-Oct-2024.

[120] G. Koster, B. L. Kropman, G. J. Rijnders, D. H. Blank, and H. Rogalla. "Quasi-ideal strontium titanate crystal surfaces through formation of strontium hydroxide". In: *Applied Physics Letters* 73.20 (1998), pp. 2920–2922.

[121] G. Koster, G. Rijnders, D. H. Blank, and H. Rogalla. "Surface morphology determined by (0 0 1) single-crystal SrTiO3 termination". In: *Physica C: Superconductivity* 339.4 (2000), pp. 215–230.

[122] M. L. Weber, G. Lole, A. Kormanyos, A. Schwiers, L. Heymann, F. D. Speck, T. Meyer, R. Dittmann, S. Cherevko, C. Jooss, et al. "Atomistic insights into activation and degradation of La0.6Sr0.4CoO3-$\delta$ electrocatalysts under oxygen evolution conditions". In: *Journal of the American Chemical Society* 144.39 (2022), pp. 17966–17979.

[123] M. L. Weber, C. Baeumer, D. N. Mueller, L. Jin, C.-L. Jia, D. S. Bick, R. Waser, R. Dittmann, I. Valov, and F. Gunkel. "Electrolysis of water at atomically tailored epitaxial cobaltite surfaces". In: *Chemistry of materials* 31.7 (2019), pp. 2337–2346.

[124] J. M. Börgers. "Combining Experimental and Computational Approaches to Characterise and Understand Oxygen Diffusion in (La, Sr) MnO_3". PhD thesis. Dissertation, RWTH Aachen University, 2022, 2022.

[125] A. Sambri, M. Scuderi, A. Guarino, E. D. Gennaro, R. Erlandsen, R. T. Dahm, A. V. Bjørlig, D. V. Christensen, R. D. Capua, B. D. Ventura, et al. "Self-Formed, Conducting LaAlO3/SrTiO3 Micro-Membranes". In: *Advanced Functional Materials* 30.45 (2020), p. 1909964.

[126] S Lee, S. Choi, and Y.-Y. Earmme. "Analysis of vertical cracking phenomena in tensile-strained epitaxial film on a substrate: Part I. Mathematical formulation". In: *International journal of solids and structures* 43.11-12 (2006), pp. 3401–3413.

[127] M. Torija, M Sharma, M. Fitzsimmons, M Varela, and C. Leighton. "Epitaxial La0.5Sr0.5CoO3 thin films: Structure, magnetism, and transport". In: *Journal of Applied Physics* 104.2 (2008).

[128] W. S. Choi, J.-H. Kwon, H. Jeen, J. E. Hamann-Borrero, A. Radi, S. Macke, R. Sutarto, F. He, G. A. Sawatzky, V. Hinkov, et al. "Strain-induced spin states in atomically ordered cobaltites". In: *Nano letters* 12.9 (2012), pp. 4966–4970.

[129] O. Lis, S. Kichanov, D. Kozlenko, Z Jirak, A. Belushkin, and B. Savenko. "Pressure-induced spin state crossover in layered cobaltite LaSrCoO4". In: *Journal of Magnetism and Magnetic Materials* 487 (2019), p. 165360.

[130] R. J. Tilley. *Perovskites: structure-property relationships*. John Wiley & Sons, 2016.

[131] M. Senarıs-Rodrıguez and J. Goodenough. "Magnetic and Transport Properties of the System La1-xSrxCoO3-$\delta$ (0< x 0.50)". In: *Journal of Solid State Chemistry* 118.2 (1995), pp. 323–336.

[132] M Merz, P Nagel, C Pinta, A. v. Samartsev, H. v. Löhneysen, M Wissinger, S Uebe, A Assmann, D Fuchs, and S Schuppler. "X-ray absorption and magnetic circular dichroism of LaCoO3, La0.7Ce0.3CoO3, and La0.7Sr0.3CoO 3 films: Evidence for cobalt-valence-dependent magnetism". In: *Physical Review B* 82.17 (2010), p. 174416.

[133] Z. Yin, J. Wang, J. Wang, J. Li, H. Zhou, C. Zhang, H. Zhang, J. Zhang, F. Shen, J. Hao, et al. "Compressive-Strain-Facilitated Fast Oxygen Migration with Reversible Topotactic Transformation in La0.5Sr0.5CoOx via All-Solid-State Electrolyte Gating". In: *ACS nano* 16.9 (2022), pp. 14632–14643.

[134] B. Liu, G. Liu, H. Feng, C. Wang, H. Yang, and Y. Wang. "Effect of oxygen vacancies on structural, electrical and magnetic properties of La0.67Sr0.33CoO3 thin films". In: *Materials & Design* 89 (2016), pp. 715–720.

[135] V. Sathe, A. Pimpale, V Siruguri, and S. Paranjpe. "Neutron diffraction studies of perovskite-type compounds La {sub 1-x} Sr {sub x} CoO {sub 3}(x= 0.1, 0.2, 0.3, 0.4, 0.5)". In: *Journal of Physics. Condensed Matter* 8 (1996).

[136] Q. Lu and B. Yildiz. "Voltage-controlled topotactic phase transition in thin-film SrCoO x monitored by in situ x-ray diffraction". In: *Nano letters* 16.2 (2016), pp. 1186–1193.

[137] S. He, O. Petracic, V. Lauter, L. Cao, Y. Zhou, M. L. Weber, J. Schubert, O. Concepción, R. Dittmann, R. Waser, et al. "La0. 6Sr0.4CoO3-$\delta$ films under deoxygenation: Magnetic and electronic transitions are apart from the structural phase transition". In: *Advanced Functional Materials* 34.24 (2024), p. 2313208.

[138] J Gazquez, S. Bose, M Sharma, M. Torija, S. J. Pennycook, C Leighton, and M Varela. "Lattice mismatch accommodation via oxygen vacancy ordering in epitaxial La0. 5Sr0. 5CoO3-$\delta$ thin films". In: *APL Materials* 1.1 (2013).

[139] X. Cheng, E. Fabbri, M. Nachtegaal, I. E. Castelli, M. El Kazzi, R. Haumont, N. Marzari, and T. J. Schmidt. "Oxygen evolution reaction on La1-xSrxCoO3 perovskites: a combined experimental and theoretical study of their structural, electronic, and electrochemical properties". In: *Chemistry of Materials* 27.22 (2015), pp. 7662–7672.

[140] I.-T. Chiu, M.-H. Lee, S. Cheng, S. Zhang, L. Heki, Z. Zhang, Y. Mohtashami, P. N. Lapa, M. Feng, P. Shafer, et al. "Cation and anion topotactic transformations in cobaltite thin films leading to Ruddlesden-Popper phases". In: *Physical Review Materials* 5.6 (2021), p. 064416.

[141] V Lauter-Pasyuk. "Neutron grazing incidence techniques for nano-science". In: *Collect. SFN* 7 (2007), s221–s240.

[142] S. Tanuma, C. J. Powell, and D. R. Penn. "Calculations of electron inelastic mean free paths. V. Data for 14 organic compounds over the 50-2000 eV range". In: *Surface and interface analysis* 21.3 (1994), pp. 165–176.

[143] C. J. Powell. "Practical guide for inelastic mean free paths, effective attenuation lengths, mean escape depths, and information depths in x-ray photoelectron spectroscopy". In: *Journal of Vacuum Science & Technology A* 38.2 (2020).

[144] Q. Lu, Y. Chen, H. Bluhm, and B. Yildiz. "Electronic structure evolution of SrCoO x during electrochemically driven phase transition probed by in situ X-ray spectroscopy". In: *The Journal of Physical Chemistry C* 120.42 (2016), pp. 24148–24157.

[145] N. McIntyre and M. Cook. "X-ray photoelectron studies on some oxides and hydroxides of cobalt, nickel, and copper". In: *Analytical chemistry* 47.13 (1975), pp. 2208–2213.

[146] M. C. Biesinger, B. P. Payne, A. P. Grosvenor, L. W. Lau, A. R. Gerson, and R. S. C. Smart. "Resolving surface chemical states in XPS analysis of first row transition metals, oxides and hydroxides: Cr, Mn, Fe, Co and Ni". In: *Applied Surface Science* 257.7 (2011), pp. 2717–2730.

[147] W. T. Hong, K. A. Stoerzinger, E. J. Crumlin, E. Mutoro, H. Jeen, H. N. Lee, and Y. Shao-Horn. "Near-ambient pressure XPS of high-temperature surface chemistry in Sr2Co2O5 thin films". In: *Topics in Catalysis* 59 (2016), pp. 574–582.

[148] A. Nenning, A. K. Opitz, C. Rameshan, R. Rameshan, R. Blume, M. Havecker, A. Knop-Gericke, G. Rupprechter, B. Klotzer, and J. Fleig. "Ambient pressure XPS study of mixed conducting perovskite-type SOFC cathode and anode materials under well-defined electrochemical polarization". In: *The Journal of Physical Chemistry C* 120.3 (2016), pp. 1461–1471.

[149] P. Van Der Heide. "Systematic x-ray photoelectron spectroscopic study of La1-xSrx-based perovskite-type oxides". In: *Surface and Interface Analysis: An International Journal devoted to the development and application of techniques for the analysis of surfaces, interfaces and thin films* 33.5 (2002), pp. 414–425.

[150] H. Shin, J. Seo, S. Jeon, S. J. Jeong, J. Kim, S. Lee, J. J. Lee, and W. Jung. "Enhanced catalytic activity and stability of SOFC electrodes through plasma-driven surface modification". In: *Journal of Materials Chemistry A* 12.18 (2024), pp. 10695–10703.

[151] A. K. Opitz, C. Rameshan, M. Kubicek, G. M. Rupp, A. Nenning, T. Götsch, R. Blume, M. Hävecker, A. Knop-Gericke, G. Rupprechter, et al. "The Chemical Evolution of the La0.6Sr0.4CoO3-$\delta$ Surface Under SOFC Operating Conditions and Its Implications for Electrochemical Oxygen Exchange Activity". In: (2018).

[152] M. Siebenhofer, C. Riedl, A. Nenning, W. Artner, C. Rameshan, A. K. Opitz, J. Fleig, and M. Kubicek. "Improving and degrading the oxygen exchange kinetics of La0.6Sr0.4CoO 3-$\delta$ by Sr decoration". In: *Journal of Materials Chemistry A* 11.24 (2023), pp. 12827–12836.

[153] M. Siebenhofer, T. M. Huber, G. Friedbacher, W. Artner, J. Fleig, and M. Kubicek. "Oxygen exchange kinetics and nonstoichiometry of pristine La0.6Sr0.4CoO3-$\delta$ thin films unaltered by degradation". In: *Journal of Materials Chemistry A* 8.16 (2020), pp. 7968–7979.

[154] A. Berenov, A Atkinson, J. Kilner, E. Bucher, and W. Sitte. "Oxygen tracer diffusion and surface exchange kinetics in La0.6Sr0.4CoO3-$\delta$". In: *Solid State Ionics* 181.17-18 (2010), pp. 819–826.

[155] M. Kubicek, Z. Cai, W. Ma, B. Yildiz, H. Hutter, and J. Fleig. "Tensile Lattice Strain Accelerates Oxygen Surface Exchange and Diffusion in La1-xSrxCoO3-$\delta$ Thin Films". In: *ACS nano* 7.4 (2013), pp. 3276–3286.

[156] J. Lee, Y. Ha, and S. Lee. “Hydrogen Control of Double Exchange Interaction in La0.67Sr0.33MnO3 for Ionic–Electric–Magnetic Coupled Applications”. In: *Advanced Materials* 33.11 (2021), p. 2007606.

[157] Q. Wang, Y. Gu, W. Zhu, L. Han, F. Pan, and C. Song. “Noble-Metal-Assisted Fast Interfacial Oxygen Migration with Topotactic Phase Transition in Perovskite Oxides”. In: *Advanced Functional Materials* 31.50 (2021), p. 2106765.

[158] M. Huff. “Residual stresses in deposited thin-film material layers for micro-and nano-systems manufacturing”. In: *Micromachines* 13.12 (2022), p. 2084.

[159] PCBMake. *Thin Film Ceramic Substrates*. 2023. URL: `https://pcbmake.com/thin-film-ceramic-substrates/` (visited on 03/26/2024).

[160] M. Park, B. Bae, T. Kim, H. S. Kum, and K. Lee. “2D materials-assisted heterogeneous integration of semiconductor membranes toward functional devices”. In: *Journal of Applied Physics* 132.19 (2022).

# List of Figures

**Eidesstattliche Erklärung**

**Declaration of Authorship**

I, *Suqin He*

declare that this thesis and the work presented in it are my own and has been generated by me as the result of my own original research.

Hiermit erkläre ich an Eides statt / I do solemnely swear that:

1. This work was done wholly or mainly while in candidature for the doctoral degree at this faculty and university.

2. Where any part of this thesis has previously been submitted for a degree or any other qualification at this university or any other institution, this has been clearly stated.

3. Where I have consulted the published work of others or myself, this is always clearly attributed.

4. Where I have quoted from the work of others or myself, the source is always given. This thesis is entirely my own work, with the exception of such quotations.

5. I have acknowledged all major sources of assistance.

6. Where the thesis is based on work done by myself jointly with others, I have made clear exactly what was done by others and what I have contributed myself.

7. Parts of this work have been published before as: He, Suqin, et al. "$La_{0.6}Sr_{0.4}CoO_{3-\delta}$ films under deoxygenation: Magnetic and electronic transitions are apart from the structural phase transition." *Advanced Functional Materials* 34.24 (2024): 2313208.
https://doi.org/10.1002/adfm.202313208

*Date: 01.12.2024*

*Signature:* Suqin He